Modeling the Rheology of Ordinary and Associating Unentangled Polymer Melts

Hongwei Liu
Department of Chemical, Materials, and Production Engineering
University of Naples Federico II

A thesis submitted for the degree of
PhilosophiæDoctor (PhD)

December 2021

Supervisor: Giovanni Ianniruberto

Signature from head of PhD committee:

Abstract

We are aiming at studying the rheological behavior of ordinary and associating polymers. Ordinary polymers refer to polymers without stickers but under fast flows. Associating polymers are a group of polymers which are held together through reversible non covalent bonds, such as ionic interactions, metal-ligand, π-π stacking, and hydrogen bonds. Both topics have attracted enormous attention either due to the non-universal features in fast flows of polymer melts or because of their unique abilities for working as self-healing, stimuli-sensitive, and shape-memory materials.

Fast flows and large deformation rates typically are involved in polymer processing operations and no general constitutive equation can be written that describes these nonlinear rheological behavior exhibited by polymer flows. Therefore, molecular modeling of the rheology of polymers in fast flow was developed many years ago. The friction reduction due to coalignment of polymer chains has been confirmed both through molecular dynamics simulations and extensional flow experiments. In spite of the results achieved by the friction reduction model, the flow-induced reduction of the friction coefficient is still highly controversial. For instance, the Einstein relationship between ζ and the diffusion coefficient probably does not hold true away from equilibrium.

This thesis partly focuses on enhancing our understanding of the mechanisms behind the nonlinear responses of the unentangled polymer melts under fast shear flow through a coarse-grained modeling approach. We take advantage of the rich set of data of Kremer-Grest melts in fast steady shear flows. First, we apply the data to the latest Watanabe's model. Then we reproduce them by suitable Brownian dynamics simulations, where the beads are endowed with isotropic and anisotropic friction separately.

Likewise, molecular modeling is typically used to study the viscoelastic response of associating polymers as well. The most famous one is the sticky Rouse model. This model is capable of accounting for the slowing down of the relaxation caused by reversible bonds. However, the effects of the lifetime, density, and distribution of stickers on the dynamics of associating polymers is still a matter of some debate. For instance, a mismatch between data and predictions of this model at the intermediate frequencies always appears.

The rest of this thesis concentrates on studying the dynamics of associating polymers. A multi-chain model and a single-chain model are proposed. The predictions of the multi-chain model are able to describe the topological structure of polymer networks. Meanwhile, those effects on rheological behavior are studied. The results are compared with the predictions of the sticky Rouse model. The single-chain model, which was designed to save running time, allows stickers to be distributed randomly. The predictions are compared with data.

Acknowledgements

I would like to acknowledge my supervisor, Professor Giovanni Ianniruberto, first. Prof. Ianniruberto not only assists me with the Ph.D. project, but also takes care of my life. Prof. even asked other student for a textbook for me during a coffee break. I did not realized that how lucky am I until I heard that other foreign students encountered bureaucratic problems now and then. Prof. does everything he can to support my study. I remembered that Prof. came to my office immediately with a mouse just after I told him that the mouse did not work. Thanks to Prof.'s assistance, I can get used to the local life easily. I would thank Professor Giuseppe Marrucci as well since he provided a large number of insightful suggestions to my Ph.D. project. His insistence in small but crucial details impress me profoundly. Thanks should also be given to Professor Qian Huang and Professor Ole Hassager for their host of my academic secondment. Their sharing knowledge as well as their passion on research touched me. Professor Daniel Read, Professor Yuichi Masubuchi, and Professor Zuowei Wang gave me many useful suggestions to the project. I appreciate their kindness. I would also like to give my thank to our coordinator, Professor Evelyne van Ruymbeke, not only for her intuitive suggestions to the project but also for her Rheology lecture at UCL.

At Department of Chemical, Materials, and Production Engineering, I met many amiable Professors and students, they are Professor Nino Grizzuti, thanks for his lecture ”Advanced Transport Phenomena”, I am impressed by his explanation of the Gaussian theorem in such a clear way; Professor Francesco Greco, thanks for his lecture ”Applied Physical Chemistry”; Professor Stefano Guido, thanks for his lecture ”Advanced Thermodynamics”; Professor Pasquino Rossana, for her lecture ”Rheology”; and Technician

Veronica Vanzanella. I would like to thank Ph.D. students Pietro Avallone, Vincenzo Ianniello and Marica Muscetta. Due to the problems of language, they helped me with many detailed things.

Special thanks go to my DoDyNet colleagues and other Professors, we had a wonderful time together.

Finally, I would like to thank my family. Thanks for their tolerance, love and incessant support.

Contents

List of Figures

List of Tables

1

Introduction

1.1 Linear Response of Materials: Elastic, Viscous, Viscoelastic

1.1.1 Linear Elastic Properties

Elasticity is a property of matter typical of the solid state. An elastic solid can be deformed by applying suitable forces, and recovers the original shape when those forces are removed. Locally, i.e. in a small neighborhood of a material point, elasticity is described by a relationship (a constitutive equation) that links stresses and strains at that point. Such a relationship is generally nonlinear. However, if only small strains (or small stresses) are considered, the relationship becomes linear. Alternatively, when one starts deforming (or forcing) an elastic material, the initial response is always linear, to become nonlinear only eventually, when strains (or stresses) are large. We will only consider amorphous solids, like glass or rubber. Crystals are more complicated, because they are anisotropic, i.e., their response to deformation depends on how the crystal is oriented.

Figure 1.1 shows the configurations of an amorphous solid before and after an uniaxial extension. We introduce the stretch ratio $\lambda = L/L_0$ as a scalar measure of the extension. When the deformation is small, i.e., λ is close to unity, it becomes convenient to introduce the strain ε:

$$\varepsilon = \lambda - 1 = \frac{L - L_0}{L_0} \ll 1 \tag{1.1}$$

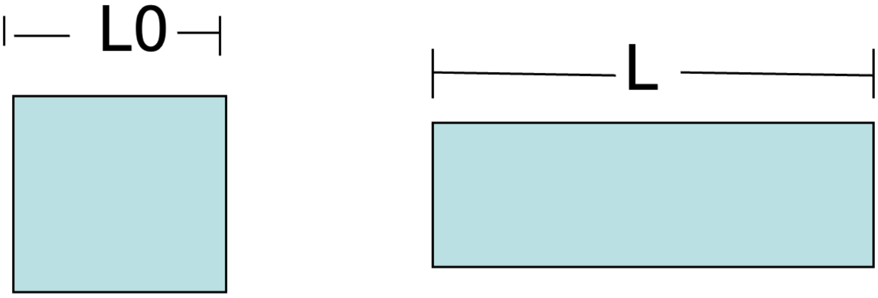

Figure 1.1: Small deformations in uniaxial extension. - L_0 and L are the undeformed and deformed lengths, respectively

To achieve a (small) strain, a force per unit area is required, given by:

$$F/A = E\varepsilon, \tag{1.2}$$

where the coefficient of this linear law is the Young's modulus. Assuming that the uniaxial extension occurs along x, the material element contracts along y and z in most cases. The corresponding strains are therefore negative, given by:

$$\varepsilon_y = \varepsilon_z = \mu\varepsilon, \tag{1.3}$$

where μ is Poisson's ratio ($\mu \leq 1/2$). $\mu = 1/2$ on condition that the material is incompressible.

Figure 1.2 displays the configurations of an amorphous solid before and after a simple shear deformation.

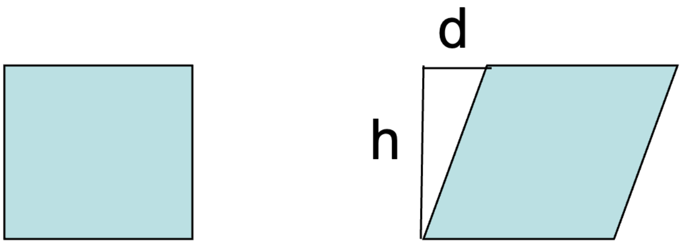

Figure 1.2: Small deformations in shear. - h is the undeformed length and d is the distance that the upper material points were translated parallel to the horizontal direction. Shear strain is defined by $\gamma = d/h \ll 1$.

For whatever amorphous material, a stress that generates a small shear strain does not modify the volume. The tangential stress σ is linked to γ by

$$\sigma = G\gamma, \tag{1.4}$$

where G is the shear modulus.

Among the three material constants so far introduced (G, E, μ) there exists a relationship, namely

$$E = 2G(1 + \mu). \tag{1.5}$$

Thus linear elasticity of amorphous materials is characterized by two material constants only. For the important case of volume-preserving materials, since $\mu = 1/2$, eq (1.5) becomes

$$E = 3G$$

and hence a single material constant, G or E, describes linear behavior.

1.1.2 Linear Viscous Properties

The viscosity is a property of the liquid state defined by Newton in 1687 (as quoted by Barnes et al.[10]) through the simple shear experiment schematically depicted in Figure 1.3. The liquid is confined between two parallel plates, the bottom plate being fixed while the top plate is allowed to slide over the liquid. In simple liquids like water the tangential force per unit area F/A, that is, the shear stress σ, required to move the upper plate is proportional to the plate velocity U, and inversely proportional to the gap H between the two plates, the proportionality constant being the viscosity η, that is,

$$\sigma = \eta \frac{U}{H} = \eta\dot{\gamma}, \tag{1.6}$$

where the velocity gradient $\dot{\gamma} = \frac{U}{H}$ is the shear rate. Eq (1.6) is known as Newton's law of viscosity, and fluids obeying eq (1.6) are called Newtonian.

Newtonian behaviour in experiments conducted at constant temperature and pressure has the following characteristics[10]:

- The only stress generated in simple shear flow is the shear stress, the two normal stress differences being zero.

- The shear viscosity does not vary with shear rate.

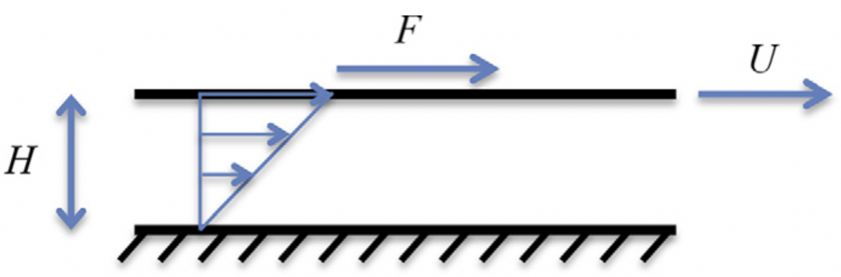

Figure 1.3: Shear flow between parallel plates. - U is the velocity of the upper plate.

- The viscosity is constant with respect to the time of shearing and the stress in the liquid falls to zero immediately the shearing is stopped. In any subsequent shearing, however long the period of resting between measurements, the viscosity is as previously measured.
- The viscosities measured in different types of deformation are always in simple proportion to one another, so, for example, the viscosity measured in a uniaxial extensional flow is always three times the value measured in simple shear flow.

A liquid showing any deviation from the above behaviour is non-Newtonian.

1.1.3 Linear Viscoelastic Properties

1.1.3.1 Step Strain Experiment

Many materials, especially polymeric ones, exhibit both elastic and viscous behavior. They are called viscoelastic. There exist viscoelastic solids and viscoelastic liquids, though sometimes the distinction can be difficult. To approach viscoelasticity, specifically linear viscoelasticity, let us start from the case of solids. These, when perfectly elastic, obey eq (1.4) in the general case. The crucial difference introduced by viscoelasticity is that the moduli G become time dependent. Limiting our discussion to the incompressible case, eq (1.4) becomes

$$\sigma(t) = G(t)\gamma \tag{1.7}$$

with the following meaning: At time t=0 a small strain γ is applied to the material element, and the strain γ is held constant therefrom. A stress immediately arises like in purely elastic solid: $\sigma(0) = G(0)\gamma$. Subsequently, however, the stress decays in time. The material function $G(t)$ is called relaxation (shear) modulus, and is always a decreasing function of time represented by the GreenKubo relations. The experiment to which eq (1.7) applies is called: stress relaxation after a step strain.

The relaxation process just described is irreversible, and dissipates at least part of the work done initially to deform the material element. To the dissipation accompanying a deformation we associate the word viscous. Therefore, materials obeying eq (1.7) in step strain are called viscoelastic. If the viscoelastic material to which eq (1.7) applies is a solid, then $G(t)$ in the course of time approaches a nonzero value, G_∞. That is, although stress decreases in time during relaxation, it will approach a value which then stays on forever as long as the configuration corresponding to the strain γ is maintained. The difference with respect to a perfectly elastic solid is that, for the viscoelastic case, the equilibrium stress associated to the strain γ is smaller than the initial stress $\sigma(0)$.

Eq (1.7) applies to viscoelastic liquids as well. For such a case, however, $G(t)$ decreases down to zero. Then, although the strain γ is held constant, in due time the stress σ vanishes entirely, the liquid material relaxing back to the isotropic equilibrium state. The work done initially is totally lost, and deformation is not recovered when the constraint imposing γ is removed. As shown next, though introduced for the particular case of a step strain, the material function $G(t)$ fully characterizes the linear viscoelastic response of incompressible materials.

1.1.3.2 Boltzmann Superposition Principle

We take the stress-free equilibrium configuration at $t = 0$ as the reference configuration. After that, we deform the material element progressively in time. Such a process can be described through the function $\gamma(t)$, which gives the shear strain at time t. For solids, we assume that γ remains small at all times. For liquids, we temporarily make the same assumption. Next, we try to find the stress σ at time t, given the fact that we know the relaxation modulus $G(t)$ of the material. The problem is that, while the strain is being augmented in time, thus generating additional stress, the stress due to previous strains is simultaneously relaxing. The strain increment is given by $\dot{\gamma}(t)\mathrm{d}t$, where $\dot{\gamma}(t)$ is the shear rate at time t.

t' is marked as any instant of time prior to present time t, when we want to know the stress $\sigma(t)$. The increment in strain between t' and $t' + \mathrm{d}t'$ in the past is given by $(t')\mathrm{d}t'$. Such a differential strain step has generated a differential stress $\mathrm{d}\sigma$ which, however, during the time interval between t' and t has relaxed somewhat, obeying the relaxation rule given by eq (1.7). Then, at the present time t, we expect that $\mathrm{d}\sigma$ has become:

$$\mathrm{d}\sigma(t) = G(t - t')\dot{\gamma}(t')\mathrm{d}t' \tag{1.8}$$

In view of linearity, we are entitled to sum over all such past contributions to the present stress (Boltzmann superposition principle). Hence:

$$\sigma(t) = \int_0^t G(t - t')\dot{\gamma}(t')\mathrm{d}t' \tag{1.9}$$

Eq (1.9) is the constitutive equation of linear viscoelasticity for incompressible materials (limited to shear deformations for simplicity).

The linear equations of viscoelasticity were obtained under the condition that the strain $\gamma(t)$ remains small. While such a condition is mandatory for the case of solids, it is not so for liquids. The asymptotic value is G_∞ for solids, while it is zero for liquids. Thus eq (1.9) only contains the shear rate $\dot{\gamma}(t)$, which means that $\gamma(t)$ can grow indefinitely (as it certainly does in a steady shear flow) as long as the shear rate $\dot{\gamma}(t)$ remains small for all values of t'. In other words, eq (1.9) also applies to flows for which the deformation grows without bounds provided they are sufficiently slow, so that the memory of large deformations is lost, and only small, more recent, relative strains contribute to the current stress.

In a steady shear flow, shear rate and shear stress are constant. Eq (1.9) then becomes:

$$\sigma(t) = \dot{\gamma} \int_0^t G(t - t')\mathrm{d}t' = \dot{\gamma} \int_0^\infty G(t)\mathrm{d}t. \tag{1.10}$$

Hence the viscosity is the integral over time of the relaxation modulus:

$$\eta = \int_0^\infty G(t)\mathrm{d}t. \tag{1.11}$$

1.2 Nonlinear Response of Polymers

1.2.1 Generalities on Linear Response

Linear response implies that the equilibrium microstructure of the material essentially remains the same in the non-equilibrium situation, and is only infinitesimally perturbed.

The observed stress is then proportional to some measure of such perturbation. The concepts of equilibrium microstructure and of perturbation are vague, but can be made more precise in specific materials.

In solid materials, for example, where atoms can be considered (aside from vibrations) as fixed in space, the microstructure is described by the interatomic distances, and a deformation indeed perturbs such distances. In liquids made of small molecules, since molecules are mobile, the microstructure can be the density distribution around each molecule, or the orientational distribution if the molecules are elongated, or both. These equilibrium distributions, usually isotropic, will be perturbed by flow. In suspensions, we may define the microstructure in a similar way, with reference to the suspended particles instead of molecules. In polymeric liquids and in rubber, since the molecules have a large number of internal degrees of freedom, the microstructure can be related to polymer conformations. And the examples could continue.

1.2.2 Why Linearity is Universal?

In spite of differences in microstructure, linearity of response is generally observed for small perturbations.

At equilibrium, the material is in a minimum of free energy. For whatever shape of the free-energy function, close to the minimum the shape is always parabolic (i.e., quadratic) in the state variables. Hence, the forces required to displace the material from its free-energy minimum, being the derivatives of the free energy (at constant temperature), are linear.

In the linear range, materials differ one from another only in the values of the proportionality constants. It should also be apparent that, since far from the minimum the shape of the free energy function will vary from one case to another, no universality of nonlinear behavior can be expected. Materials may then differ widely in their nonlinear behavior. At most, we can expect that materials that are similar in structure will show some sort of universal behavior, nevertheless limited to their specific category.

1.2.3 Why liquids respond nonlinearly?

From what we have said about linearity, it is to be expected that solids will respond nonlinearly if we deform them too much. However, what makes liquids, which are infinitely deformable, become nonlinear?

It is well known that the microstructure of a liquid can be described by distribution functions. When the fluid is set in motion, the velocity gradient acts in the direction of modifying the distributions prevailing at equilibrium. For example, rodlike molecules that are randomly oriented at equilibrium will tend to be aligned to some direction because of flow. On the other hand, thermal motion acts in the opposite direction, i.e., it attempts at re-establishing equilibrium.

The concept of relaxation will help us understand the competition between the external force and intrinsic thermal motion. The concept is more general: If the microstructure of a material has been modified by some cause, and then the cause is removed, the microstructure relaxes back to equilibrium. Hence, if flow is much slower than relaxation, then flow loses the competition. It only marginally perturbs the equilibrium microstructure of the liquid, and the response is linear. It is nonlinear otherwise.

1.2.4 Nonlinear Behavior Example: Shear Thinning

A well known example of nonlinear (or non-Newtonian) behavior is the shear thinning exhibited by most polymeric liquids in steady shear flows:

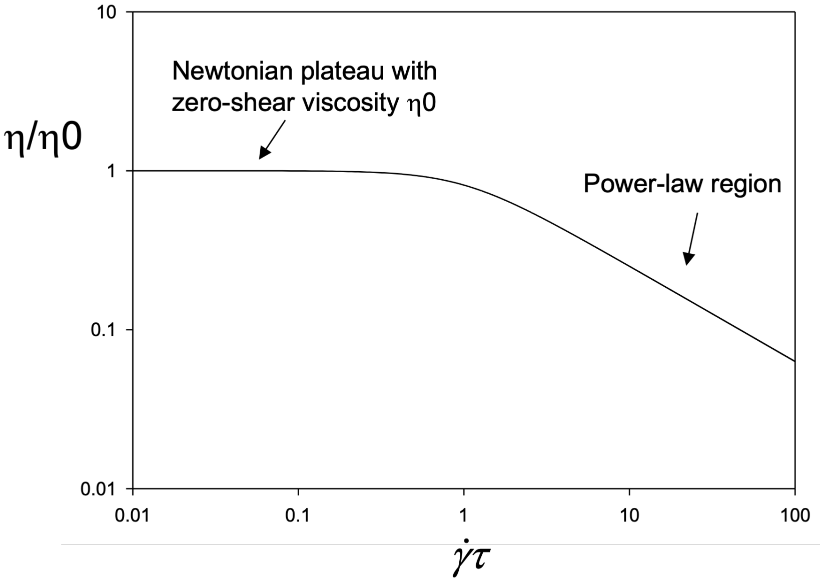

Figure 1.4: Illustration of shear thinning. - Steady-state shear viscosity normalized with zero shear viscosity as a function of non dimensional shear rate.

Cox and Merz (1958) [26] reported that the dependence of η on the shear rate (a nonlinear material function) happens to virtually coincide with the dependence of $|\eta^*|$ on frequency ω(a material function of linear viscoelasticity). This is known as the "Cox-Merz rule".

In summary, nonlinear behavior varies qualitatively from one system to another. Differently from the linear case, no general constitutive equation can be written that describes nonlinearities. Some generic (usually phenomenological) nonlinear constitutive equations , such as the power law for shear thinning fluids, only applies to some categories of materials, and only in some range of shear rates. Many phenomenological nonlinear constitutive equations have been proposed in the past that are occasionally useful for specific problems. Nonlinear constitutive equations are better derived by modeling the relevant physics of the specific material, or group of materials.

1.3 Friction Reduction due to Co-alignment of Polymer Chains in Fast Flows

Fast flows and large deformation rates typically are involved in polymer processing operations. As a consequence, the polymer flow properties during processing cannot be predicted from measurement of their linear viscoelastic functions, which merely describe relaxation from small deviations from equilibrium. In strong flows, the polymer molecular configurations depart strongly from their equilibrium configurations. For instance, this departing is encountered frequently in many processing operations such as fiber spinning and film blowing, which are operated in extensional flows [42].

Molecular modeling of the rheology of polymers in fast flow has been developed over many years starting from the fundamental contributions of Ianniruberto et al.[38, 55, 56], of Masubuchi et al.[86, 88] and of Watanabe et al.[90, 134]. Many years ago, Ianniruberto et al.[51] proposed that in polymer melts, the monomeric friction coefficient might change because of coalignment of the Kuhn segments (statistical chain monomers) under the action of fast flows, the phenomenon being in some way analogous to what occurs at the isotropic-to-nematic transition of liquid crystals. There followed several suggestions that indeed the effect existed, both from molecular dynamics simulations of styrene oligomer melts in shear flows[52] and from the analysis of extensional flow experiments on entangled and unentangled polystyrene melts and solutions[53, 90, 98, 139]. Dependence of the friction reduction effect on the polymer chemistry is also suggested in some works[86, 90, 92]. Even for a melt of Kremer-Grest chains, an indirect indication of a weak reduction of the friction coefficient with increasing molecular coalignment has been recently reported by Masubuchi et al.[88], who performed molecular dynamics simulations of stress relaxation following fast extensional flows. Finally, a recent analysis of shear (instead of extensional) data for unentangled polystyrene melts was added to the list[56].

In spite of the results reported in the papers just referred to, the flow-induced reduction of the friction coefficient is still highly controversial, partly because most of the evidence is indirect and also because the nonlinear rheology of polymers, especially if entangled, is very complex, encompassing several molecular dynamics mechanisms (e.g., see the reviews of Masubuchi[86] and of Larson and Desai[69]). For example, one of the more advanced molecular models for the rheology of entangled polymers[3] predicts an extensional viscosity of polystyrene melts that falls somewhat below the experimental data, despite the fact that the friction coefficient is kept constant in the model. Needless to say, the prediction worsens should the friction coefficient be assumed to decrease in fast flows. Such a consideration, clearly speaking against friction reduction, is also explicitly mentioned by Shahid et al.[118], while discussing possible nematic interactions between polymers and oligomeric solvents. Moreover, Wagner[130] models the nonlinear rheology of entangled polymer melts (seemingly successfully) without making use of any friction coefficient reduction. Wagners model is also taken up by Rasmussen[103], up to very recent times.[104] Finally, OConnor et al.[94] report molecular dynamics simulations of the relaxation following fast uniaxial extensional flows of entangled polymer melts, and their results show that the first stage of the relaxation occurs in a time comparable to the equilibrium Rouse time, seemingly with no sign of acceleration induced by a possible friction coefficient reduction.

Here, we hopefully solve the above-mentioned controversy by comparing the predictions of the Brownian dynamics simulations of the coarse-grained Fraenkel-chain model to KremerGrest (KG) molecular dynamics simulation results by Xu et al.[138]. In addition, the results reported by Xu et al. [138] are implemented to the very recent model proposed by Watanabee et al. [134], in which the roles of finite extensible nonlinear elasticity (FENE), friction-reduction, as well as brownian force intensity variation playing on the nonlinear flow behavior were studied.

1.4 Dynamics of Reversible Polymer Networks

Reversible polymer networks are formed by physical association of linear or branched polymers via reversible noncovalent bonds[30, 114, 116, 126], such as ionic interactions[21, 22, 33, 129], metalligand[78, 142, 143], π-π stacking, and hydrogen bonds[24, 34, 74, 75, 119, 136]. The reversibility of cross-linking provides them unique abilities for working as self-healing, stimuli-sensitive, and shape-memory materials. They also have superior processing and recycling properties over traditional polymers and chemical networks constructed from covalently cross-linked polymers owing to the sharp decrease in viscosity upon increasing temperature or decreasing concentration. The potential applications of supramolecular polymer networks have inspired strong interests in understanding the physical mechanisms underlying their structural, dynamic, and mechanical properties[30, 114, 116, 126].

The topological structures of supramolecular polymer networks are determined by the molecular composition of the back bones and the nature of the noncovalent interactions. The associating polymers which form supramolecular polymer networks can have multiple stickers distributed along their backbones. Each sticker can thus be cross-linked with several other polymers at well-separated bonding sites[33, 34]. The simplest and most widely studied supramolecular systems are those formed by the pairwise association of stickers[22, 108]. The polymers begin to aggregate into clusters which effectively work as cross-links in the transient network if the sticker functionality increases above two. Here, we only study the case where the sticker functionality is two. In spite of that, the complicated topological structures, together with the interplay between the dynamics of the parent polymer chains and the breaking/re-forming kinetics of the physical bonds, result in rich dynamic behavior of supramolecular polymer networks. The intrinsic characteristic times include the lifetime of the reversible stickers τ_s and the Rouse time τ_R in view that only unentangled polymers are taken into account here.

Theoretical models have been developed for describing the dynamic and rheological properties of supramolecular polymer networks in accordance with their structural classification[1, 11, 22, 27, 43, 73, 80, 107, 108, 108, 115]. For unentangled polymers with supramolecular side groups, the polymer type relevant to our work, the so-called sticky-Rouse model has been proposed [11, 22, 40, 73, 107]. A scaling theory based on the assumptions of pairwise association and hopping diffusion of stickers has also been developed to describe the self-healing process of unentangled supramolecular polymer networks[123]. Chen et al. [22] viewed the dynamics of associating polymers as two kinds of motional modes, i.e., low order chain motional modes (Rouse-like, through breaking and reformation of reversible crosslinks) and high order Rouse modes (delayed by ion associations with lifetime τ_s). On the basis of Chen et al.'s work [22], Cui et al. [27] made several improvements by taking dangling effects into account and introducing the so-called "hop" distance. Even though the predictions of their models are able to capture the main features of the viscoelastic response of associating polymers, discrepancies still appear in the intermediate frequency range of the LVE response, i.e., in the region where data exhibit a rubbery plateau in the elastic modulus, and a minimum in the loss modulus. More importantly, their models typically predict more pronounced than shown by the data at the intermediate frequency regarding the minimum of the loss modulus.

Here, we investigate the dynamics of the reversible polymer networks by using the multi-chain model and the single-chain model. The multi-chain model has the capabilities to predict the evolution of the topological structure so that we can estimate the phase separation according to the local chain density. Due to the natural characterization of the time correlation, it usually takes several days to obtain relatively good results. Particularly, one hardly waits for the terminal relaxation time. On the other hand, the single-chain model is a time-saving one even though we can only implicitly know the topological structure of polymer networks through conformational quantities. More importantly, the predictions of our single-chain model have a good agreement with data, especially at the intermediate frequencies.

1.5 Thesis Outline

This Ph.D project is part of the DoDyNet (Double Dynamics for Design of New Responsive Polymer Networks and Gels) project which is funded under the Initial Training Network of Marie Curie Programme in the European Union HORIZON 2020 Framework. The scientific objective of DoDyNet is to obtain a fundamental understanding of the synergistic effects arising by combining distinct dynamic modes within a polymeric network. As part of DoDyNet, this Ph.D project focuses on modeling the dynamics of reversible polymer networks and modeling the nonlinear rheological behavior of unentangled polymer melts under fast flows. The aim of this Ph.D project is to study the effects of sticker related factors (sticker distribution, density, and lifetime etc.) on the viscoelastic response of the transient polymer networks and explore the mechanisms of friction reduction happening in fast flows through modeling and simulation approaches.

Chapter 2 and 3 deal with the dynamics of reversible polymer networks. Chapter 2 starts with the periodic simulation box. Then the Smoluchowski approach and Langevin approach are given. At the same time, our model is introduced. The effects of the lifetime, density, and distribution of stickers on the dynamics of associating polymers are studied. Meanwhile, the comparison between the predictions of our model and that of the sticky Rouse model is made.

Chapter 3 first displays the mathematical model. Then the results were applied to examine the data reported by Lewis et al.[74] referring to the unentangled polydisperse poly-butyl acrylate (PBA) melts (both with and without stickers). Meanwhile, the polydispersity effect is studied. Next, the results are compared with the LVE data of Cui et al.[27], where the glassy contribution is taken into account.

Chapter 4 and 5 deal with the friction reduction of unentangled melts under flows. Chapter 4 first illustrates the physics of deformed polymer under flows in the Introduction. Then a few finitely extensible nonlinear elastic (FENE) models and the flow-induced friction reduction are given in the same section. Later, a rich set of data of Kremer-Grest melts in fast steady shear flows is presented. Next, Watanabe's model is briefly presented and the above data are applied to this model.

Chapter 5 begins with the assumption that the beads are endowed with isotropic friction. In this section, the Fraenkel-chain model is shown first. Then the predictions are compared with the data. Discussions are given at the same time. The next section proposes that the beads are endowed with anisotropic friction. In this section, the theory is presented first. The results are compared with the data as well as the results of the isotropic friction reduction model both for the conformation data and the viscometric functions.

2

A Multi-chain Model for the Linear Viscoelasticity of Unentangled Associating Polymer Melts

2.1 Introduction

Associating polymers are made of covalent chains connected through noncovalent bonds[30, 114, 116, 126], such as ionic interactions[21, 22, 33, 129], metalligand[78, 142, 143], π-π stacking, and hydrogen bonds[24, 34, 74, 75, 119, 136]. The ability to vary and control the interactions in supramolecular systems provides an efficient tool to tune the structure, dynamics, and rheology [19, 44, 106]. This ability stems from different lifetimes, densities and distribution of stickers along the chain.

The physical meaning of the lifetime of stickers is the bonding energy that enables two stickers to be associated. The thermal energy at room temperature and pressure is around $k_BT = 2.5kJ \cdot mol^{-1}$. The energy of a covalent bond is typically larger than $100kJ \cdot mol^{-1}$. Therefore, the polymer chains connected through covalent bonds are stable at room temperatures and pressures. In contrast, the bonding energies of hydrogen bonding, ionic, or van der Waals interactions are comparable with the thermal energy at room pressure and temperature[15, 59]. Therefore, the networks formed by these bonds are reversible. The reversibility is crucial for materials to fulfill the functions of self-healing, stimuli responsive, and shape memory[91, 144]. Moreover, both touching and detaching are physiologically important in folding and unfolding of proteins, where the reversible bonds play a pivotal role[60].

The density of stickers makes a difference as well. Callies et al. [20] investigate systematically the viscoelasticity of supramolecular center-functionalized linear poly(n-butyl acrylate) (PnBA) chains as a function of density of stickers. At a certain threshold, the density of stickers is supposed to lead to a transition between two kinds of dynamics. Specifically, above the threshold, the density of stickers should be high enough to allow self-assembly into large aggregates and the rheological properties should be regulated by the scission and relaxation of these aggregates. On the other hand, below the threshold, the stickers are dispersed in the PnBA melt and should behave as localized and transient attachment points between chains.

The distribution of stickers has an effect on the structure and physical properties of associating polymers. Radi et al. [100] supposed that dangling chain ends result in imperfections in the associating polymers, which lower the crosslink density, thereby reducing elastic recovery and increasing the solvent swelling. Martin et al.[83] confirmed that the dangling chains act as a network defect and decrease crosslink density depending on the number and length of these dangling chains. This decrease in the crosslink density leads to reduced mechanical properties[131] as well as greater swelling of the network in an active solvent environment. In an amorphous polymer network such as a vulcanized elastomer, the number of dangling chains leads to an increase in the relaxation time[28, 83] and poor elastic recovery. Control of the number and type of dangling chains can lead to useful properties.

This study attempts to investigate the effects of the lifetime, density and distribution of stickers on the viscoelastic response of associating polymers by using a multi-chain model. This Chapter is scheduled as follows. Section 2.2 introduces the periodic simulation box. The Lees-Edwards sliding bi-periodic box is illustrated, which makes it possible to simulate polymer melts under shear flow at a molecular scale. Section 2.3 gives background of Smoluchowski approach and Langevin approach, as well as the sticky Rouse model and the multi-tau algorithm. Section 2.4 discusses the predictions of the model and compares the results with Chen et al.'s model[22]. Section 2.5 summarizes the whole Chapter.

2.2 Periodic Simulation Box

When it comes to the multi-chain model, we can not avoid the simulation box. Taking into account the finite size of model/simulation box is crucial to compute correctly many of the structural characteristics (e.g. bead-spring statistics) of the system being studied since the size of the system is limited by the available storage on the host computer, and, more crucially, by the speed of execution of the program.

The importance of the finite size of the model box can be illustrated using a 1 dm^3 edged cube of water (1 L) at room temperature. This cube contains approximately 3.3×10^{25} water molecules, each of them can be considered as a sphere having a diameter of 2.8 $\AA$. Following this scheme surface interactions can affect up to 10 layers of spheres (water molecules) far from the surface of the model cubic box. In this case the number of water molecules exposed to the surface is about 2×10^{19}, which is a small fraction of the total number of molecules in the model.

Currently, simulations are usually performed on a small number of molecules, somewhere from 1 thousand to several thousands of molecules/atoms. As a result a very substantial fraction of them may be influenced by the finite size of the simulation/model box. The problem of surface effects is approached by implementing the so-called Periodic Boundary Conditions "PBC"[18], which means surrounding the simulation box with its translational images in the 3 directions of space. The cubic box is replicated throughout space to form an infinite lattice. In the course of the simulation, as a molecule moves in the original box, its periodic image in each of the neighbouring boxes moves in exactly the same way. Thus, as a molecule leaves the central box, one of its images will enter through the opposite face. There are no walls at the boundary of the central box, and no surface molecules. This box simply forms a convenient axis system for measuring the coordinates of the N molecules.

The Periodic Boundary Conditions have been implemented successfully over the past few years to predict the equilibrium behaviour of a macroscopic system from that of a small model. The consideration of various correlation functions offers a rigorous approach to the evaluation of transport coefficients provided one is close to thermal equilibrium. (It should, however, be stated that any study of transport phenomena is extremely demanding in terms of machine time.) However if one is far from equilibrium the correlation function approach is inapplicable, as are purely analytic approaches. If the periodic boxes are stationary, it cannot reveal the time dependent properties or the behaviour of a system under really extreme conditions.

In 1972 Lees and Edwards[72] proposed a bi-periodic domain concept for Molecular Dynamics simulations by describing sliding boundary conditions for simple shear flow, which is nowadays called the Lees-Edwards boundary condition (LEbc). Hwang et al. (2003)[49] combined the sliding bi-periodic domain concept of Lees and Edwards[72] with a standard velocity-pressure formulation of a fictitious-domain/finite-element method by introducing sliding bi-periodic frame constraints. A two-dimensional version of such a periodic system under shear flow is shown in Figure 2.1. The periodic system can be applied in equilibrium problems by setting the shear rate $\dot{\gamma} = 0$.

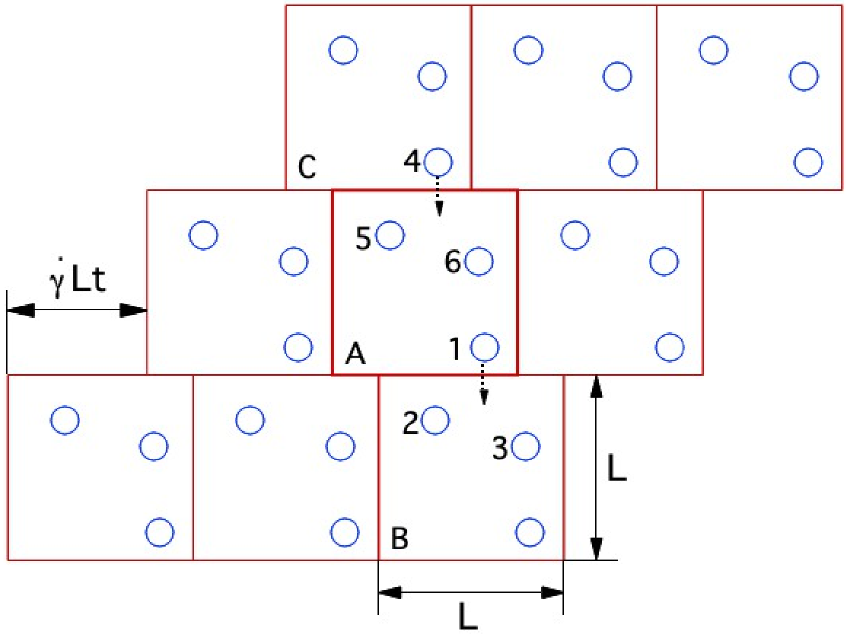

Figure 2.1: Illustrates the principle of the periodic boundary conditions used in shear flow: a particle which goes out from the simulation box by one side is reintroduced in the box by the opposite side (in the 2 dimension of space). - $\dot{\gamma}$ is the shear rate and L is the length of the box.

In Figure 2.1, the Cartesian coordinates in the plane are specified in terms of the x coordinate axis (horizontal)and the y-coordinate axis (vertical) with the intersection point at the bottom left corner of box A. The kinematic relations for the horizontal periodicity and the sliding periodicity are written in eqs (2.1) and (2.2), respectively:

$$v_x(x+nL,y)=v_x(x,y),\quad x\in(0,L),\quad y\in(0,L),\quad n\in N. \tag{2.1}$$

$$v_x(x+n\dot{\gamma}Lt,y+nL;t)=v_x(x,y;t)+n\dot{\gamma}L,\quad x\in(0,L),\quad y\in(0,L),\quad n\in N, \tag{2.2}$$

which means middle row boxes remain static, while the upper row boxes or the bottom row boxes are moving toward right or left at the speed of $\dot{\gamma}L$, respectively. To illustrate eqs (2.1) and (2.2) explicitly, Figures 2.2-2.6 show the boxes position and the particles location at different time, where the blue circles or boxes indicate the particles or boxes location at $t=0$ and the red circles or boxes refer to the current particles or boxes location.

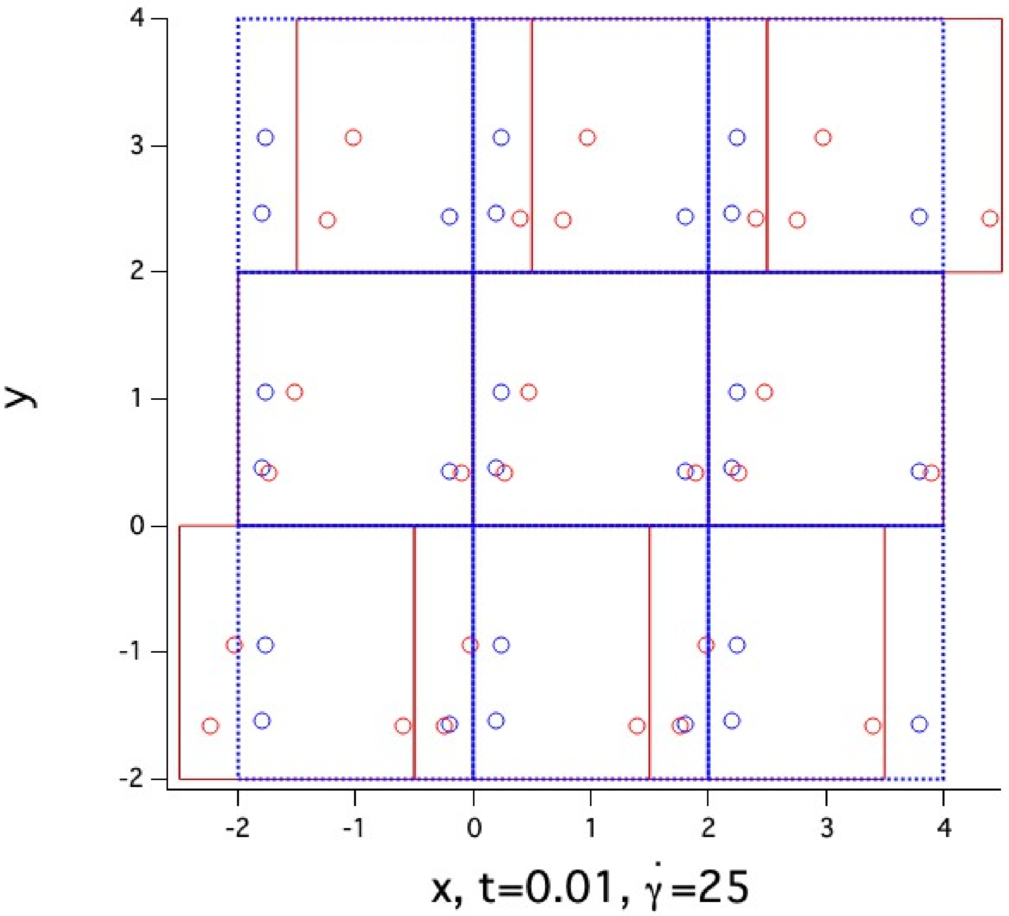

Figure 2.2: Illustration of periodic boxes movement under shear flow - $t=0.01, \dot{\gamma}=25$

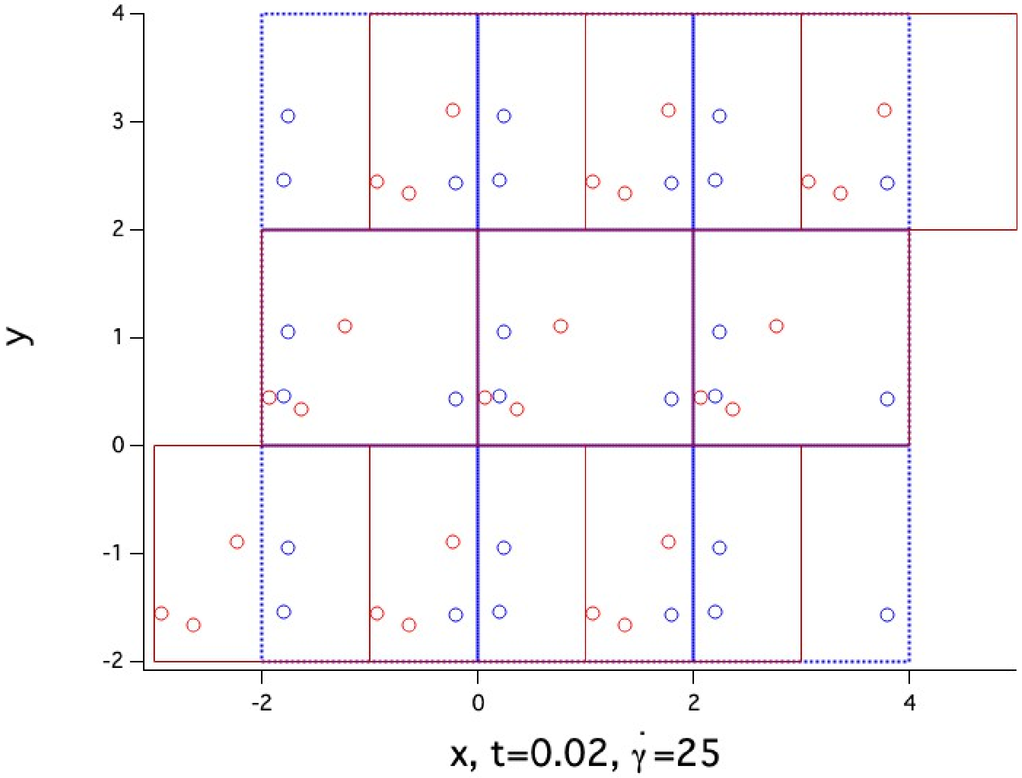

Figure 2.3: Illustration of periodic boxes movement under shear flow - $t = 0.02, \dot{\gamma} = 25$

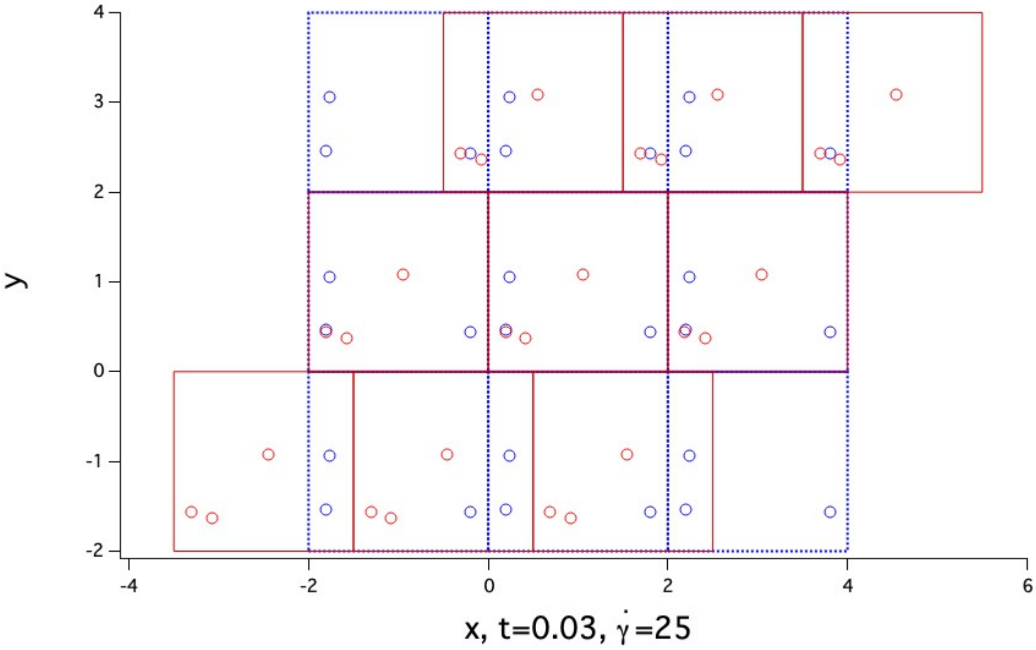

Figure 2.4: Illustration of periodic boxes movement under shear flow - $t = 0.03, \dot{\gamma} = 25$

As particle 1_A moves through a boundary, its images 4_C (where the subscript specifies in which box the image lies) move across their corresponding boundaries. The number density in the central box A (and hence in the entire system) is conserved. It is not necessary to store the coordinates of all the images in a simulation (an infinite number!), just the molecules in the central box (However, when particle interactions are not negligible, the coordinates of the particles in surrounding boxes (8 boxes for the 2-D problem) are usually necessary to be stored as well). When a molecule leaves the box by crossing a boundary, attention may be switched to the image just entering. It is sometimes useful to picture the basic simulation box (in our two-dimensional example) as being rolled up to form the surface of a three-dimensional torus or doughnut, when there is no need to consider an infinite number of replicas of the system, nor any image particles. This correctly represents the topology of the system, if not the geometry. A similar analogy exists for a three-dimensional periodic system.

It is important to ask if the properties of a small, infinitely periodic system and the macroscopic system which it represents are the same. This will depend both on the range of the intermolecular potential and the phenomenon under investigation. The

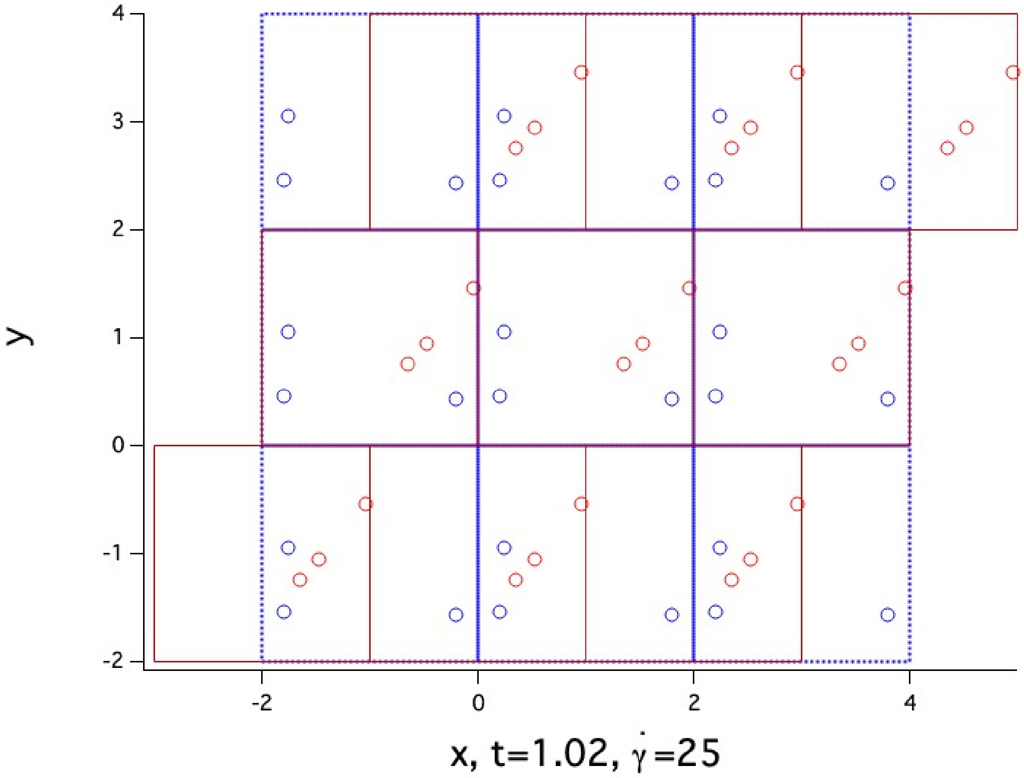

Figure 2.5: Illustration of periodic boxes movement under shear flow - $t = 1.02, \dot{\gamma} = 25$

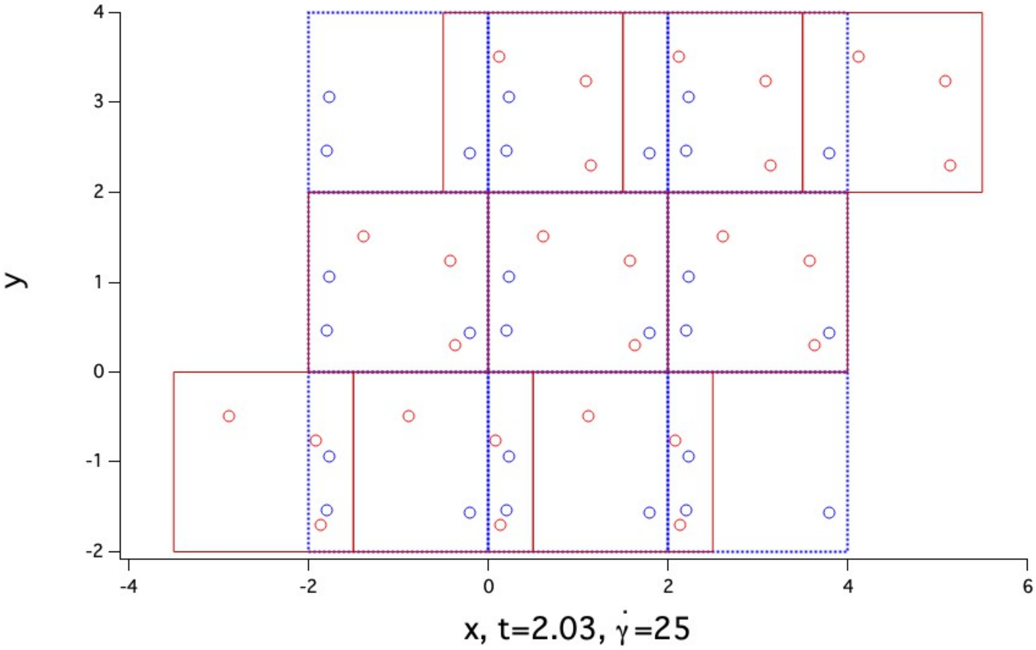

Figure 2.6: Illustration of periodic boxes movement under shear flow - $t = 2.03, \dot{\gamma} = 25$

common experience in simulation work is that periodic boundary conditions have little effect on the equilibrium thermodynamic properties and structures of fluids away from phase transitions and where the interactions are short-ranged. It is always sensible to check that this is true for each model studied. If the resources are available, it should be standard practice to increase the number of molecules (and the box size, so as to maintain constant density) and rerun the simulations. In addition, Pratt and Haan (1981) [99] have developed theoretical methods for investigating the effects of boundary conditions on equilibrium properties.

The cubic box has been used almost exclusively in computer simulation studies because of its geometrical simplicity.

2.3 Molecular Approach

As we mentioned in the Introduction, the nonlinear behavior of polymers varies qualitatively from one system to another and no general constitutive equation can be written that describes nonlinearities. However, the molecular approach has generalities and can be applied to different systems. The most famous model is the bead-spring model. Figure 2.7 shows the Dumbbell model, where two friction beads are connected by a spring. The beads account for the viscous, dissipative properties of the polymer, while the elastic spring accounts for the connectivity of the molecule and for its entropic elasticity[50].

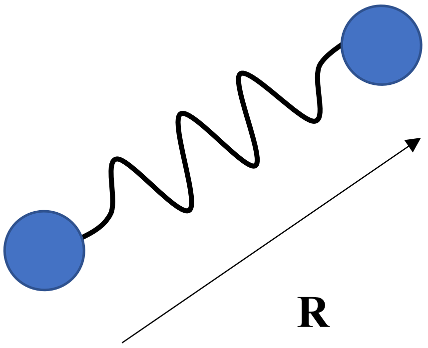

Figure 2.7: Dumbbell model. - ***R*** is the end-to-end vector.

2.3.1 Smoluchowski Approach and Langevin Approach

The motion of polymer chains is also affected by thermal agitation. This Brownian motion dominates various time-dependent phenomena in polymer melts such as viscoelasticity and diffusion. This motion is regularly regarded as a kind of stochastic process from a phenomenological point of view, i.e., constructing a phenomenological equation describing Brownian motion based on known macroscopic laws. The phenomenological equation for Brownian motion has two seemingly different, but essentially the same, forms: the Smoluchowski equation and the Langevin equation.

- Smoluchowski approach

  The Smoluchowski equation is derived from the diffusion equation and has the following form.:

$$\frac{\partial \Psi}{\partial t} = \frac{\partial}{\partial \mathbf{R}} \cdot \left[D\frac{\partial \Psi}{\partial \mathbf{R}} + \Psi D \frac{\partial}{\partial \mathbf{R}}\Big(\frac{E}{k_B T}\Big)\right] - \frac{\partial}{\partial \mathbf{R}} \cdot (\Psi \mathbb{K} \cdot \mathbf{R}), \tag{2.3}$$

where E is the elastic energy, $\mathbb{K}$ is the velocity gradient and D is the diffusion coefficient. At equilibrium, $\Psi(\mathbf{R}, t)$ is isotropic and Gaussian distribution function. When D does not vary with $\mathbf{R}$, we can easily compute the term $\langle\mathbf{RR}\rangle$ by

$$\frac{\mathrm{d}\langle\mathbf{RR}\rangle}{\mathrm{d}t} = 2D\mathbb{I} - \frac{6D}{R_0^2}\langle\mathbf{RR}\rangle + \mathbb{K}\cdot\langle\mathbf{RR}\rangle + \langle\mathbf{RR}\rangle\cdot\mathbb{K}^{\mathrm{T}}. \tag{2.4}$$

- Langevin approach

  The Langevin approach describes Brownian motion by including the random force $\mathbf{f}$ explicitly. For the dumbbell model, the Langevin equation is written as:

$$\zeta\Big(\mathbb{K}\cdot\mathbf{R} - \frac{\mathrm{d}\mathbf{R}}{\mathrm{d}t}\Big) - H\mathbf{R} + \mathbf{f} = \mathbf{0}. \tag{2.5}$$

For the Rouse model (C.F. Figure 2.8), the Langevin equation reads:

$$\begin{cases} \zeta\frac{\mathrm{d}\mathbf{R}_1}{\mathrm{d}t} = -H(\mathbf{R}_1 - \mathbf{R}_2) + \zeta\mathbb{K}\cdot\mathbf{R}_1 + \mathbf{f}_1, \text{if } n=1 \\ \zeta\frac{\mathrm{d}\mathbf{R}_n}{\mathrm{d}t} = -H(2\mathbf{R}_n - \mathbf{R}_{n+1} - \mathbf{R}_{n-1}) + \zeta\mathbb{K}\cdot\mathbf{R}_n + \mathbf{f}_n, \\ \quad \text{if } n = 2, ..., N-1 \\ \zeta\frac{\mathrm{d}\mathbf{R}_N}{\mathrm{d}t} = -H(\mathbf{R}_N - \mathbf{R}_{N-1}) + \zeta\mathbb{K}\cdot\mathbf{R}_N + \mathbf{f}_N, \text{if } n=N \end{cases} \tag{2.6}$$

where $H = 3k_BT/R_0^2$ and R_0 is the end-to-end distance for a subchain at the equilibrium state, $\mathbf{f}_n$ is the random force characterized by

$$\begin{aligned} &\langle\mathbf{f}_n(t)\rangle = 0, \\ &\langle f_{n\alpha}(t) f_{m\beta}(t')\rangle = 2\zeta k_BT\delta_{nm}\delta_{\alpha\beta}\delta(t-t'). \end{aligned} \tag{2.7}$$

Figure 2.9 shows that the Smoluchowski approach is equivalent to the Langevin approach, neglecting the fluctuation caused by Brownian motion. The Langevin equation is preferable insofar as it is capable of describing wider classes of stochastic processes[71].

2.3.2 Microscopic Expression for the Stress Tensor and the Relaxation Modulus

- Microscopic expression for the stress tensor

  It can be shown that the stress tensor $\boldsymbol{\sigma}$ contributed by an ensemble of Rouse chains is equal to

$$\boldsymbol{\sigma} = \nu H\langle\sum_{n=1}^{N-1}(\mathbf{R}_{n+1} - \mathbf{R}_n)(\mathbf{R}_{n+1} - \mathbf{R}_n)\rangle, \tag{2.8}$$

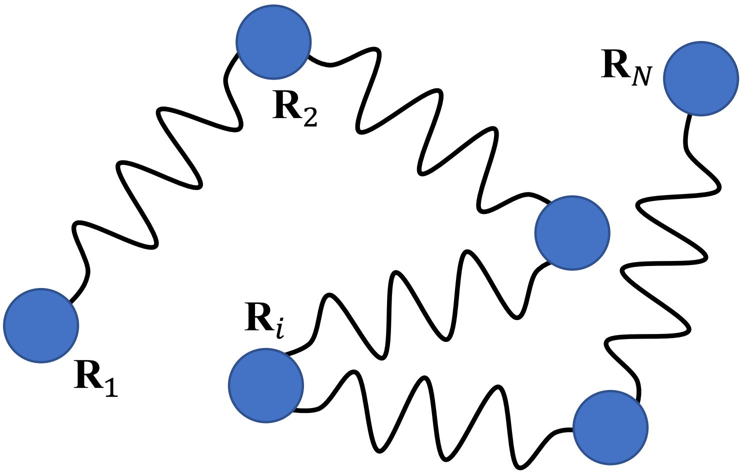

Figure 2.8: Rouse model. - $\boldsymbol{R}_i$ is the position vector of i-th bead.

where ν is the number density of molecules.

- Microscopic expression for the relaxation modulus

$$G(t) = \frac{V}{k_B T}\langle \sigma_{xy}(t+\tau)\sigma_{xy}(\tau)\rangle_\tau = \nu k_B T \sum_{p=1}^{N-1} \exp(-2t/\tau_p), \tag{2.9}$$

where $H = 3k_B T/R_0^2$ and τ_p is written as

$$\tau_p = \frac{2\zeta}{H}\left[4\mathrm{sin}^2\left(\frac{p\pi}{2N}\right)\right]^{-1}. \tag{2.10}$$

It should be noted that the term $\langle \sigma_{xy}(t+\tau)\sigma_{xy}(\tau)\rangle_\tau$ appearing in eq (2.9) is a time correlation function revealing relaxation properties of polymer chains. In order to improve the response signal, many values of the stress $\sigma_{xy}(t)$ are typically used. Thus, the calculation of time correlation functions frequently consumes significant CPU time and memory resources. Recently developed efficient methods[79, 101, 102], i.e. the multi-tau correlator algorithm, have made this computation significantly easier.

2.3.3 Sticky Rouse Model

The sticky-Rouse model is based on the idea that stickers along the chain provide an additional effective drag, delaying the terminal relaxation time, schematically depicted

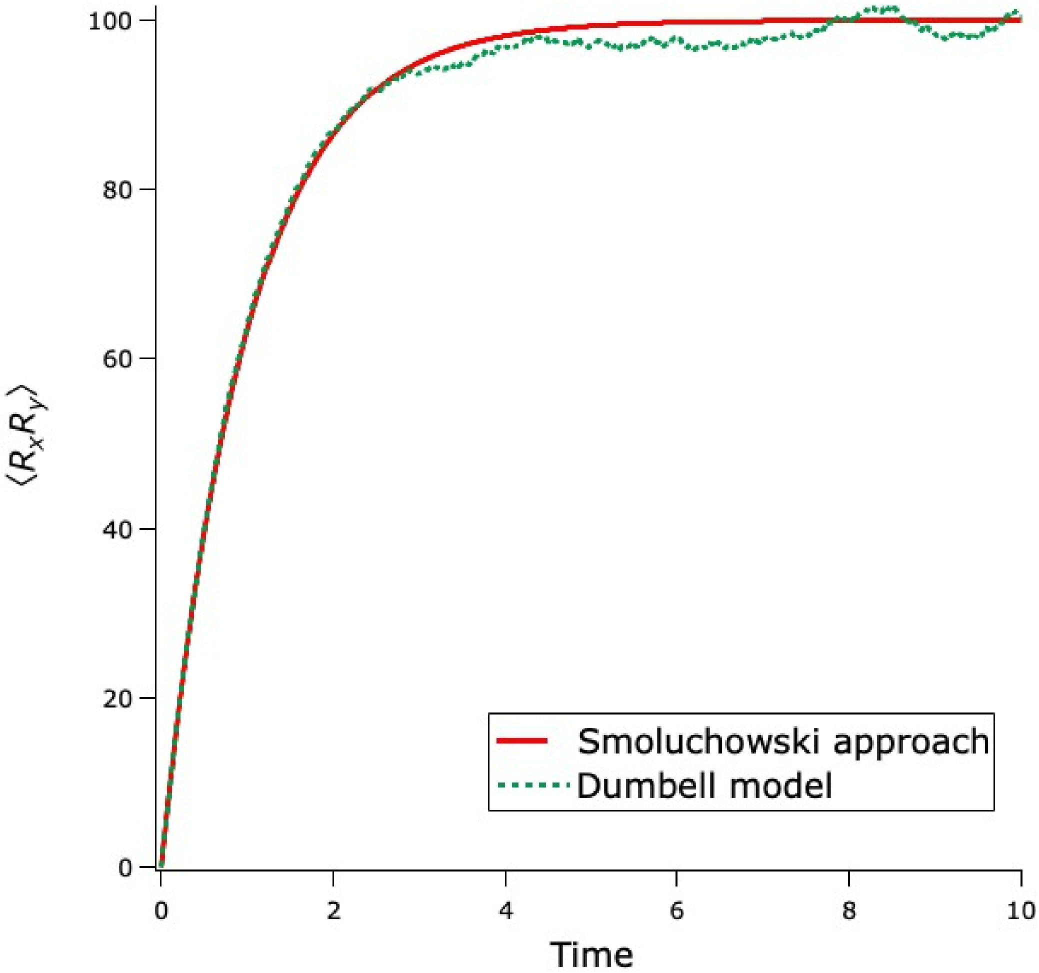

Figure 2.9: Comparison of Smoluchowski approach and Langevin approach. - $\langle R_x R_y \rangle$ as a function of time.

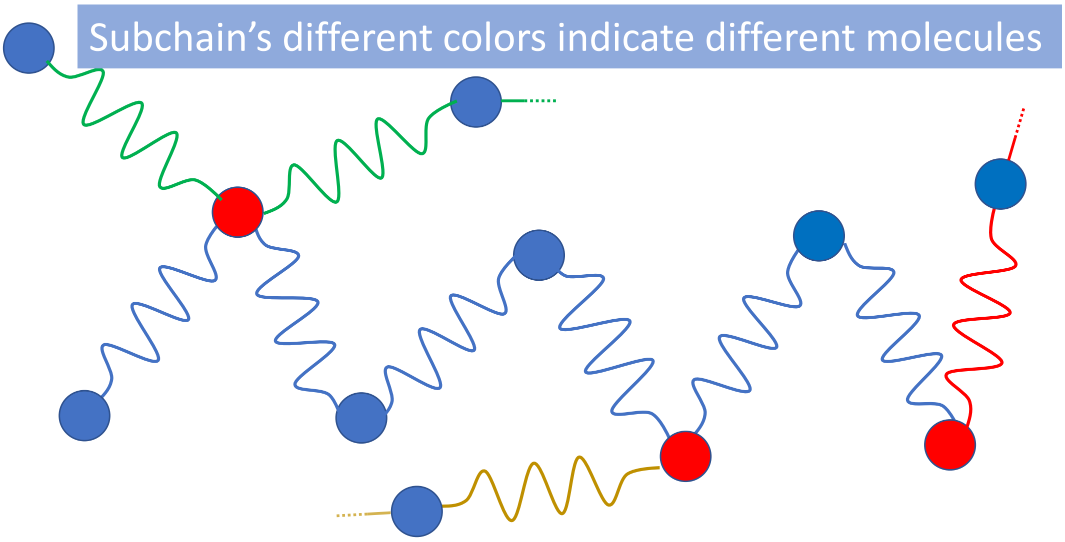

Figure 2.10: Sticky Rouse model. - The sticker functionality is two.

in Figure 2.10. Accordingly, a larger value of friction coefficient ζ_s will be adopted, compared with the ordinary bead friction ζ.

The delaying effect can be taken into account either by the drag force from associated polymer chains (C.F. Figure 2.11) or by assigning a larger value of friction coefficient ζ_s, compared with the ordinary bead friction ζ.

In the former method, we suppose that when the distance of two stickers, which are from different chains, is less than d_c, they are associated and they are relocated to the middle point. After the lifetime t_c, the limitation is released and they are in free status.

Figure 2.12 illustrates the chain's movements in the periodic simulation boxes.

2.4 Linear Viscoelastic Response of Polymer Networks

Figure 2.13 shows the nondimensional results of shear relaxation modulus $G(t)$. The yellow, gray, and black curves clearly indicate that the number of stickers N determines the level of the second plateau. Furthermore, these three curves imply that a more significant time delay at the end will be found for a larger friction ratio ζ_s/ζ. The red and gray curves (or pink and yellow curves) indicate that the G(t) prediction has a higher second plateau for the the chain with more stickers. The blue and pink

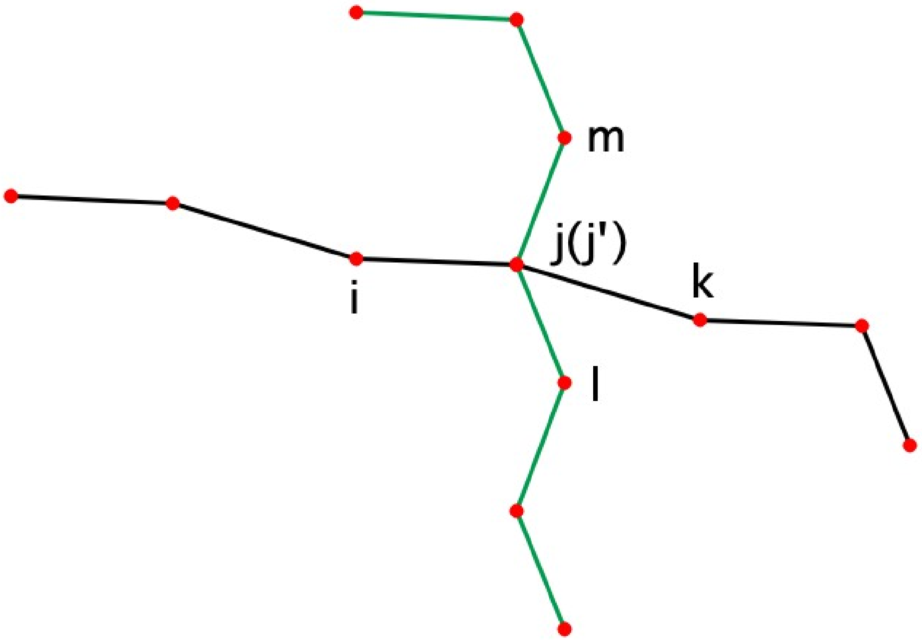

Figure 2.11: Two associated chains. - The bead j is the associated bead. The friction coefficient of bead j is two times of that of the ordinary bead.

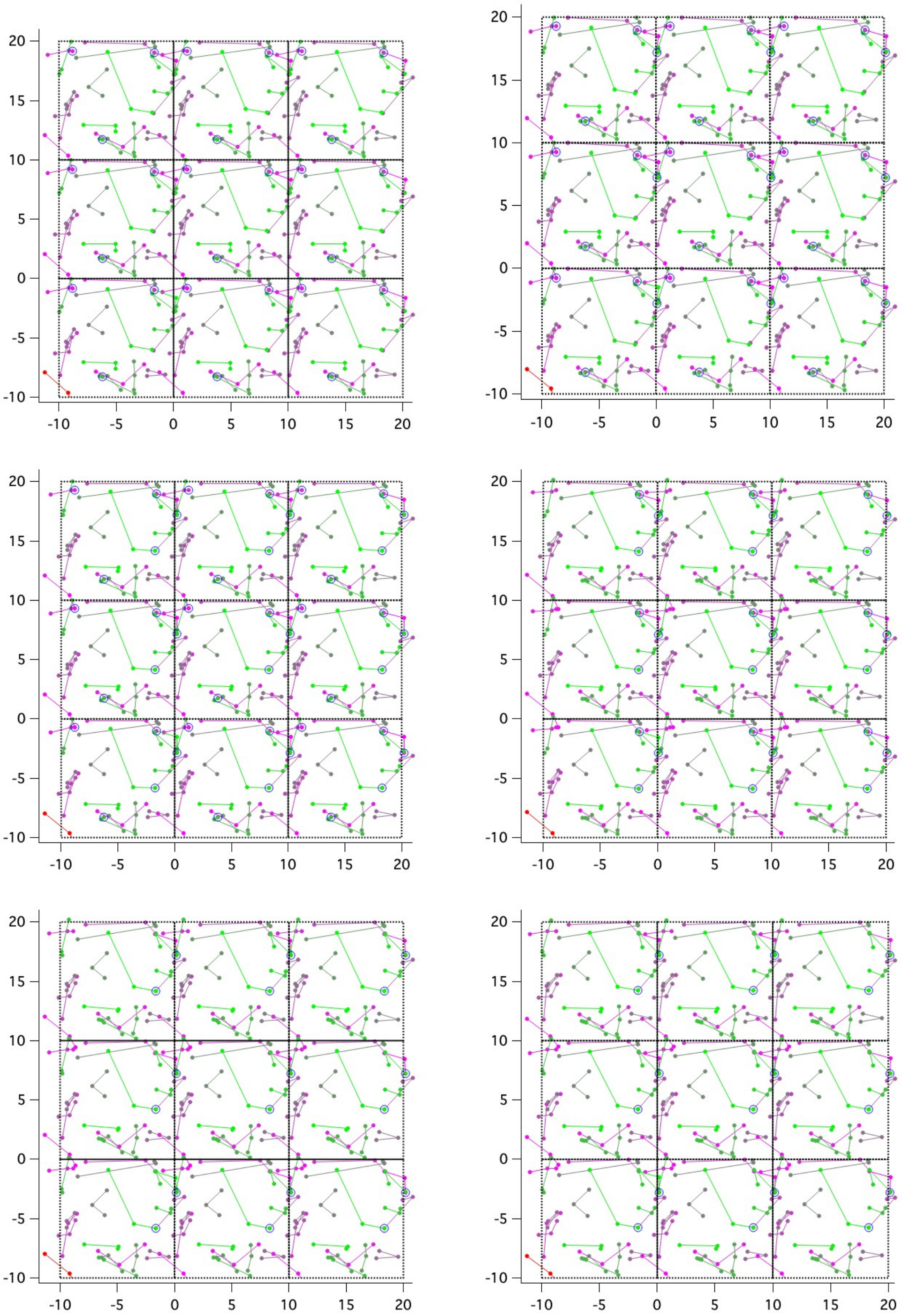

Figure 2.12: The conformations of polymer chains in the periodic simulation boxes. - Blue circles refer to associating stickers. 3 beads per chain with 2 stickers. Box size: 10×10. $d_c = 0.2$, $t_c = 0.05$, time step: 0.01. From up left to down right: t= 5.9-t=5.95.

curves implies that the distributions of stickers make a difference to the relaxation modulus results. At the second plateau, the $G(t)$ prediction of the chains with random distribution of stickers is slightly higher than that of the chains with fixed distribution of stickers, which means the random distribution of stickers amplifies the effect caused by stickers, compared with the fixed distribution of stickers. The green and grey curves show that a vertical shift factor is enough when the $G(t)$ predictions of a longer chain is traslated to that of a shorter chain.

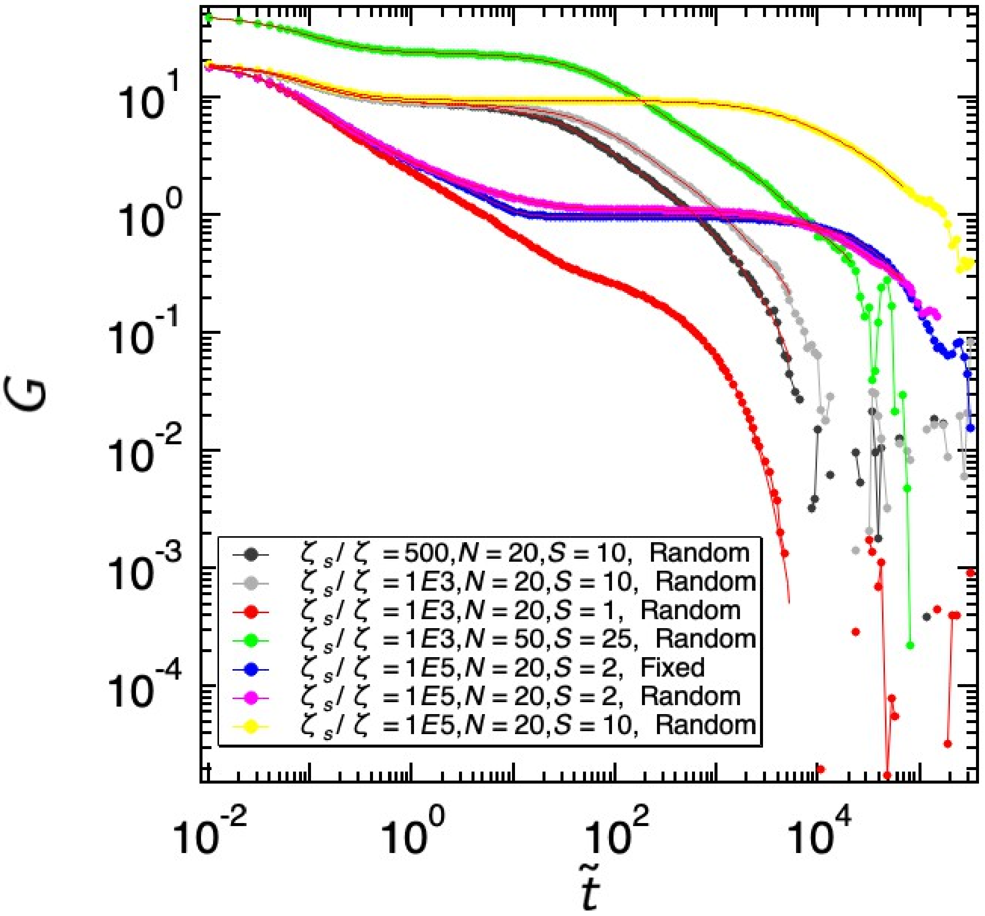

Figure 2.13: Comparisons of shear relaxation modulus for different friction ratio ζ_s/ζ, number of beads N, number of stickers S, and distribution of stickers. - Hereinafter, "Random" and "Fixed" indicate the distribution of stickers.

Figure 2.14 displays the nondimensional predictions of the storage and loss moduli. From Figure 2.14, we can have a whole picture of the effects of distribution of stickers, number of stickers, and friction ratio on the viscoelastic response. To illustrate these effects clearly, we plot them separately.

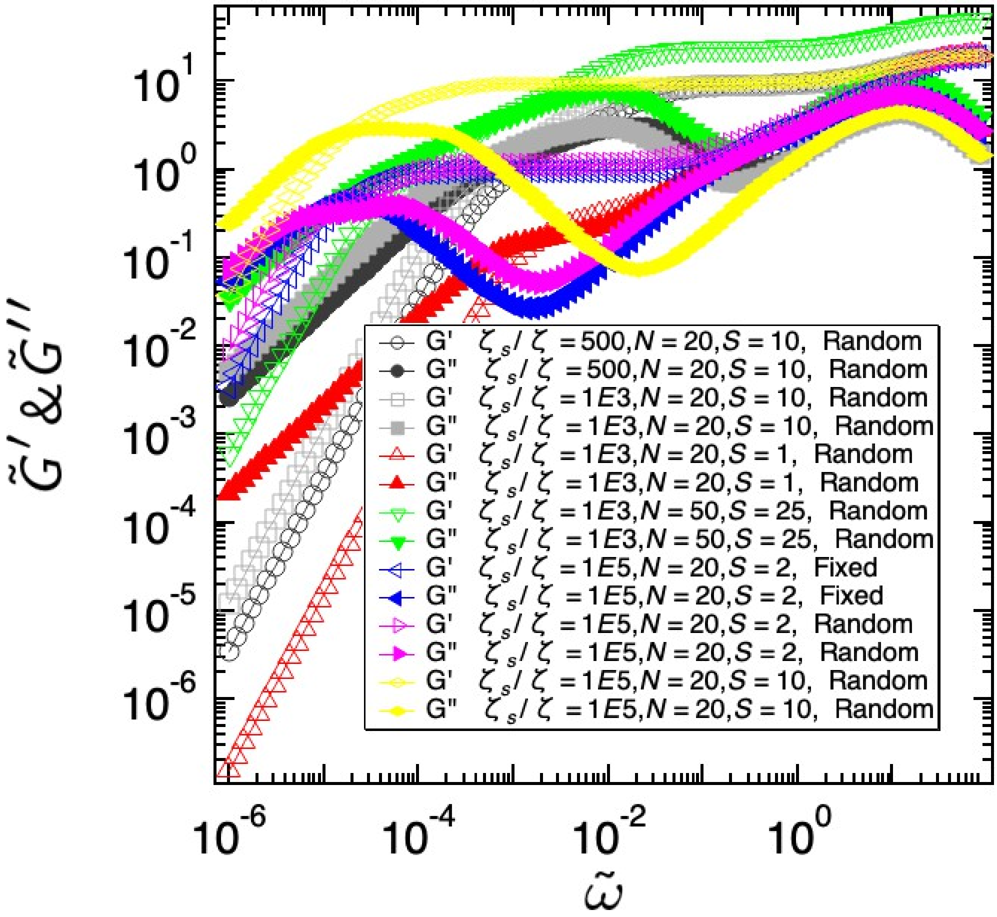

Figure 2.14: Comparisons of linear viscoelastic master curves for different friction ratio ζ_s/ζ, number of beads N, number of stickers S, and distribution of stickers. -

Figure 2.15 shows the effects of the distribution of stickers. The $G''(\omega)$ prediction of the chain with fixed distribution of stickers shows a lower minimum at the intermediate frequency.

Figure 2.16 shows the effects of the number of stickers. The $G'(\omega)$ prediction of the chain with more stickers shows a higher plateau of the intermediate frequencies. In addition, it displays a longer time delay at the low frequencies than that of the chain with less number of stickers.

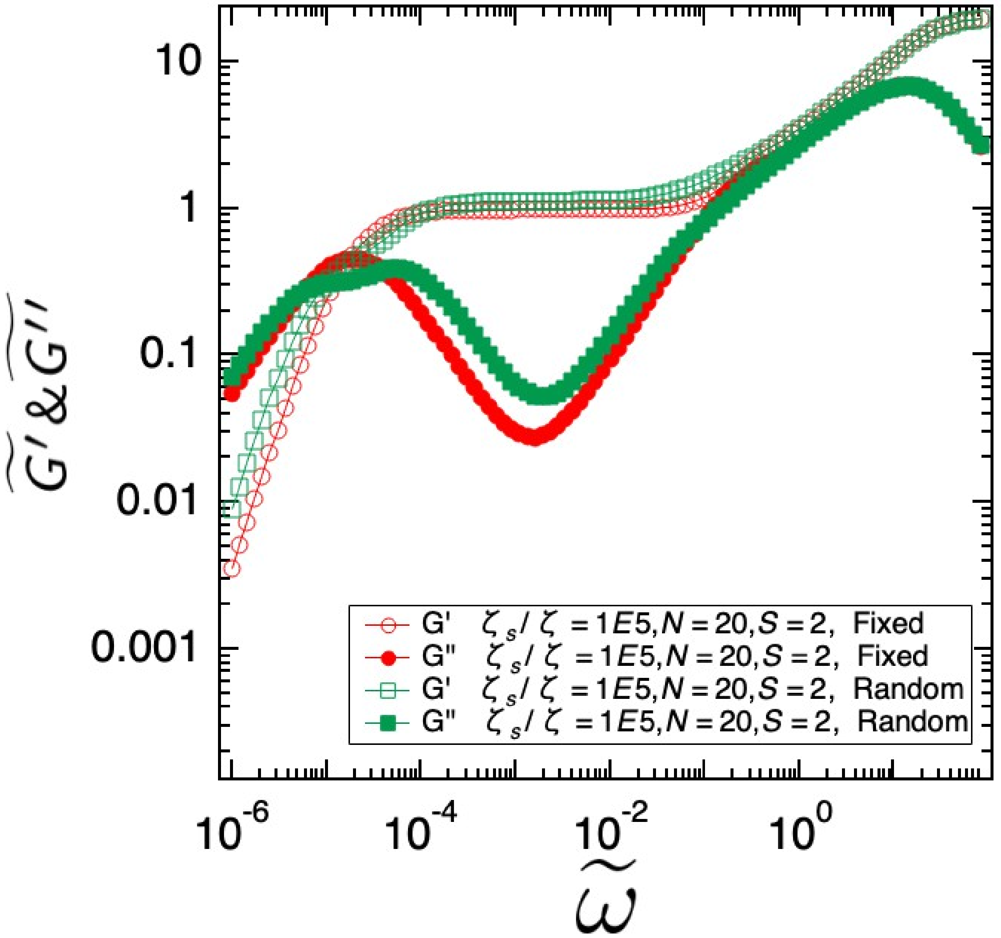

Figure 2.15: Comparisons of linear viscoelastic master curves for different distribution of stickers. -

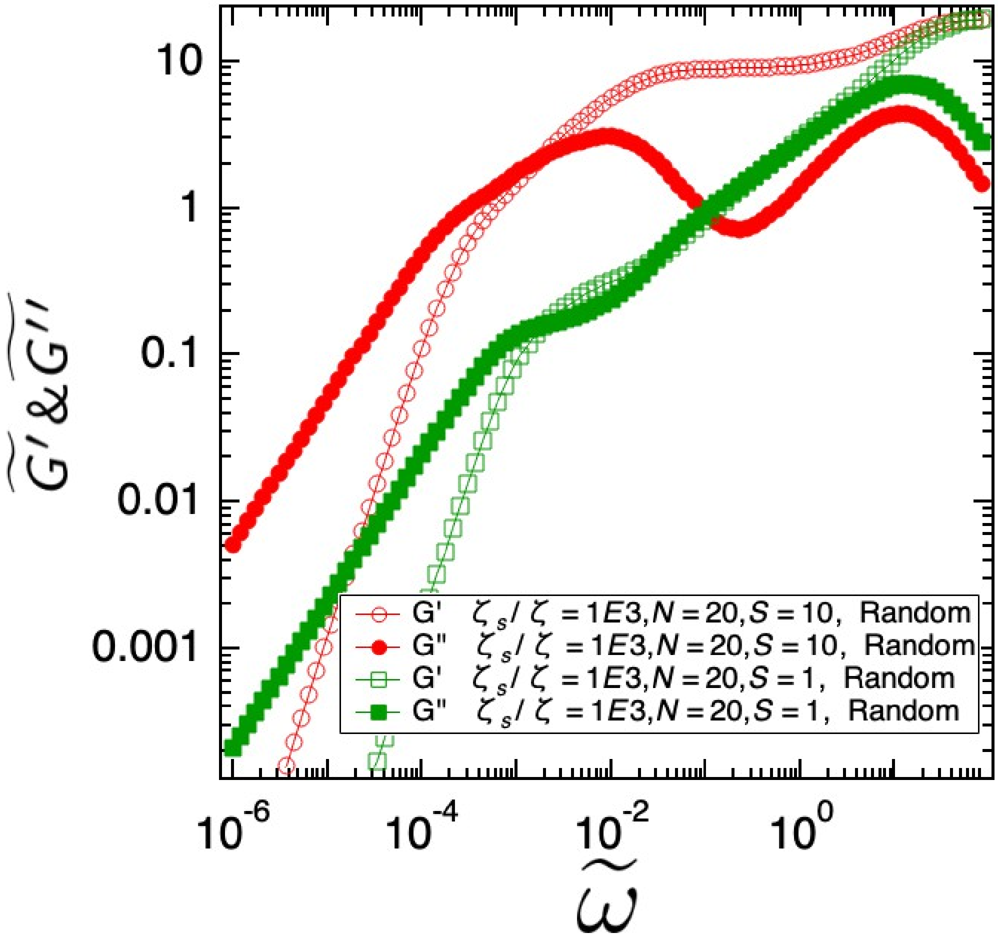

Figure 2.16: Comparisons of linear viscoelastic master curves for different number of stickers S. -

Figure 2.17 shows the effects of the friction ratio. The physical meaning of the friction ratio is the lifetime of stickers, which is related to the bonding energy. The higher the bonding energy is, the larger the friction ratio is. The window of the prediction of the chain with longer lifetime of stickers (larger friction ratio) is wider than that of the chain with shorter lifetime of stickers at the intermediate frequencies. Moreover, it displays a more remarkable time delay at the low frequencies. However, there is almost no difference at the high frequencies, which indicates that the lifetime of stickers has no effects on the local dynamics of chains.

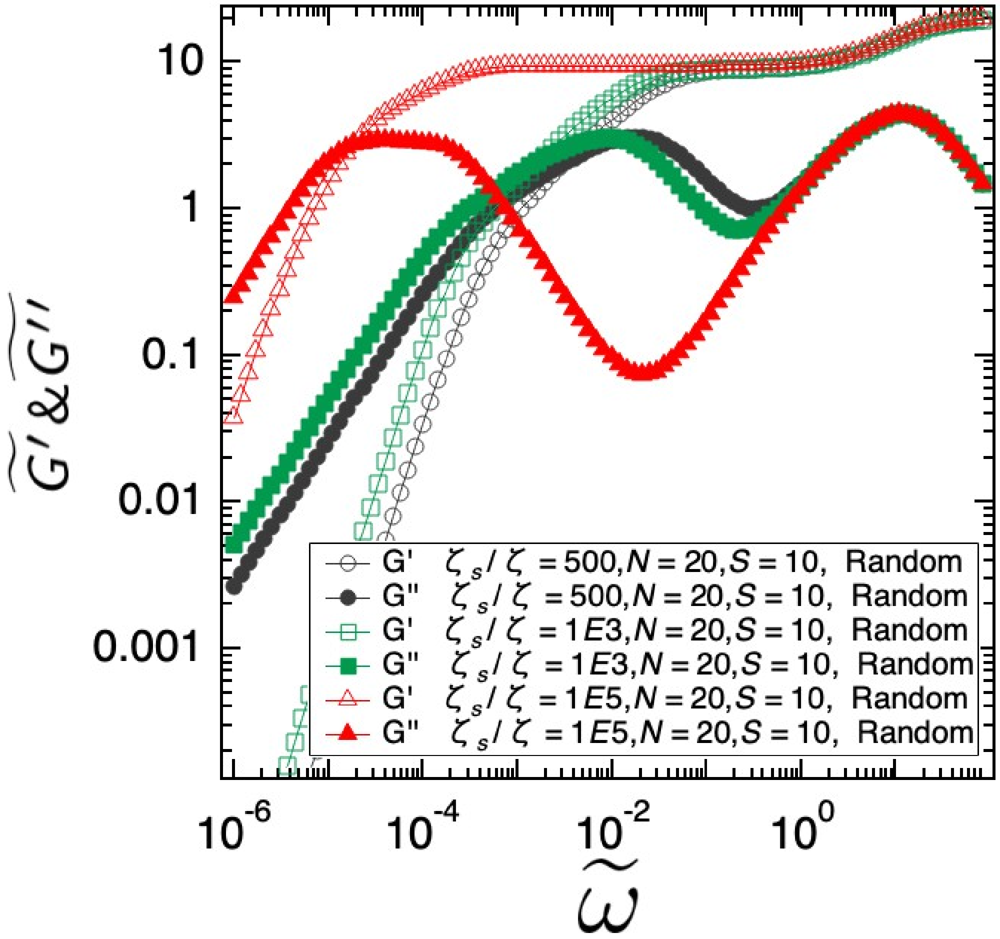

Figure 2.17: Comparisons of linear viscoelastic master curves for different friction ratio ζ_s/ζ. -

Figure 2.18 displays the comparisons with the predictions of the sticky Rouse model reported by Chen et al. [22]. Their model is simple and is capable of capturing the main features of the viscoelastic response of reversible polymer networks. From Figure 2.18, we can see that Chens formula is reasonably consistent with our simulations. However, discrepancies appear in the low and intermediate frequencies. It probably results from the ignoring of the dangling effect and the unknown distribution of stickers in their model.

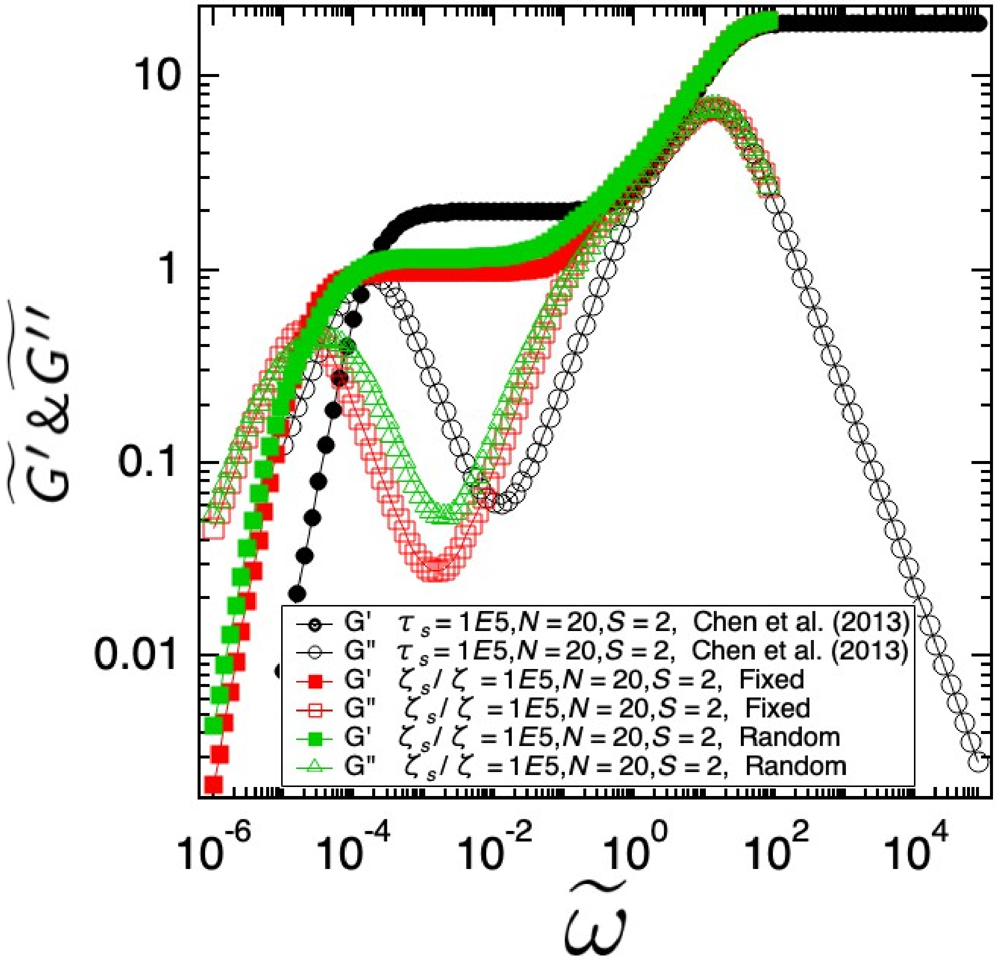

Figure 2.18: Comparisons of linear viscoelastic master curves between Chen et al. (2013)[22] and our simulation predictions. -

2.5 Conclusions

The dynamics response as well as the topological structure of reversible polymer networks are studied through a multi-chain model in this Chapter. This model not only is able to describe the topological structures of polymer networks, but also is capable of predicting rheological behavior in a more comprehensive way.

The simulation results show that the number of stickers decides the level of the second plateau of $G(t)$ as well as of the plateau of $G'(\omega)$ at the intermediate frequencies. In addition, the number of stickers not only affects the local dynamics of polymer networks but also has an effect on the viscoelastic response of polymer networks at a whole scale. Nevertheless, the lifetime of stickers (friction ratio) merely affects the relaxation of the polymer networks at a whole scale rather than locally.

Moreover, the distribution of stickers affects the viscoelastic response of associating polymers. Chen et al.[22] reported a classic sticky Rouse model, which is explicit and simple. However, their model did not take the distribution of stickers into account. Indeed, discrepancies of the linear viscoelastic response typically appear at the intermediate frequencies. We will discuss this problem as well in the next Chapter.

Even though the multi-chain model seems perfect, it is somewhat time-consuming. For instance, to plot the Figure 2.13, it takes 3-4 days, considering the fact that we still can not obtain good results of the terminal relaxation. In the next Chapter, we propose a single-chain model, which makes the running time shorter without deteriorating the reliability.

3

A Single-chain Model for the Linear Viscoelasticity of Unentangled Associating Polymer Melts

3.1 Introduction

Our current understanding of the rheology of associating polymers is based on the seminal paper of Green and Tobolsky [40], who first introduced the concept of impermanent network. Associating polymers indeed form impermanent networks with temporary cross-links made up of sticky monomers along the chains. The dynamics of associating polymers then becomes a many-chain problem, even in the case of low-molar mass unentangled polymers. Successful single-chain models for unentangled associating polymers have been first developed by Baxandall [11], Rubinstein and Semenov [107], and Leibler [73], with their well-known sticky Rouse model, later refined by several authors, e.g., by Indei and Takimoto [58] who accounted for the occurrence of multiple stickers in the same network junction.

A systematic comparison of the predictions of the sticky-Rouse model with data on unentangled associating polymers has been made only more recently. In particular, we here refer to the nice contributions by Chen et al. [22], Shabbir et al. [117], and Cui et al. [27], who clearly show that, though the sticky Rouse model qualitatively describes the linear viscoelastic (LVE) behavior of a variety of associating systems, a quantitative agreement with data is still missing. Discrepancies typically emerge in the intermediate frequency range of the LVE response, i.e., in the region where data exhibit a rubbery plateau in the elastic modulus, and a minimum in the loss modulus. Particularly critical is the minimum, which models often predict more pronounced than shown by the data.

A possible reason for the mismatch is that in the sticky-Rouse model the sticky beads are assumed to be evenly distributed along the chain, while the real chains are copolymers with a random distribution of sticky comonomers along the chain. The model of Jiang et al. [61] accounts for the randomness of the sticker location along the chain by solving a Rouse-like mathematics with beads endowed with two different friction coefficients, a small one for the ordinary non-sticky beads, and a large one for the stickers. As we shall see, however, this model remains somehow inadequate. Indeed, the same authors have just published a paper [62], where they perform molecular dynamics simulations of Kremer-Grest-type unentangled associating chains, and compare the resulting relaxation modulus $G(t)$ with that predicted by their model in [61]. One may note that the comparison remains not completely successful at intermediate times, corresponding to the $G'(\omega)$ plateau region. In this paper, we suggest a solution for this discrepancy.

The paper is organized as follows. We first develop the Rouse-like mathematics of a chain with the same friction coefficient at all beads, but different chain contour lengths between consecutive beads. This model is meant to describe the slow relaxation of the associated chains, the beads coinciding with the stickers, randomly distributed along the chain. The theory is then completed by suggesting a more complete description of the fast relaxation process. Next, the model is successfully compared with two different sets of data provided by Lewis et al. [74], and by Cui et al. [27]. Final remarks conclude the paper.

3.2 Theory

Let's consider unentangled polymer chains with N Kuhn segments and S sticky points forming binary junctions. If those junctions are long lasting, the system becomes an impermanent network that completely relaxes only at times longer than the lifetime of those junctions. At sufficiently long times, the many-chain dynamics of the network can be replaced by that of a single chain where the sticky points are endowed with a sufficiently large (fictitious) friction coefficient, as suggested long ago by several authors [11, 58, 73, 107]. As mentioned in the Introduction, we here consider a random distribution, which is the actual situation of the data by Lewis et al. [74] and by Cui et al. [27] .

Should two of the sticky points be located at the chain ends, and all other ones distributed uniformly, as in the work of Chen et al. [22], the number of Kuhn segments in each chain strand is $N/(S-1)$. In that case, the chain is a classic Rouse chain with an elastic constant given by

$$k = \frac{3k_BT}{\frac{N}{S-1}b^2}, \tag{3.1}$$

where k_BT is thermal energy, and b the Kuhn segment length. In the case of a random distribution, for any given location of the S sticky points, the i-th strand will have an elastic constant $k_i = \alpha_i k$, with the α_i's given by

$$\alpha_i = \frac{\frac{N}{S-1}}{n_i}, \tag{3.2}$$

n_i being the number of Kuhn segments in the i-th strand. The α_i numbers are on average larger than unity because the utmost sticky points are generally not located at the chain ends.

The long-time chain dynamics then obeys the following Langevin equations

$$\begin{cases} \zeta\frac{\mathrm{d}\mathbf{R}_1}{\mathrm{d}t} = \alpha_1 k(\mathbf{R}_2 - \mathbf{R}_1) + \mathbf{f}_1, \text{if } i = 1 \\ \zeta\frac{\mathrm{d}\mathbf{R}_i}{\mathrm{d}t} = k[\alpha_i(\mathbf{R}_{i+1} - \mathbf{R}_i) - \alpha_{i-1}(\mathbf{R}_i - \mathbf{R}_{i-1})] + \mathbf{f}_i, \\ \quad \text{if } i = 2, ..., S-1 \\ \zeta\frac{\mathrm{d}\mathbf{R}_S}{\mathrm{d}t} = \alpha_{S-1} k(\mathbf{R}_{S-1} - \mathbf{R}_S) + \mathbf{f}_S, \text{if } i = S \end{cases} \tag{3.3}$$

where $\mathbf{R}_i$ is the position of the i-th sticky point, ζ is their equivalent friction, and $\mathbf{f}_i$'s are the random forces obeying the fluctuation dissipation theorem characterized by

$$\begin{aligned} &\langle \mathbf{f}_n(t)\rangle = 0, \\ &\langle f_{n\alpha}(t) f_{m\beta}(t')\rangle = 2\zeta k_BT\delta_{nm}\delta_{\alpha\beta}\delta(t-t'). \end{aligned} \tag{3.4}$$

As is usual [84], to solve the set of eqs (3.3), we need to find the normal modes, i.e., the S eigenvalues λ_i of the symmetric matrix

$$\begin{bmatrix}
\alpha_1 & -\alpha_1 & 0 & \cdots & \cdots & \cdots & \cdots & \cdots & 0 \\
-\alpha_1 & \alpha_1+\alpha_2 & -\alpha_2 & 0 & \cdots & \cdots & \cdots & \cdots & 0 \\
0 & \cdots & \cdots & \cdots & \cdots & \cdots & \cdots & \cdots & 0 \\
\vdots & \vdots & \vdots & \vdots & \vdots & \vdots & \vdots & \vdots & \vdots \\
0 & \cdots & 0 & -\alpha_{i-1} & \alpha_{i-1}+\alpha_i & -\alpha_i & 0 & \cdots & 0 \\
\vdots & \vdots & \vdots & \vdots & \vdots & \vdots & \vdots & \vdots & \vdots \\
0 & \cdots & \cdots & \cdots & \cdots & \cdots & \cdots & \cdots & 0 \\
0 & \cdots & \cdots & \cdots & \cdots & 0 & -\alpha_{S-2} & \alpha_{S-2}+\alpha_{S-1} & -\alpha_{S-1} \\
0 & \cdots & \cdots & \cdots & \cdots & \cdots & 0 & -\alpha_{S-1} & \alpha_{S-1}
\end{bmatrix} \tag{3.5}$$

which reduces to the Rouse matrix if all elastic coefficients α_i are equal to unity. Also in this case, one of the eigenvalues is zero. The $S-1$ modes $\mathbf{X}_p$ corresponding to the nonzero eigenvalues obey the equation

$$\zeta_p \frac{\mathrm{d}\mathbf{X}_p}{\mathrm{d}t} = -k_p \mathbf{X}_p + \mathbf{f}_p \tag{3.6}$$

where the ratio $\frac{\zeta_p}{k_p}$ defines the relaxation time τ_p of the p-th mode:

$$\tau_p = \frac{\zeta_p}{k_p} = \frac{\zeta}{\lambda_p k} = \frac{\frac{N}{S-1} b^2}{\lambda_p 3 k_B T} \zeta \tag{3.7}$$

The long-time stress relaxation is then given by

$$G_{long}(t) = \nu k_B T \sum_{p=1}^{s-1} \exp\left(-\frac{t}{\tau_p}\right) \tag{3.8}$$

where ν is chain number density.

In order to determine the short-time dynamics (aside from the glassy one), we argue as follows. We have seen that the sticky points, with their friction coefficient ζ, determine the long-lasting topology of the network. However, the binary junctions they form are not virtually fixed in space at short times as the large friction coefficient ζ might suggest. Indeed, the binary junctions fluctuate in space, their local motion being controlled by a friction coefficient ζ_{strand} comparable to that of a network strand between consecutive stickers, which on average is lower than

$$\zeta_{strand} = \frac{N}{S-1} \zeta_K, \tag{3.9}$$

where ζ_K is the Kuhn segment friction coefficient. Within the assumption that the network junctions are long lasting, it is

$$\zeta \gg \zeta_{strand}. \tag{3.10}$$

Consistently with the argument above, the short time dynamics generates a stress relaxation given by:

$$G_{short}(t) = \nu k_B T \sum_{p=1}^{N} \exp\left(-\frac{t}{\tau_{R,p}}\right), \quad \tau_{R,p} = \frac{1}{p^2}\tau_{Rouse}, \quad \tau_{Rouse} = \frac{\zeta_K N^2 b^2}{6\pi^2 k_B T}. \tag{3.11}$$

As in the classical theory [22], the overall stress relaxation is then given by:

$$G(t) = G_{short}(t) + G_{long}(t). \tag{3.12}$$

Notice, however, that in the classical theory [22] the short-time relaxation is written as

$$G_{short}(t) = \nu k_B T \sum_{p=S}^{N} \exp\left(-\frac{t}{\tau_{R,p}}\right) \tag{3.13}$$

i.e., the sum over the Rouse normal modes starts from $p = S$ rather than from $p = 1$, as in eq (3.11). In other words, the classical theory assumes that at short times the first $S - 1$ normal modes are frozen, i.e., that the junctions created by the sticky points are virtually fixed in space because of their large friction coefficient ζ, whereas in reality their local mobility is assured by the small value of the friction coefficient ζ_{strand}. We will show in the following section how important is the difference between eq (3.11) and the classical assumption.

Nondimensional parameters of the model are: the number N of Kuhn segments, the number S of the sticky points, as well as their location along the chain, ranging in the interval $\{1, \cdots, N\}$. The dimensional parameters are the friction coefficient ζ_K of the Kuhn segments, the much larger (effective) friction coefficient ζ of the sticky points, and $\nu k_B T$, where ν is chain number density.

3.3 Results and Discussion

We first examine the data reported by Lewis et al. [74] referring to poly-butyl acrylate (PBA) melts with an average molar mass M_w of the order of 80 kg/mol, and a polydispersity index PI of the order of 2.5. The melts are essentially unentangled since the PBA entanglement molar mass is $M_e \approx 20kg/mol$ [121]. This is also confirmed by Figure 3.1, showing the Rouse-like linear viscoelastic response of the basic PBA melt at room temperature. Notice that the glassy response is absent in Figure 3.1 because the glass temperature is much lower than 25°C, and the highest frequency explored is not large enough.

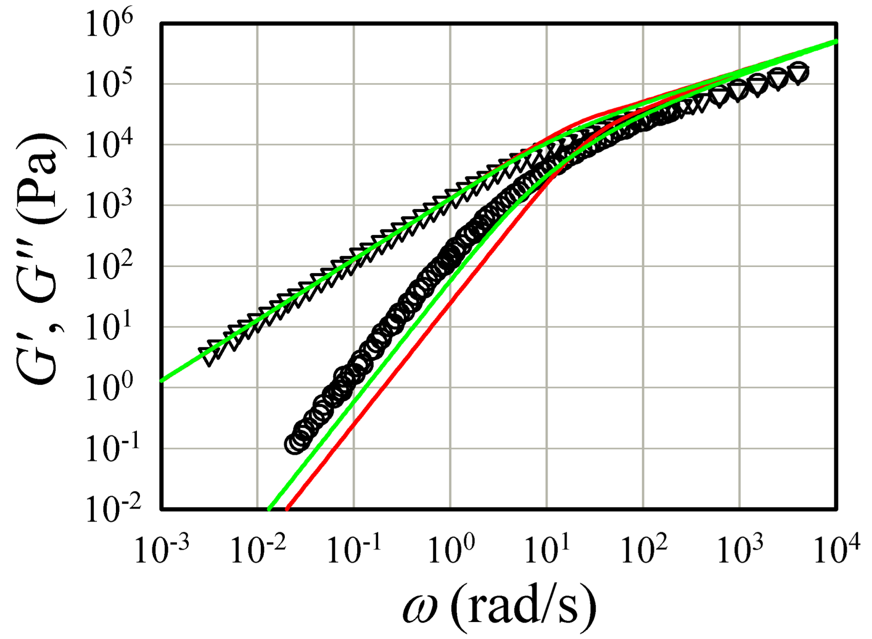

Figure 3.1: Frequency response of the PBA melt ($M_w = 82kg/mol$, PI=2.5) at 25°C. - Symbols are data by Lewis et al. [74]. Red and green lines are predictions of the monodisperse ($M = M_w$) and polydisperse Rouse model, respectively

Figure 3.1 shows both the monodisperse and polydisperse Rouse model predictions. Knowing that for PBA melts at room temperature the Kuhn segment molar mass is $M_K \approx 0.7kg/mol$ and the mass density is $\rho \approx 10^3 kg/m^3$ [121], the monodisperse prediction is obtained from eq (3.11) with $N = M_w/M_K \approx 100$ (results in Figure 3.1 are in fact insensitive to N provided N is larger than ca. 50), and by choosing the Kuhn segment friction coefficient ζ_K so as to fit the zero shear viscosity given by G''/ω in the terminal region. The polydisperse prediction is obtained by assuming a Generalized Exponential (GEX) distribution function [93]. We have taken the exponent within the exponential equal to 2, a value often suggested in the literature [128], while the other two parameters are determined from the average molar mass ($M_w = 82kg/mol$) and the polydispersity index (PI=2.5). In the low-M tail of the molar mass distribution the number of Kuhn segments can be small enough to require that $\tau_{R,p}$ and τ_{Rouse} of eq (3.11) take the more complex expressions reported in the literature (see e.g. Likhtman [76]).

Figure 3.1 shows good agreement between data and polydisperse predictions. The minor discrepancy at high frequencies, while suggesting a smaller value for the Kuhn segment friction coefficient, reveals a minor influence of topological effects, i.e., the presence of some entanglements. In other words, should ζ_K be reduced to fit the high frequency data, the Rouse-like prediction in the terminal region falls slightly to the right of the data, thus indicating a somewhat slower terminal relaxation because of topological interactions.

We next examine the data of Lewis et al. [74] for the polymers containing sticky points, obtained by copolymerization n-butyl acrylate with comonomers bearing hydrogen-bonding side groups. We here only consider PBA melts with the UPy comonomer because they show a plateau in $G'(\omega)$, which is typical of an impermanent network with long-lasting sticky junctions.

Figure 3.2 reports the comparison of the model predictions with the data on PBA melts with a 5% concentration of UPy comonomers. We first examine the case with no stickers by using the polydisperse Rouse model (cyan curves). We so determine the Kuhn segment friction coefficient by fitting the high frequency response. Although the G' curve follows the data, the G'' one drops down too early, probably because we are omitting some contribution from the glassy response. Alternatively, we might obtain a better fit by artificially decreasing the Kuhn segment molar mass M_K, but there is no evidence thatM_K is significantly smaller than $0.7kg/mol$.

Next, we consider predictions of the polydisperse model with an average number of stickers per chain equal to 11 (corresponding to 5% UPy molar concentration). The green curves are obtained by fitting the low frequency region through the arbitrary choice of the friction coefficient ζ of the sticky points. As is apparent, the plateau modulus is somewhat lower than that shown by the data. We believe that such discrepancy is due to the fact that the model has so far ignored the possible presence of trapped entanglements. Indeed, the large value of M_w, significantly larger than M_e, together with the evidence of some topological interaction in the basic polymer (see

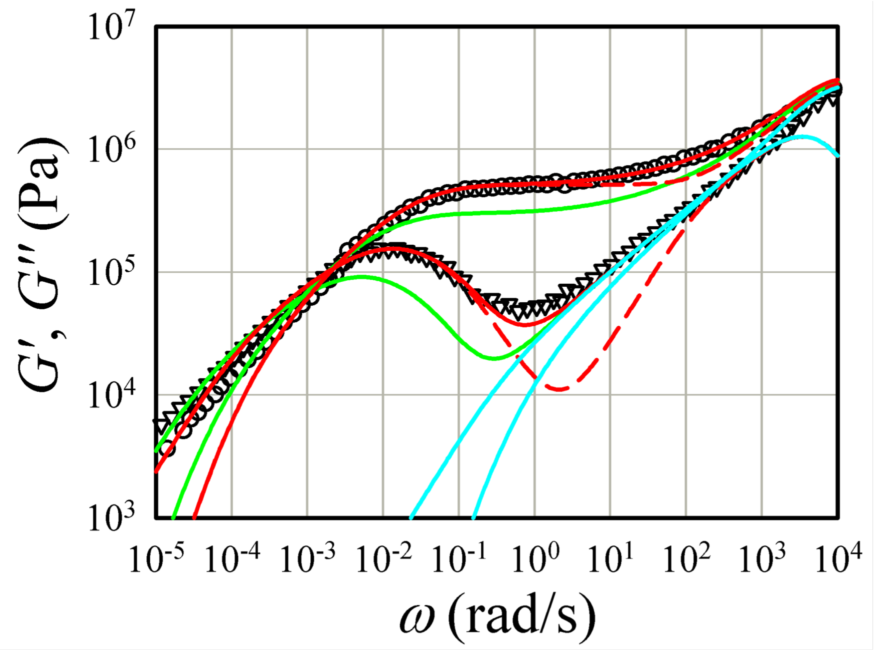

Figure 3.2: Frequency response at 25°C of the PBA melt ($M_w = 75kg/mol$, PI=2.4) with 5% molar concentration of UPy monomers (a mean of 11 stickers per chain). - Symbols are data by Lewis et al. (2014)[74]. Cyan and green lines are polydisperse model predictions for the case of no stickers and 5% stickers, respectively. Red lines are predictions accounting for trapped entanglements, using eq (3.11) (full lines) or eq (3.13) (dashed lines) for G_{short}

discussion of Figure 3.1), indicate that when the stickers close up to form junctions the impermanent network entraps a non-negligible number of entanglements. The solid red curves in Figure 3.2 are obtained by raising the long-time modulus $G_{long}(t)$ in eq (3.8) by a factor of 1.7. This would indicate that there is somewhat less than one trapped entanglement per every network strand, a result compatible with the ratio M_w/M_e. Fit of the low frequency data indicates that the friction coefficient ζ of the sticky points is about $3.5 \cdot 10^4$ times that of the Kuhn segment, ζ_K.

The low frequency data also indicate that the terminal region is not yet reached, i.e., that some more permanent weak structure is still present. Such long-living structures probably result from stronger junctions created by sticker doublets. The latter occur when two stickers are located at two neighboring beads. The numerical code reveals that the probability of such occurrence is about 1%, which seems in agreement with the fact that on average there are ca. 10 stickers per chain, the latter containing (on average) ca. 100 beads. The junctions formed by doublets are expected to be more permanent than junctions formed by individual stickers [27, 107].

It is now important to notice that the dashed red curves in Figure 3.2 are obtained by using eq (3.13) instead of eq (3.11). It is remarkable how well the solid red lines, differently from the dashed ones, fit the G'' minimum of the data. How difficult is the matching of this minimum has been the subject of several discussions in the literature [22, 27]. It so appears that the solution of this difficulty is in the fact that the sticky junctions move in space (and dissipate energy) with a friction coefficient close to ζ_K (actually ζ_{strand}), rather than with the equivalent friction coefficient ζ of the network topology. The latter is the assumption tacitly made in the existing literature. It is finally noted that also the G' solid red curve fits the data better than the dashed one in the intermediate frequency range.

Figure 3 reports the comparison of the model predictions with the data of the PBA melt having a 2% molar concentration of UPy comonomers. In this case the LVE data reported by Lewis et al. are $G'(\omega)$ and the complex viscosity $\eta^*(\omega)$. The triangles in Figure 3.3, representing $G''(\omega)$, were then obtained indirectly by using the relationship $\eta^* = \sqrt{(G'^2 + G''^2)}/\omega$. The scatter of the triangles in the intermediate frequency region is due to the fact that G' is dominating in that region.

Here, as in the previous case, the long-time modulus $G_{long}(t)$ has been increased by the same factor 1.7 because of trapped entanglements. As regards friction coefficients,

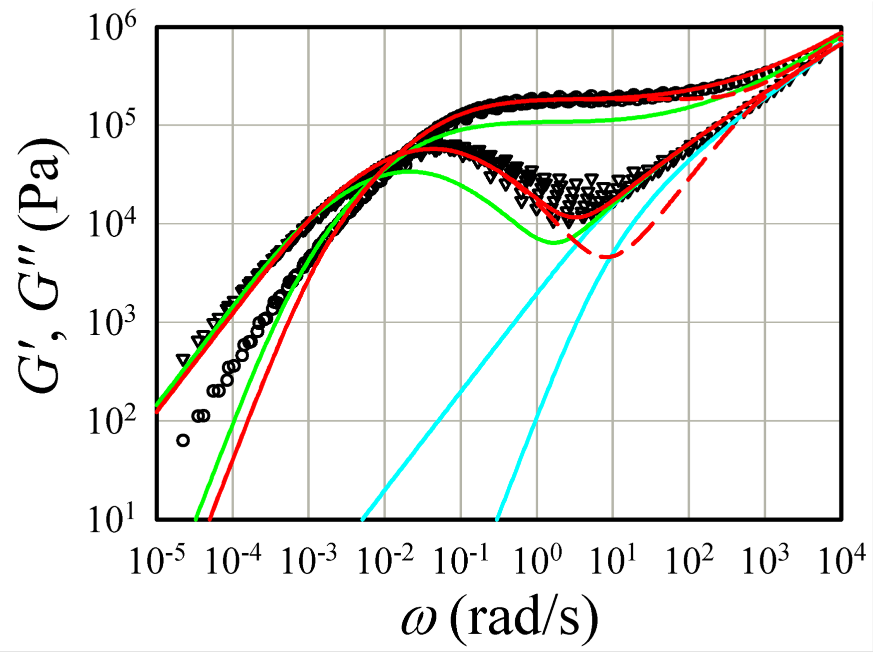

Figure 3.3: Frequency response at 25°C of the PBA melt ($M_w = 82kg/mol$, PI=2.5) with 2% molar concentration of UPy monomers (a mean of 5 stickers per chain) . - Symbols are data by Lewis et al. [74]. Lines as in Figure 3.2.

we find that ζ_K is smaller than that of the 5% case by a factor of ca. 20 due to the different distance from the glass temperature T_g. Also the sticker friction coefficient ζ comes out smaller (by a factor of ca. 8) in spite of the fact that the binding energy is independent of T_g. Decrease of ζ is probably due to the larger mobility of the network strands.

Before leaving the analysis of the data by Lewis et al. [74] it is worth considering that, as previously mentioned, the ratio ζ/ζ_K for the UPy comonomers is larger than 10^4, which guarantees the appearance of a plateau modulus. The absence of a plateau in G' curves of the other comonomers examined by Lewis et al[74]. indicates that such friction ratio is not large enough. Quantitative analysis of those other data falls beyond the scope of the present work.

We now move on to examine the LVE data of Cui et al. [27] where the same sticky monomer, UPy, is co-polymerized with ethylhexyl acrylate (EHA) monomers. Two features distinguish these more recent data with respect to those of Lewis et al[74]. One of them is that one of the copolymers only contains two stickers per chain (on average), a feature that, as shown in the following, is of particular importance. The second difference is that the copolymer chains are made up of very few Kuhn segments and are therefore definitely unentangled. For the same reason, however, the glassy response plays a major role.

Figure 3.4 reports Cui et al. [27] G', G'' data at 70°C for the nearly monodisperse PEHA melt (without stickers) with $M_w = 18kg/mol$. Since $M_e \approx 15kg/mol$ [27], this melt can certainly be considered unentangled. The crossing of the data at high frequencies is a signature of the glassy response. Hence, in order to obtain predictions in the low frequency range, we first made a fit of the high frequency data (from $\omega = 10^7 rad/s$ onwards) with a multi-mode Maxwell model. The resulting discrete glassy spectrum is shown in Table 1. From the spectrum, we calculate the glassy contribution to the zero-shear viscosity given by $\eta_G \approx 0.1 Pa \cdot s$.

In the lower frequency range, predictions are based on the Rouse model with parameters determined as follows. As indicated by Cui et al. [27], the PEHA Kuhn segment is made up of 13 monomers, corresponding to a Kuhn segment molar mass $M_K \approx 2.4kg/mol$. Hence, we used eq (3.11) with $N = M_w/M_K = 18/2.4 \approx 7$. As regards density, lacking direct information, we used $\rho = 900kg/m^3$. We then chose the Kuhn segment friction coefficient ζ_K so as to fit the zero-shear viscosity (given by

Table 3.1: Discrete glassy spectrum for PEHA at 70°C

Relaxation times (s)	Moduli (Pa)
$4.2 \cdot 10^{-15}$	$1.3 \cdot 10^{8}$
$2.2 \cdot 10^{-14}$	$9.8 \cdot 10^{7}$
$9.6 \cdot 10^{-14}$	$1.1 \cdot 10^{8}$
$5.5 \cdot 10^{-13}$	$1.3 \cdot 10^{8}$
$3.3 \cdot 10^{-12}$	$1.2 \cdot 10^{8}$
$1.7 \cdot 10^{-11}$	$8.3 \cdot 10^{7}$
$8.9 \cdot 10^{-11}$	$5.9 \cdot 10^{7}$
$5.0 \cdot 10^{-10}$	$2.9 \cdot 10^{7}$
$2.8 \cdot 10^{-9}$	$1.0 \cdot 10^{7}$
$1.6 \cdot 10^{-8}$	$2.9 \cdot 10^{6}$
$1.3 \cdot 10^{-7}$	$1.3 \cdot 10^{5}$

G''/ω in the terminal region), accounting for the fact the glassy contribution is known (see above). Lines in Figure 3.4 were then obtained by summing the glassy and Rouse contributions. Agreement between predictions and data can be deemed satisfactory.

Figure 3.5 reports the data for the copolymer with 2 UPy stickers per chain. As is apparent, notwithstanding the strength of the UPy association, there is no G' plateau. The reason is actually quite simple. Molecules associate to form impermanent longer chains, thus saturating the 2 stickers they contain. Indeed, no temporary network can form unless stickers are at least 3 per chain. The long impermanent chains thus formed relax at a rate controlled by the ordinary Kuhn segment friction coefficient, essentially ignoring the presence of stickers except when their dissociation destroys the long impermanent chains. The equilibrium length of these associated chains is in fact determined by the detachment time of the stickers, insofar as no associated long chain can exist whose Rouse-like relaxation time is longer than the junction lifetime of the stickers.

The peculiar behavior of chain with only 2 stickers has been missed by Cui et al. [27] who used either the classic sticky-Rouse theory or a more sophisticated stochastic model, both predicting a G' plateau. One may note that the essential irrelevance of the sticker friction coefficient ζ in this case of only 2 stickers per chain is the same one previously mentioned when considering the local motion of the network junctions,

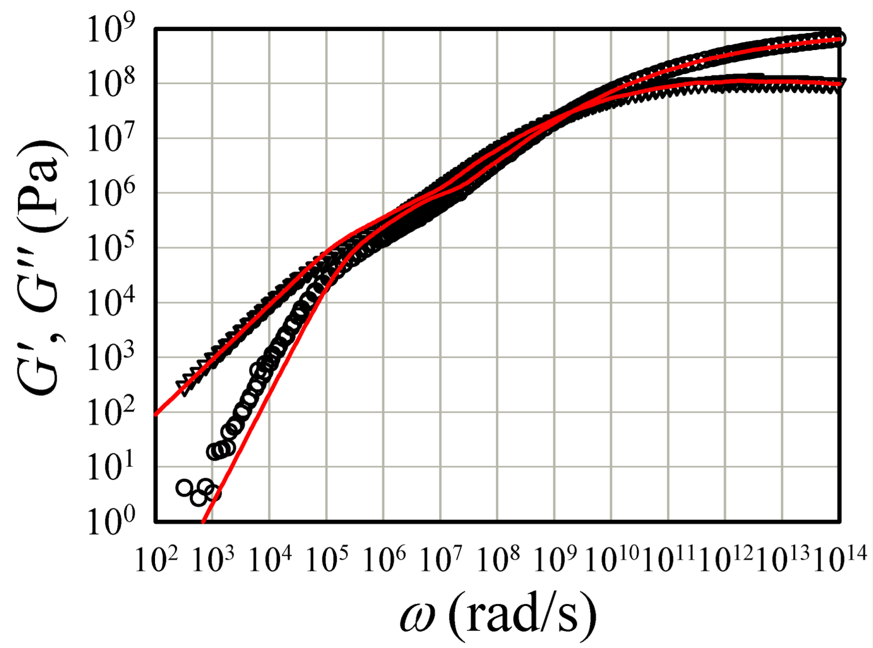

Figure 3.4: Frequency response at 170°C **of the PEHA melt** ($M_w = 18kg/mol$, **PI=1.05) without stickers.** - Symbols are data by Cui et al. (2018)[27]. Lines are Rouse predictions, summed up to the glassy contribution.

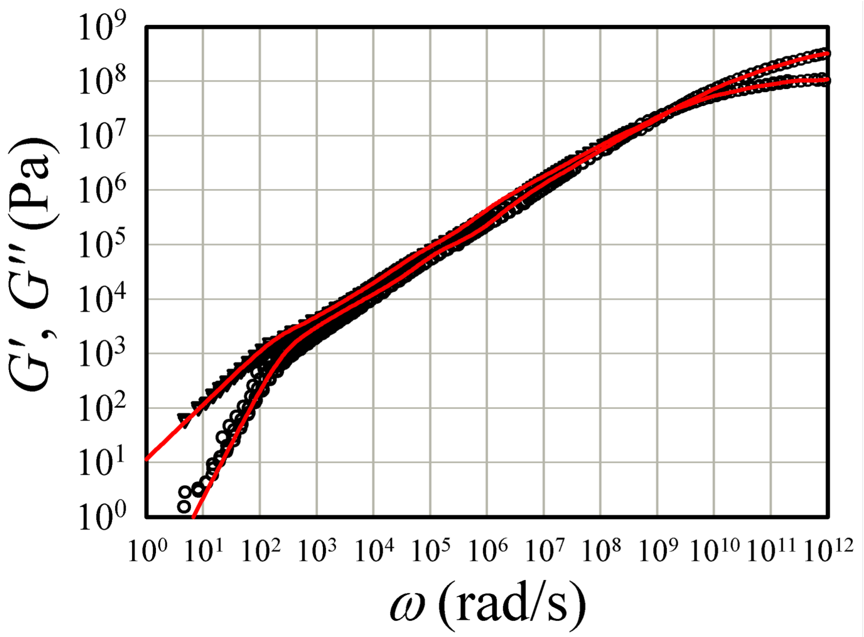

Figure 3.5: Frequency response at 170°C of the PEHA melt with 2 stickers per chain ($M_w = 21kg/mol$, PI=1.24). - Symbols are data by Cui et al. (2018)[27]. Lines are polydisperse Rouse predictions with parameters specified in the text (plus the glassy contribution)

leading to the use of eq (3.11) instead of eq (3.13).

Predictions in Figure 3.5 were obtained by using a model for the long-associated Rouse chains with a molar mass $M_w \approx 1200kg/mol$, corresponding to nearly 60 unassociated chains. Best fit of the data was achieved for a value of the Kuhn segment molar mass $M_K \approx 4.8kg/mol$ (giving $N = M_w/M_K \approx 250$). One may note that M_K of the associated chain is ca. twice as large than that of the unassociated one. This is probably due to the short branches of the associated chain arising from the fact that the sticky points are generally not located at the ends of the unassociated chains. The other parameter of the best fit is the Kuhn segment characteristic time, which we find essentially equal to that of the unassociated polymer. Needless to say, curves in Figure 3.5 also account for the glassy contribution, which the data indicate to be the same as the PEHA melt, i.e., that reported in Table 3.1.

The above analysis of the data in Figure 3.5 delivers a very important result. Indeed, as just discussed, the value of the Rouse time of the associated long chain (equal to ca. $3 \cdot 10^{-3}s$) also represents the lifetime of the UPy sticker junction. Such a lifetime is confirmed by the value of the frequency at which the terminal relaxation starts (ca. $300rad/s$), and it will be used in dealing with the other associating polymers, carrying more than 2 stickers per chain.

Figure 3.6 reports the data of Cui et al. [27] for the PEHA melt with 7 UPy comonomers per chain (on average) showing, as expected, a clear G' plateau. The analysis starts by first simply that the lifetime of the junctions is $3 \cdot 10^{-3}s$, as derived from Figure 3.5. Such assumption leads to the cyan curves in Figure 3.6, clearly inadequate. The data strongly indicate a much longer lifetime of the stickers as well as a slightly smaller value of the plateau modulus. The first discrepancy is due to an effect emphasized by Rubinstein and Semenov [107] who write (in the Introduction) a network strand breaks and recombines again many times at the same pair of stickers before a final break occurs . It is therefore no surprise that fitting of the data requires a much longer sticker lifetime in the network with respect to that in the linear chain considered in Figure 3.5.

As regards the second (minor) discrepancy, i.e., the slightly lower level of the plateau modulus, it is worth noting that the 7 UPy stickers will distribute in a chain made up of very few Kuhn segments (at most $N = M_w/M_K = 30/2.4 \approx 13$). Consequently, we expect that some Kuhn segments will contain more than one sticker, whereas the cyan curves in Figure 3.6 are calculated by assuming that the 7 stickers are all located on different Kuhn segments. The occurrence of multiple stickers on the same Kuhn segment reduces the number of elastically active network strands, and hence the level of the plateau modulus. To confirm this effect, simulations found that, on average, only ca. 2 Kuhn segments (out of 13) contain single stickers, while the other 5 stickers form clusters located on other Kuhn segments. Such clusters form in spite of the fact that the code randomly distributes the 7 stickers among the 13 Kuhn segments. To be complete, we mention that in fact, since the sample is polydisperse, numbers of stickers and of Kuhn segments are made proportional to the molar mass of each component of the molar mass distribution, 7 stickers and 13 Kuhn segments being average values.

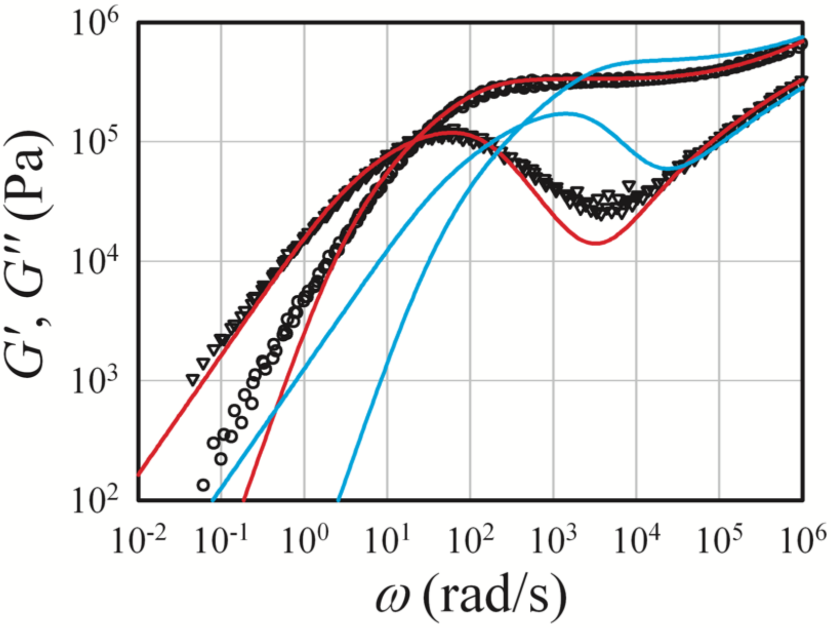

Figure 3.6: Frequency response at 170°C of the PEHA melt with 7 stickers per chain ($M_w = 30kg/mol$, PI=1.38). - Symbols are data by Cui et al. [27]. Lines are polydisperse Rouse predictions with parameters specified in the text.

Consistently with the above discussion, the red curves in Figure 3.6 were then obtained by reducing the average number of effective stickers per chain from 7 to 5.3, and by increasing the effective sticker lifetime from $3 \cdot 10^{-3}s$ to $5.4 \cdot 10^{-2}s$. We also slightly increased the Kuhn segment characteristic time from $1.6 \cdot 10^{-6}s$ to $2.4 \cdot 10^{-6}s$ to optimize the fit in the high frequency range. The lifetime ratio $5.4 \cdot 10^{-2}/(3 \cdot 10^{-3}) = 18$ indicates that on average the stickers open up and close up again 18 times before finding a different partner, i.e., before contributing to the relaxation process. The intuition of Rubinstein and Semenov [107] appears confirmed.

Although the agreement of the red curves with data is satisfactory, some minor discrepancies can be observed. Indeed, data do not show the expected terminal behavior, thus indicating the presence of a small proportion of long-lasting structures. These can be rationalized on the basis of the clusters of stickers previously mentioned. It appears sensible to envisage that such clusters may form more long-lasting temporary junctions.

An analysis similar to that just made for the 7 sticker case could be repeated for the two higher UPy concentrations reported by Cui et al. [27], with 11 and 17 stickers per chain, respectively. Although the qualitative aspect of the data looks similar, the large number of stickers distributed over so few Kuhn segments makes a quantitative analysis awkward, also because an arbitrary choice of more parameters would be required.

3.4 Conclusions

The main original contributions of this work are as follows:

a) The analysis of the data in Figure 3.5 for a melt of unentangled associating polymers with only two stickers per chain has clearly shown for the first time that the classic sticky-Rouse recipes, predicting a G' plateau not shown by the data, fail because the association generates longer chains but no network structure.

b) The same analysis also provides an estimate of the true lifetime of the sticky junction, coinciding with the longest relaxation time of the associated chain. Indeed, when in this case sticky junctions open up, the chance that the same two stickers recombine is expected not to be significantly different from that of combining with a different partner.

c) Still, the success of the Rouse-like model used for the data in Figure 3.5 clarifies that the friction coefficient of the sticky junctions in their 3D motion is not significantly different from that of the ordinary monomers (Kuhn segments). Of course, this conclusion is an obvious consequence of the structural information given by point a).

d) Moving on to the data with more than two stickers per chain (Figures 3.2, 3.3, and 3.6), the original contribution with respect to the classic sticky Rouse models consists in using eq (3.11), instead of eq (3.13), for the so-called short-time contribution to $G(t)$, coming from the fast relaxation of the individual chains (as opposed to the slow relaxation of the network). The physics behind the use of eq (3.11) is that, in the fast relaxation of the chains, the sticky junctions exhibit a friction coefficient similar to that of the Kuhn segments, the much larger friction coefficient only affecting the slower relaxation of the network topology. In other words, in eq (3.13) of the classical theory the sum over the modes is made by assuming that the sticky points are essentially fixed in 3D space because of their large friction coefficient, i.e., the slower modes of the fast chain motion are completely cut off. In reality, the sticky points move in space towards equilibrium conformations of the network, thus dissipating energy. This appears to explain why eq (3.11) gives a better fit of the G'' minimum (see Figures 3.2 and 3.3).

e) Concerning the slow network relaxation, Figure 3.6 shows explicitly that the effective lifetime of the sticky junctions in the network is several times longer than the lifetime of the same junctions in the unconstrained situation of the long-associated chains not forming a network, i.e., those of Figure 3.5. As mentioned in Section 3, this result confirms for the first time the suggestion advanced long ago by Rubinstein and Semenov [107].

f) Last, but not least, it is worth comparing predictions that make use of the theory we developed for randomly-distributed stickers (requiring calculation of the eigenvalues of the matrix in eq (3.5)) with those obtained with the uniform sticker distribution of the classic sticky-Rouse model. This is done in Figure 3.7 for the data already examined in Figure 3.2, where, according to the authors [74], stickers are distributed randomly. Red and blue curves were obtained with the same values of the parameters, and both make use of eq (3.11). Superiority of the predictions with a random sticker distribution (red curve) over those for the uniform case is apparent.

Note finally that, as mentioned in the Introduction, the algorithm developed by Jiang et al. for a random distribution of stickers is not equivalent to that proposed here. Indeed, their model assigns a definite value of the friction coefficient to all Kuhn

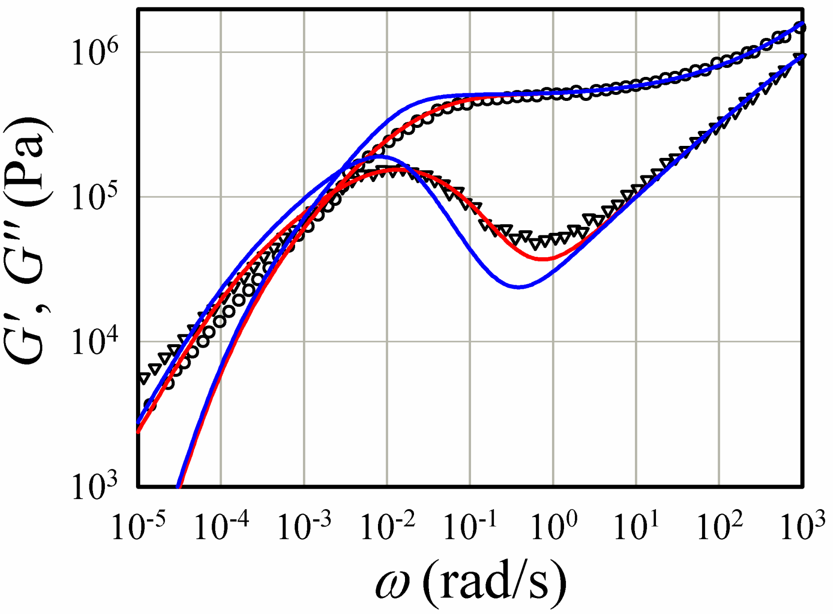

Figure 3.7: Random vs. uniform sticker distribution. - For the data in Figure 3.2 random distribution of stickers generates the red curves (as in Figure 3.2),while a Rouse-like uniform distribution gives the blue curves.

segments, and hence a large value ζ to the Kuhn segments occupied by the stickers. Therefore, at short and intermediate times, those Kuhn segments are in fact fixed in space, contrary to the physical picture described by the model developed in this paper. Of course, many-chain models like those developed by Masubuchi and coworkers (see e.g. [85, 87]) can effectively, but more expensively, replace the single-chain model suggested here.

4

Unentangled Polymer Melts are not Simpler than Entangled Ones

4.1 Introduction

Since we shall concentrate on the viscosity behaviour of polymer melts, it is important that we first emphasize what polymer melts is, in the context of the shear viscosity. Polymer melts are highly viscous liquids, possessing non-Newtonian and viscoelastic properties. These properties result in very complicated stress relaxation and flow behavior in response to a deformation. For example, under shear flow or extensional flow, the stress is a function of the whole deformation history rather than just of deformation rate (as in simple liquids) or of deformation amplitude (as in simple solids).

The configurations of deformed polymer molecules (melts) subject to flow manifest themselves in anisotropic quantities such as the stress and optical tensors. Understanding the physics of polymer melts in simple flows is crucial in order to develop molecular models and constitutive equations which can subsequently be implemented for more complex flows and geometries.

4.1.1 Physics of Deformecd Polymer Melts Subject to Flow

4.1.1.1 Unentangled vs Entangled Melts in Shear Flow

If a start-up shearing test is continued until the stresses reach their steady state values, the rheological response of the material is described completely by three functions of the shear rate. These are the viscosity and the first and second normal stress differences, which were defined by Eqs. (4.1), (4.2), and (4.3).

$$\eta \equiv \sigma_{xy}/\dot{\gamma} \tag{4.1}$$

$$N_1 \equiv \sigma_{xx} - \sigma_{yy} \tag{4.2}$$

$$N_2 \equiv \sigma_{yy} - \sigma_{zz} \tag{4.3}$$

The three material functions of steady simple shear $\eta(\dot{\gamma})$, $N_1(\dot{\gamma})$, and $N_2(\dot{\gamma})$ are called the viscometric functions, and they provide a complete description of the behavior in steady simple shear of an isotropic polymer, i.e., one that does not form a liquid crystal or another ordered phase at rest.

Of the viscometric functions, the viscosity is the easiest to measure and the one most often reported. As in the case of Newtonian fluids, the viscosity depends on temperature and pressure, but for polymeric fluids (Non-Newtonian) it also depends on shear rate, and this dependency is quite sensitive to molecular structure. In particular, the curve of viscosity versus shear rate can be used to infer the molecular weight distribution of a linear polymer. This curve is also of central importance in plastics processing, where it is directly related to the energy required to extrude a melt.

At sufficiently high shear rates, the viscosity often approaches a power-law relationship with the shear rate. Figure 4.1 is a plot of viscosity versus Weissenberg number for unentangled polystyrene melts, and it shows a slope of -0.5 when $W_i > 1$[109, 122]. Figure 4.2 displays the relationship for entangled polystyrene melts, and it indicates a slope of -0.8 when $W_i > 1$[25].

4.1.1.2 Unentangled vs Entangled Melts in Elongational Flow

The nonlinear rheological behavior under uniaxial elongation was examined for unentangled melts of polystyrene by Matsumiya et al [90] (C.F. Figure 4.3). The steady state shear viscosity, η_E, exhibites strain-rate-hardening and then strain-rate-softening on an increase of the Weissenberg number $Wi \geq 0.3$ ($Wi = \dot{\gamma}\tau_R$, with $\dot{\gamma}$ and τ_R being the shear rate and the Rouse relaxation time in the linear viscoelastic regime, respectively). For the unentangled melts, the hardening and softening are free from any entanglement nonlinearity, so that the hardening was unequivocally related to the finite extensible nonlinear elasticity (FENE) of the chain, and the softening, to the

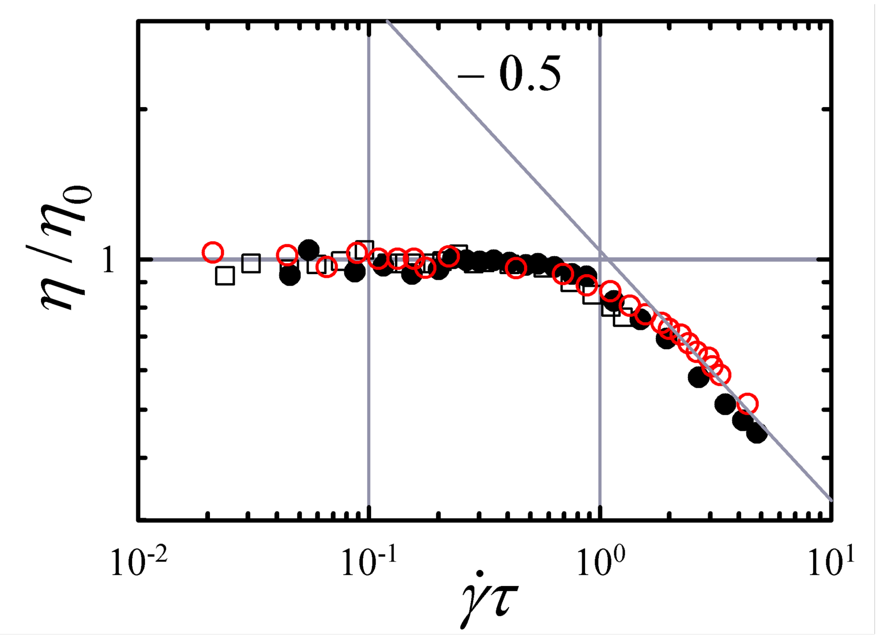

Figure 4.1: Steady-state shear viscosity normalized with zero shear viscosity as a function of Weissenberg number: Unentangled PS melts in shear - $M_\omega = 10k, 14k, 20k$

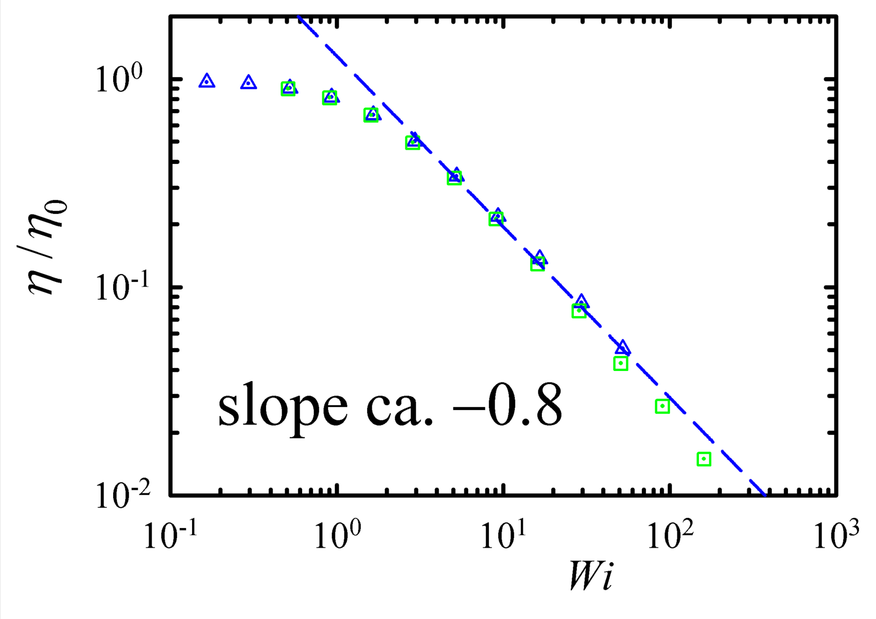

Figure 4.2: Steady-state shear viscosity normalized with zero shear viscosity as a function of Weissenberg number: Entangled PS melts in shear - $M_\omega = 133k, 185k$[25, 47]

suppression of the FENE effect due to reduction of the segment friction ζ occurring for the highly stretched and oriented chain.

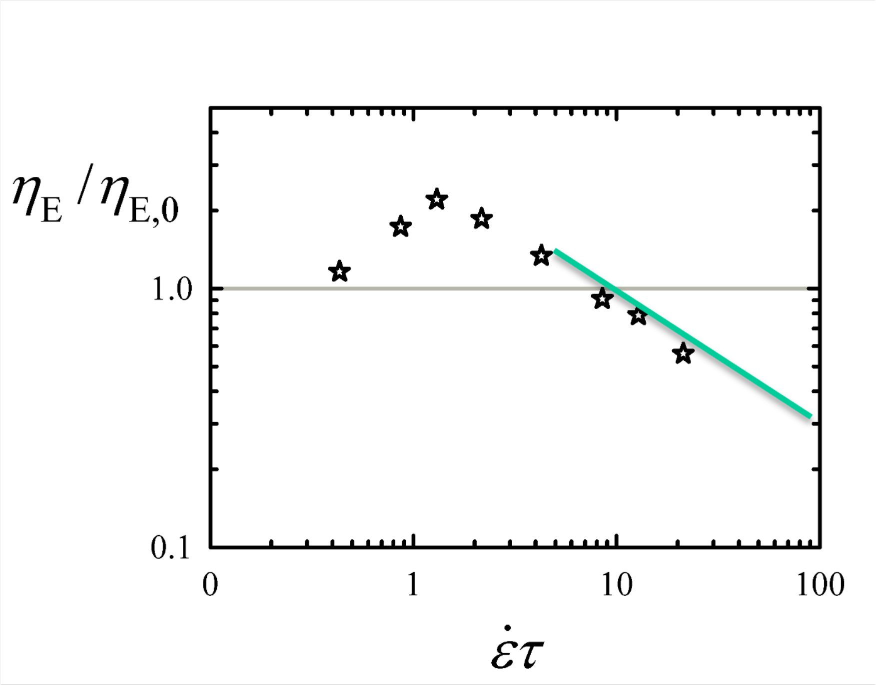

Figure 4.3: Steady-state extensional viscosity normalized with zero shear viscosity as a function of Weissenberg number: Unentangled PS melts in extension - $M_\omega = 27k$

The extensional viscosity of entangled polystyrene melts was measured using a filament stretching rheometer capable of measuring at high temperatures by Huang et al, 2019, Bach et al, 2003[5, 47] with thinning viscosity exhibiting a power-law dependence on stretch rate with an exponent of about $-1/2$.

The steady-state extensional viscosities are plotted against Weissenberg number $\dot{\varepsilon}\tau$ in Figure 4.4 for two nearly monodisperse linear PS melts with molar mass of 133000 g/mol and 185 000 g/mol linear molecules. The linear chains exhibit a transition from constant viscosity to a power-law behavior at about the inverse reptation time $(1/\tau_d)$ with no apparent change in behavior at the inverse Rouse time, as Bach et al[5] observed .

The -0.5 exponent at high extensional rates has been observed with a range of polymer melts, albeit all with free ends, including model linear [5] and star [48] polystyrene,

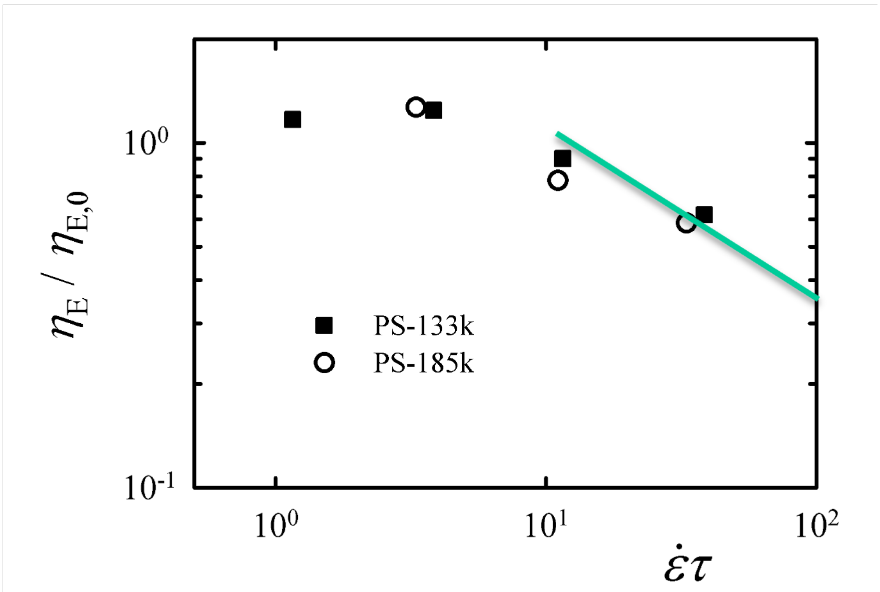

Figure 4.4: Steady-state extensional viscosity normalized with zero shear viscosity as a function of Weissenberg number: Entangled PS melts in extension - $M_\omega = 133k, 85k$

long-chain branched polyethylene [2, 45], and unentangled linear chains [90].

The PS melt data reported in the above figures clearly reveal that unentangled melts are not simpler than entangled ones in fast shear and elongational flows. Indeed, unentangled melts also exhibit shear and extensional thinning, contrary to the predictions of the Rouse model that, for long time, has been considered a reasonable model for unentangled melts. Data clearly indicate the models must account for some nonlinear effects. In the next sections, we will summarise the presuma bly missing effects.

4.1.2 Finitely Extensible Nonlinear Elastic (FENE) Model

Shear-thinning is the most common type of time-independent non-Newtonian fluid behavior that can be observed. It is also called pseudoplasticity and is characterized by an apparent viscosity, which decreases with increasing shear rate.

Many works have been done to explain these phenomena in atomic length scale. The most famous one is the bead-spring Rouse model.

Some of the earliest theoretical developments in equilibrium polymer physics involved polymer models constructed from spherical beads connected by rigid rods, i.e.

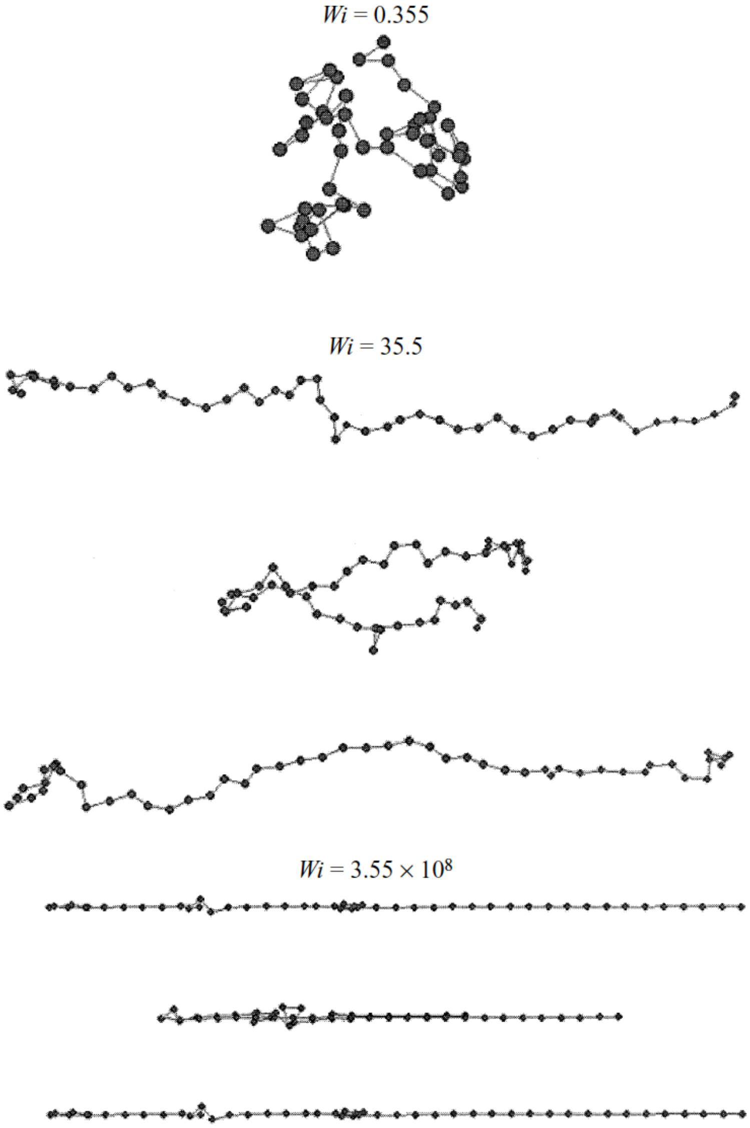

Figure 4.5: Sample chain trajectories in steady shear flow for $N = 50$ and $Wi = 0.355$; 35.5 and 3.55×10^8.[32] - For polymer melts under shear flow, the end-to-end distance of polymer chains becomes larger with increasing of Weissenberg number $Wi \geq 0.3$ ($Wi = \dot{\gamma}\tau_R$, with $\dot{\gamma}$ and τ_R being the shear rate and the Rouse relaxation time in the linear viscoelastic regime, respectively).

bead-rod chains (Flory 1989)[36]. Kuhn (1934)[67] and Guth & Mark (1934)[41] showed that the probability distribution function for the separation of the chain ends for 'phantom' bead-rod chains is a Gaussian. Using statistical thermodynamics it can be shown (Treloar 1975[127]) that the force required to increase the chain end-to-end separation is proportional to the end-to-end separation, i.e. the entropic force behaves as a Hookean spring for small deformations. For larger deformations Kuhn & Grun (1942)[68] showed that the entropic force is given by the inverse Langevin function. These entropic forces derived from the bead-rod model are the fundamental starting point for most bead-spring models, where the spring represents the entropic force. Bead-spring dumbbell models have been studied extensively and have been useful in developing constitutive equations for polymer solutions (Bird et al. 1987[16]; [84]Doi & Edwards 1986; Larson 1988[70]).

Inspired by the success of the rigid dumbbell kinetic theory [17] in describing qualitatively a wide range of shear-rate dependent viscoelastic phenomena, Warner et al, 1972[132] developed a dumbbell model with a finitely extensible nonlinear elastic (FENE) connector to understand the transition in behavior between the rigid dumbbell and the Hookean spring dumbbell. The finitely extensible connector is closer to the behavior of a macromolecule since a long chain molecule is neither rigid as is a rigid dumbbell nor infinitely expandable as is a Hookean spring dumbbell.

$$\boldsymbol{F}^c_j = \frac{H\boldsymbol{Q}_j}{[1-(Q_j-Q_0)^2]}, \tag{4.4}$$

where H is the spring constant, $\boldsymbol{Q}_j$ is the connector vector from bead j to bead $j+1$, Q_0 is the maximum end-to-end distance of a link in the chain, and $\boldsymbol{F}^c_j$ is the tension in the jth connecting spring of the chain.

The FENE-P chain, that is, the finitely extensible non-linear elastic dumbbell with the Peterlin approximation, has been used extensively to describe the rheological behavior of dilute polymer solutions.

$$\boldsymbol{F}^c_j = \frac{H\boldsymbol{Q}_j}{[1-\langle (Q_j-Q_0)^2\rangle]}, \tag{4.5}$$

where the angular brackets indicate a configuration average.

Wedgewood et al, 1991 [135] developed a model which retains the form of the FENE-P chain, but allows the use of normal coordinates. To achieve this goal, they replaced the denominator of the FENE-P spring force with an expression which was invariant under the transformation to normal coordinates, specifically writing as

$$\boldsymbol{F}_j^c = \frac{H\boldsymbol{Q}_j}{\left[1 - \sum_{j=1}^{N-1}\langle (Q_j - Q_0)^2\rangle/(N-1)\right]}, \tag{4.6}$$

This model was called the FENE-PM model where the M stands for the mean value that appears in the denominator.

To construct a spring whose length can only fluctuate within a very small range around the value of the rod length Q_0 so that the spring behaves similarly to a rigid link in the freely jointed chain, Hsieh, et al, 2006[46] mimicked the formulation of the FENE spring law and the Fraenkel spring law, where the former is finitely extensible and the latter has a nonzero equilibrium length. The FENE-Fraenkel springs were defined by

$$\boldsymbol{F}_j^c = \frac{H(Q_j - 1)}{[1 - (1 - Q_j)^2/s^2]} \frac{\boldsymbol{Q}_j}{Q_j}, \tag{4.7}$$

where s is the extensibility parameter that defines the maximum possible deviation between the actual spring length and the natural spring length. The FENE-Fraenkel model turns out to be efficient because it allows use of a larger time step and it yields less noisy results.

In the bead-spring model, the spring represents an entropic restoring force and the beads act as sources of friction. Above we have discussed the spring connector applied in the fast flow. Next we shall present the bead friction story.

4.1.3 Flow-induced Reduction of Monomeric Friction

In the polymeric melts, the friction of beads was thought of as being caused by the motion of a chain relative to the rest of the material[97]. Molecular theories of nonlinear viscoelasticity of polymeric melts usually assume, implicitly more often than explicitly, that the friction coefficient ζ of the Kuhn segment of the polymer maintains the same value, ζ_{eq}, that is observed close to equilibrium, i.e., in linear viscoelasticity. However, only in recent times, it was found necessary to account for an effect that is important in fast flows: the friction coefficient ζ of the monomeric unit (Kuhn segment) changes because of the flow-induced co-alignment of the molecules[51].

Specifically, for polystyrene (PS), ζ is found to decrease in fast elongational flows, seemingly even by a large amount. The ζ reduction has been linked to the increase in the order parameter of the Kuhn segments, although the relationship between them (expected to be chemistry-dependent) cannot easily be predicted theoretically. However, such relationship has been determined through molecular dynamics of shear flows of PS oligomers[52], as well as from stress relaxation data following elongational flows of high-molar-mass PS melts[139].

ζ reduction has been unequivocally demonstrated by the elongational flow data of unentangled PS melts reported by Matsumiya et al[90]. As emphasized by those authors, the advantage of using unentangled polymers instead of entangled ones resides in the fact that, for the latter, other nonlinear effects are simultaneously present (convective constraint release, disentanglement), which are absent in unentangled polymers. Moreover, in unentangled polymers, orientation and stretch take place simultaneously at the onset of the nonlinear response, whereas in entangled ones, nonlinearities start because of flow-induced tube orientation while chain stretch (which reduces ζ) occurs only in faster flows (faster than the reciprocal Rouse time of the chain)[84]. A ζ reduction effect in unentangled polymers had also been noted by Masubuchi et al[88]. through KremerGrest (beadspring chains) molecular dynamics simulations of stress relaxation after cessation of fast elongational flows. However, the KremerGrest chemistry gave rise to a ζ reduction effect much smaller than that found by Matsumiya et al[90]. The dependence of the ζ reduction effect on the chemistry of the polymer chain has been confirmed by Matsumiya et al.,[90] who, together with PS, also report experiments on poly(p-tertbutylstyrene) unentangled melts.

In analyzing their data, Matsumiya et al.[90] model the unentangled polymer as a finitely extensible (FENE) beadspring Rouse chain with a pre-averaged FENE effect. The ζ reduction is first estimated by them from the elongational steady-state results in the form of a dependence of ζ on the elongational stress. However, they find that the same dependence cannot explain the transient startup data, and even less the relaxation data following cessation of elongational flow. They argue that the model failure in the transient results might be due to a delay in the ζ reduction with respect to the flow-induced stretch/orientation of the polymer chains. However, they find that the same dependence cannot explain the transient startup data, and even less the relaxation data following cessation of elongational flow. They argue that the model failure in the transient results might be due to a delay in the ζ reduction with respect to the flow-induced stretch/orientation of the polymer chains.

To illustrate the ζ reduction effects explicitly clear, we reproduced the Figure 4 of Ianniruberto et al. [54] and the Figure 9 of Ianniruberto et al. [38] here. Figure 4.6 and Figure 4.7 show the comparisons of viscometric functions predictions between with ζ reduction and without ζ reduction in elongational flow and shear flow, respectively. Both of them obviously indicate that predictions without ζ reduction are not enough to fit the data.

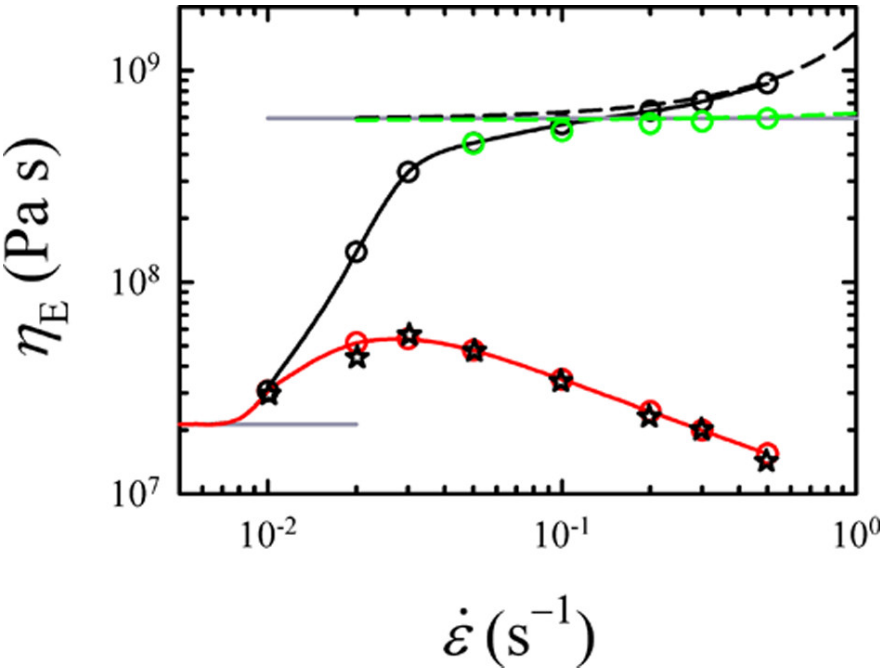

Figure 4.6: Steady-state elongational viscosity vs stretch rate. - Black stars are data from Matsumiya et al.[90] Red circles (and the red spline through them) are model predictions from the Figure 3 in Ianniruberto et al. [54]. Black circles (and the black spline through them) are model predictions without ζ reduction from Figure 2 in Ianniruberto et al. [54]. Green circles are model predictions without ζ reduction but with $\tilde{H} = 5000$ (rather than 500). Dashed black and green lines are viscosities of fully extended Fraenkel chains with $\tilde{H} = 500$ and 5000, respectively. The lower gray line is the LVE limit, while the upper one gives the viscosity of fully aligned beadrod chains.Reproduced with permission from ref [38].

Very recently, Watanabe et al [134] investigated the effects of the local elastic strength κ, segmental friction coefficient ζ, and the Brownian force intensity B of polymer chains in a melt on the nonlinear viscoleastic response and conformation. They supposed that these three separate variables are expected to change under fast

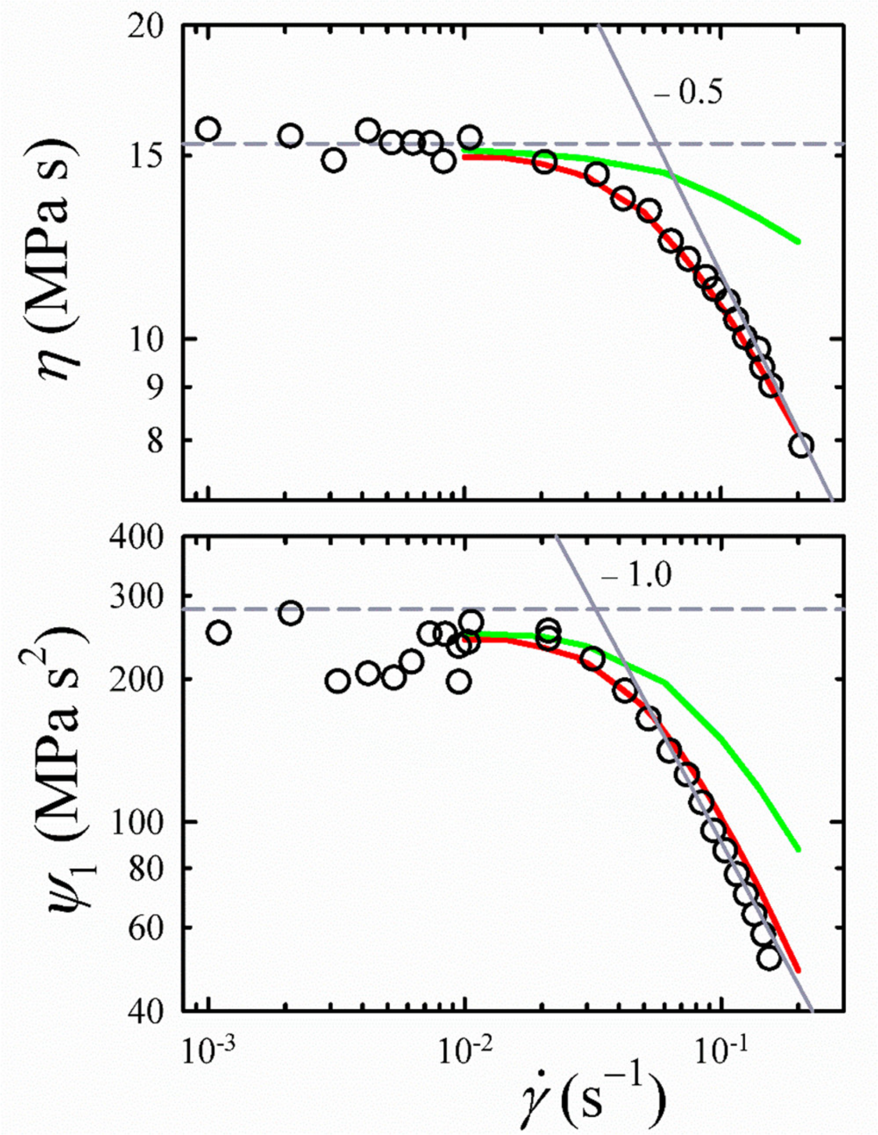

Figure 4.7: Unentangled PS melt (M = 13.7 kDa) viscosity and first normal stress difference coefficient vs shear rate, top and bottom panels, respectively. - Symbols are data from Santangelo and Roland [109], approaching power laws (solid gray lines) with the indicated slopes. Dashed gray lines mark the zero-shear values. Red and green curves are Fraenkel chain predictions with and without friction reduction, respectively[56]. Reproduced with permission from ref [38].

flow. The FENE-PM model of Wedgewood and co-workers (that adopts a FENE spring strength κ preaveraged for all springs, just as described above)[135] was modified by allowing the bead friction ζ to decrease with the tensile stress σ_E, namely, with the spring orientation and stretch that determine σ_E. The modified model also described time evolution of the stress growth and decay coefficients, $\eta_E^+(t, W_i)$ and $\eta_E(t, W_i)$, on startup and cessation of extensional flow at relatively low W_i, given that ζ determined from the η_E data (i.e., under steady flow) was extended to time-dependent $\zeta(\sigma_E(t, W_i))$ and these $\zeta(\sigma_E(t, W_i))$ and $\sigma_E(t, W_i)$ were calculated self-consistently in each step of the time evolution in the model.

Currently, a full set of rheological and structural data for unentangled melts obtained by experiments can not be found in the literature. However, Xu et al.[138] reported rich data on the Kremer-Grest melts under shear flow using nonequilibrium molecular dynamics (NEMD) simulations. We will utilize Xu et al's data on Kremer-Grest unentangled melts to check Watanabe's recipe.

4.2 Data on Polymer Kremer-Grest Melts under Fast Shear Flow

As mentioned at the end of Introduction 4.1, to our knowledge, no other data on unentangled monodisperse melts are available in the literature. We then move on to the single information on unentangled monodisperse polymers in fast shear flows contributed by Xu, et al (2014)[138] using nonequilibrium molecular dynamics (NEMD) simulations.

In their system, the intermolecular and intramolecular excluded-volume interactions were taken into account by the repulsive, shifted, and truncated $6-12$ Lennard-Jones (LJ) potential. Within one polymer chain, the entropic restoring energy was taken into account by the FENE potential. The LJ+FENE chain model was applied to study the effects of flow on the rheological (e.g., viscosity and normal stress differences), structural (e.g., chain end-to-end distance, gyration tensor, orientation resistance parameter), and dynamical (e.g., tumbling frequency) properties through NEMD simulations.

By fitting the simulation curve in the shear thinning regime with a power-law expression of the form $\eta \sim \dot{\gamma}_b$, Xu et al (2014) found that the best curve fits were obtained for $b = -0.7$ for shear rates $\dot{\gamma}$ in the interval $1/\tau_0 < \dot{\gamma} < \dot{\gamma}_c$, and for $b = -0.37 \pm 0.02$

for shear rates corresponding to $\dot{\gamma} > \dot{\gamma}_c$. Analogously, Baig et al (2010)[9] reported that the exponent b had the values of $b = -0.89 \pm 0.06$ and $b = -0.44 \pm 0.05$,respectively.

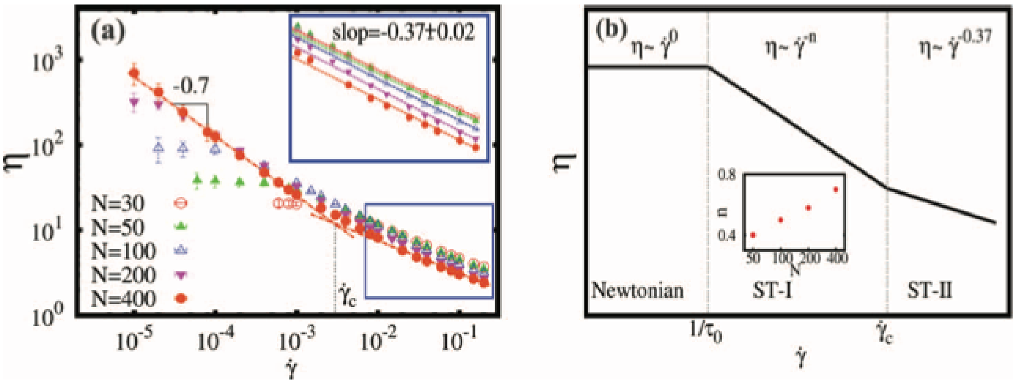

Figure 4.8: Shear viscosity ζ as a function of shear rate $\dot{\gamma}$ for different chain lengths $N = 30, 50, 100, 200$, and 400. - Two orange dashed lines correspond to $\zeta \sim \dot{\gamma}^{0.7}$ and $\zeta \sim \dot{\gamma}^{0.37}$, used to determine the critical shear rate $\dot{\gamma}_c = 0.003$ for $N = 400$. The inset displays the same data marked by the blue frame; the dashed lines indicate the dependences of ζ on $\dot{\gamma}$. (b) Schematic illustration of the shear thinning behavior. Inset: The dependence of scaling exponent n on chain length N in the ST-I regime.

We need models that predict the observed behavior, especially for the simple unentangled case. The more so because the behavior of the normal stress differences at high shear rates are pretty different from that at low shear rates (see Figure. 4.9).

Even though we have introduced the normal stress differences in eqs (4.2) and (4.3), the normal stress coefficients appear in the literature very frequently. Dealy et al (2018)[31] showed a good explanation on the origin of the definitions of normal stress coefficients.

From the basic axioms of continuum mechanics, it is possible to show that for a simple fluid subjected to a perfectly smooth (infinitely differentiable) strain history the stress tensor is given by an infinite series in terms of Rivlin-Ericksen strain tensors. The first three terms of this series show the earliest departures from Newtonian behavior as the strain rate increases from zero. This truncated series is said to model the behavior of a second-order fluid, although this is a misnomer, as it does not describe the behavior of any actual fluid but is rather an approximation of the behavior of a simple fluid in a flow that differs only infinitesimally from the rest state. According to the second-order

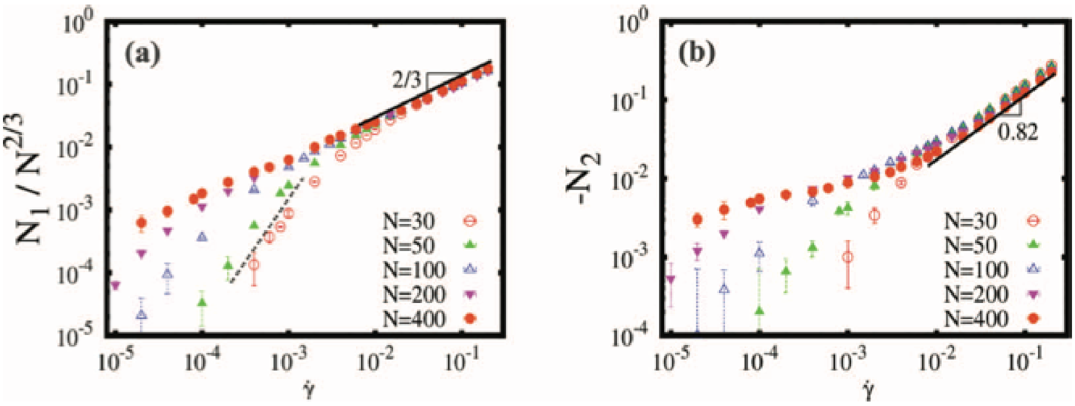

Figure 4.9: Normal stress differences - (a) Scaled first normal stress difference N_1 as a function of shear rate. The dashed line indicates quadratic behavior for $\dot{\gamma} < \tau_0^1$. (b) Negative second normal stress difference N_2 as a function of shear rate.

truncation, in simple shear flow the shear stress is proportional to the shear rate, while the first and second normal stress differences are quadratic in the shear rate. This inspired the definitions of the first and second normal stress coefficients as follows[31].

$$\Psi_1(\dot{\gamma}) \equiv N_1(\dot{\gamma})/\dot{\gamma}^2 \tag{4.8}$$

$$\Psi_2(\dot{\gamma}) \equiv N_2(\dot{\gamma})/\dot{\gamma}^2 \tag{4.9}$$

Figure 4.9 indicates that in unentangled melts N_2 is nonzero. Figure 4.10 shows that the ratio N_2/N_1 at low rates is ca. 0.1 just like in entangled melts. In entangled melts N_2/N_1 first decreases with increasing $\dot{\gamma}$ (as observed experimentally), but, surprisingly, it asymptotically increases. Otherwise, in unentangled melts N_2/N_1 first stays constant at ca. 0.1 with increasing $\dot{\gamma}$, then it approaches the same asymptotic behavior.

In Figure 4.11, the left figure indicates that the end-to-end distance appears to approach one half the fully extended length L with increasing $\dot{\gamma}$. We will examine whether it is due to tumbling. The right figure shows the end-to-end distance distribution becomes nearly a constant in fast flows.

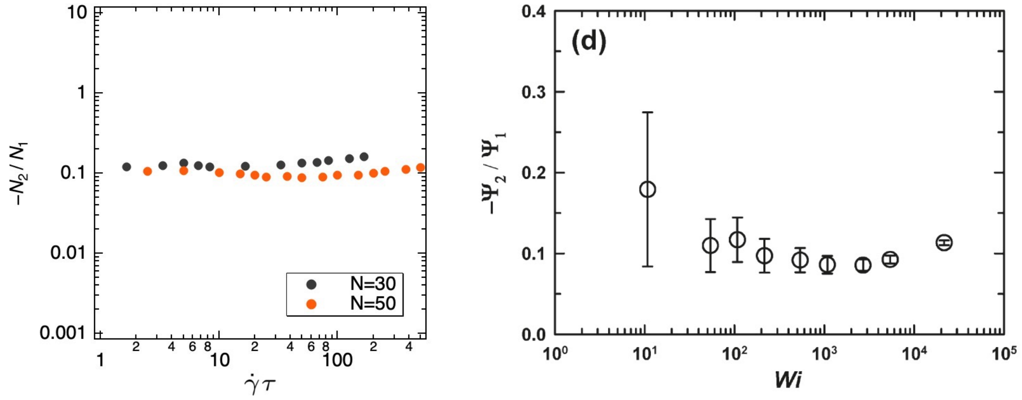

Figure 4.10: The ratio of N_2 to N_1 - Ratio of N_2/N_1 in unentangled melts reported by Xu et al, (2014)[138]) (left) and ratio of the normal stress coefficients (equivalent to the ratio of N_2/N_1) in simulated $C_{400}H_{802}$ PE melt (entangled) reported by Baig et al (2010) [9] (right)

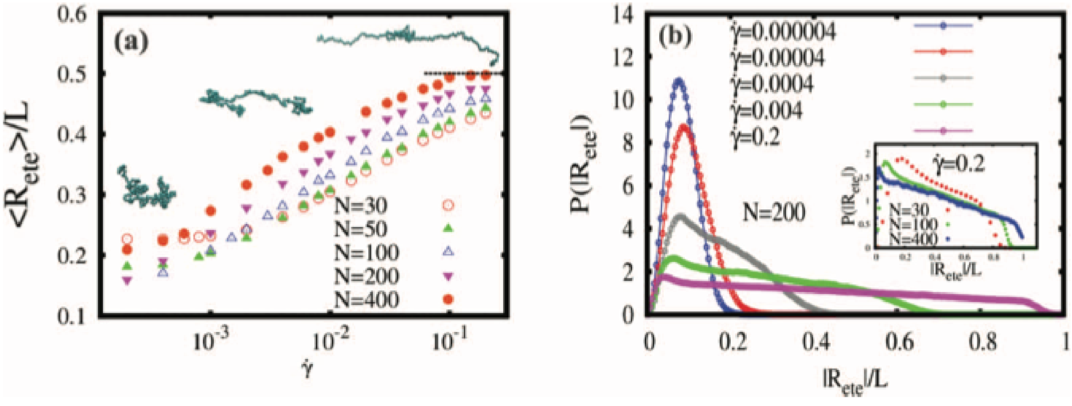

Figure 4.11: Structural properties of polymer melts under shear flow. - (a) Scaled root-mean-square end-to-end distance $\langle R_{ete}\rangle$ as a function of shear rate. The dashed line corresponds to $\langle R_{ete}\rangle/L = 0.5$. The insets show the snapshots of a polymer chain ($N = 200$) at various shear rates, from bottom to top $\dot{\gamma} = 0.00001$, 0.001, and 0.1, respectively. (b) Probability distribution functions of $|\mathbf{R_{ete}}|/L$, $P(|\mathbf{R_{ete}}|)$, for $N = 200$ at various shear rates. Inset: $P(|\mathbf{R_{ete}}|)$ at $\dot{\gamma} = 0.2$ for several chain lengths.

4.3 Interpretation of Kremer-Grest Melts Data with Watanabe's Recipe

A remarkable difference between entangled solutions and melts of linear polystyrene (PS) under fast flow was revealed by Sridhars group[13, 14, 141] and Hassagers group[5, 35].

The left figure in Figure 4.12 indicates that the entangled solution exhibits strain-softening on an increase of elongation rate $\dot{\varepsilon}$ and then significant strain-hardening on a further increase of $\dot{\varepsilon}$. In contrast, the entangled melt (data of Bach et al in the right figure) exhibits no hardening even at high $W_i (\gg 1)$. This lack of hardening strongly suggests that the entangled linear chains in a melt are not extremely stretched even at high W_i.

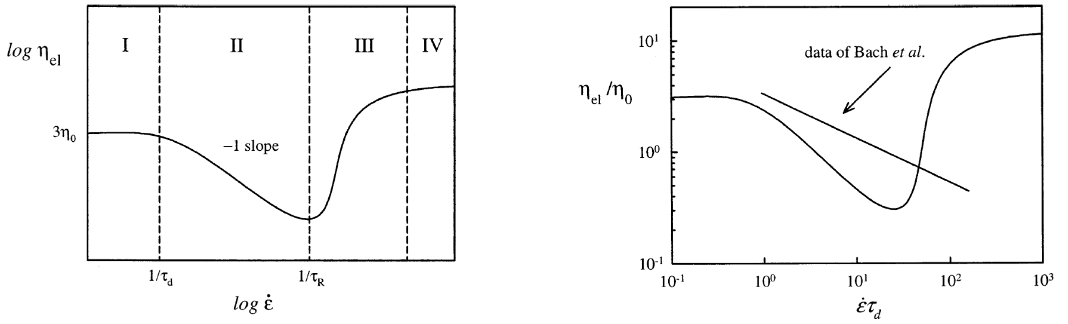

Figure 4.12: Steady-state elongational viscosity of solutions and melts - Left: Steady-state elongational viscosity vs elongation rate $\dot{\varepsilon}$ as predicted by standard molecular theories of entangled polymers. From the Trouton value $3\eta_0$ at low $\dot{\varepsilon}$, the viscosity first decreases as $1/\dot{\varepsilon}$ and then increases again when chains stretch out. Right: Same as in left figure together with data of Bach et al., showing that the standard theory does not seem to apply to polymer melts.[82]

To address this problem, Marrucci and co-workers proposed two basic molecular mechanisms, interchain pressure effect and segmental friction-reduction. Very recently, Watanabe's group studied the effect of the changes of spring strength κ, monomeric friction ζ, and Brownian force $\boldsymbol{F}_B$ on nonlinear rheological properties and conformation. They proposed that the changes in κ, ζ, and $\boldsymbol{F}_B$ should occur under fast shear flow. κ, ζ, and $\boldsymbol{F}_B$ were regarded as separate parameters that determine the chain dynamics as a function of the flow rate.

On the basis of the Smoluchowski equation for the conformational distribution function, Matsumiya et al (20018)[90] analyzed the nonlinear rheological behavior by introducing the $\zeta-$reduction into the FENE-PMRouse model[135] but with no change in the Brownian force intensity B under flow. The Langevin equation (eq (4.10)) is equivalent to the Smoluchowski equation but includes the Brownian force explicitly, so that an effect of changes of B on the rheological behavior, one of the main subjects of this study, can be examined more straightforwardly with an analytical perspective for the Langevin equation. Thus, Watanabe et al [134] adopted eq (4.10) as the starting equation.

4.3.1 Description of Watanabe's Model

A Rouse chain composed of $N+1$ beads (Rouse segments) and N springs was considered in Watanabe et al (2021)[134]. Each spring was composed of g Kuhn segments, and the chain as a whole has $n_{total} = gN$ Kuhn segments. N (or g) can be chosen rather arbitrarily due to the well-known Rouse scaling[76, 84, 133].

For the Rouse chain on startup of constant-rate shear flow, the time evolution of the position vector of the nth bead, $\boldsymbol{r}(n,t)$, is described by the Langevin equation as

$$\zeta(t)\left[\frac{\partial \boldsymbol{r}(n,t)}{\partial t} - \boldsymbol{v}(n,t)\right] = \boldsymbol{\kappa}(t)\sum_{m=0}^{N} A_{nm}\boldsymbol{r}(m,t) + \boldsymbol{F}_B(n,t), \tag{4.10}$$

where $\zeta(t)$ and $\boldsymbol{\kappa}(t)$ denote the bead friction coefficient and spring strength at time t, respectively, and $\boldsymbol{F}_B(n,t)$ stands for the thermal Brownian force acting on the nth bead at t. A_{nm} is the nmth component of the Rouse matrix $\boldsymbol{A}$ given by

$$\boldsymbol{A} = \begin{bmatrix} -1 & 1 & 0 & 0 & \cdots & \cdots & 0 \\ 1 & -2 & 1 & 0 & \cdots & \cdots & 0 \\ \cdots & \cdots & \cdots & \cdots & \cdots & \cdots & \cdots \\ \cdots & \cdots & \cdots & \cdots & \cdots & \cdots & \cdots \\ 0 & \cdots & \cdots & 0 & 1 & -2 & 1 \\ 0 & \cdots & \cdots & 0 & 0 & 1 & -1 \end{bmatrix} \tag{4.11}$$

The velocity $\boldsymbol{v}(n,t)$ of a frictional medium at the position of the nth bead is expressed in terms of the ξ-component of the bead position vector, $r_\xi(n,t)$ with $\xi = x, y, z$, as

$$\boldsymbol{v}(n,t) = \begin{bmatrix} \dot{\gamma} r_y(n,t) \\ 0 \\ 0 \end{bmatrix} \tag{4.12}$$

where $\dot{\gamma}$ is the strain rate in the shear flow field. The x and y directions are chosen to be the velocity and velocity gradient directions in eq (4.12).

The Brownnian force is characterized by

$$\begin{aligned}&\langle \mathbf{F}_B(n,t)\rangle = 0,\\ &\langle \mathbf{F}_B(n,t)\mathbf{F}_B(m,t')\rangle = B(t)\delta_{nm}\delta(t-t')\mathbf{I},\end{aligned} \tag{4.13}$$

where $\langle\cdots\rangle$ indicates an average taken for all beads in the system, δ_{nm} is the Kronecker delta, and $\delta(t-t')$ is the delta function.

A few comments need to be made for this model. Wingstrand[137], Alvarez[92], Masubuchi[86], Watanabe[90], and their co-workers have demonstrated that the ζ-reduction is a local phenomenon, which implies two facts at least. First, the friction magnitude should be dependent on the chemical structure of the monomeric segments. In fast shear flow, the bead friction ζ can be assumed to decrease with the tensile stress σ_E. Second, the segmental ζ-reduction appears to play a central role in the nonlinear shear rheology of unentangled polymer melts (as well as that of entangled polymer melts in addition to the tube pressure effect specific to entangled chains). Matsumiya and Watanabe[89] gave an explanation on the origin of friction reduction in atomic length scale. In the coarse-grained length scale, the friction unequivocally represents dissipation of mechanical energy through motion of the monomeric segments. A given monomeric segment (probe) should interact with the surrounding segments according to a spatial arrangement (position and orientation relative to the probe) of those segments, so that the energy-dissipating motion of the probe, driven by that interaction, should depend on this spatial arrangement. Then, a characteristic time τ^* of the probe motion in the atomic length scale should change with the relative orientation of surrounding segments. Specifically, the segment motion would become faster if all segments are oriented in the same direction, which results in the ζ-reduction in the coarse-grained length scale.

In the linear viscoelastic (LVE) regime, the fluctuationdissipation theorem (2.7) is valid and the (squared) intensity of the Brownian force, $B(t)$, appearing in eq (4.13), reduces to the equilibrium intensity $B_{eq} = 2\zeta_{eq}k_BT$, with ζ_{eq}, k_B, and T being the friction coefficient at equilibrium, the Boltzmann constant, and the absolute temperature, respectively. In contrast, under flow, Matsumiya and Watanabe[89] thought that $B(t)$ may deviate from B_{eq} (and may change with t in the transient state). Their assumption was supported by the following statement.

"...the isotropic white noise character of the Brownian force $\boldsymbol{F}_B(n,t)$ is assumed to be deduced from the fluctuation dissipation theorem in the coarse-grained length and time scales cf. eq (2.7). However, in the time scale of segmental motion explained above, $\boldsymbol{F}_B(n,t)$ would have a memory characterized by the time τ^* thereby not behaving as the white noise (even in the absence of flow). For this case, the term $\delta(t-t')$ appearing in eq (2.7) should be replaced by a memory decay function having the characteristic time τ^* (this τ^* may change with $S(t)$) (S is the average orientational anisotropy in the presence of nematic coupling defined in eq (13) in Matsumiya et al[89]). Furthermore, under fast flow, the fluctuation-dissipation theorem may become invalid. Then, $\boldsymbol{F}_B(n,t)$ may exhibit anisotropy according to the relative orientation of the segments under flow, so that the isotropic unit tensor $\boldsymbol{I}$ appearing in eq (2.7) may need to be replaced by an anisotropic tensor. In addition, the intensity of $\boldsymbol{F}_B(n,t)$ shown in eq (2.7) , directly related to the scalar frictional coefficient ζ, may need to be modified. Because the tensile stress σ_E is directly dependent on z and x components $\boldsymbol{F}_B(n,t)$ (as can be noted from eq (4.10)), these changes of $\boldsymbol{F}_B(n,t)$ should affect the simulation results at short t rather significantly. Combination of full-atomic and coarse-grained simulations would be helpful also for quantifying these features of $\boldsymbol{F}_B(n,t)$ under fast flow and improving the analyses explained in the previous sections."

We will check this assumption by comparing the rich data of Xu et al (2014)[138] with the model of Watanabe et al (2021)[134]. The results of the model in eqs (4.10 - 4.13) are summarized as

$$\frac{\eta}{\eta_0} = \frac{r_B}{r_\kappa} \tag{4.14}$$

$$\frac{\Psi_1}{\Psi_{1,0}} = \frac{r_B r_\zeta}{r_\kappa^2} \tag{4.15}$$

with

$$r_\zeta = \frac{\zeta_{sf}}{\zeta_{eq}}, \quad r_\kappa = \frac{\kappa_{sf}}{\kappa_{eq}}, \quad r_B = \frac{B_{sf}}{B_{eq}}. \tag{4.16}$$

$$\frac{\langle \boldsymbol{R}^2\rangle_{sf}}{\langle \boldsymbol{R}^2\rangle_{eq}} = \left(\frac{r_B}{r_\zeta r_\kappa}\right)\left\{1 + \frac{(N+1)[(N+1)^4-1]}{45N}(W_i^*)^2\right\} \tag{4.17}$$

The subscript sf appearing in eqs (4.14 - 4.17) emphasizes that the quantities shown therein are defined under steady flow. In eq (4.17), W_i^* denotes a reduced Weissenberg number under shear flow defined by

$$W_i^* = 2\sin^2\left[\frac{p\pi}{2(N+1)}\right]\frac{r_\zeta}{r_\kappa}\dot{\gamma}\tau_{R,eq}, \tag{4.18}$$

where $\tau_{R,eq} = \frac{\zeta_{eq}}{8\sin^2\left[\frac{p\pi}{2(N+1)}\right]\kappa_{eq}}$.

The eqns (4.14), (4.15) and (4.17) can be solved for r_κ, $r\zeta$, r_B by using the data of η, ψ_1 and R^2 in Xu et al (2014)[138]. The results are plotted in Figure 4.13.

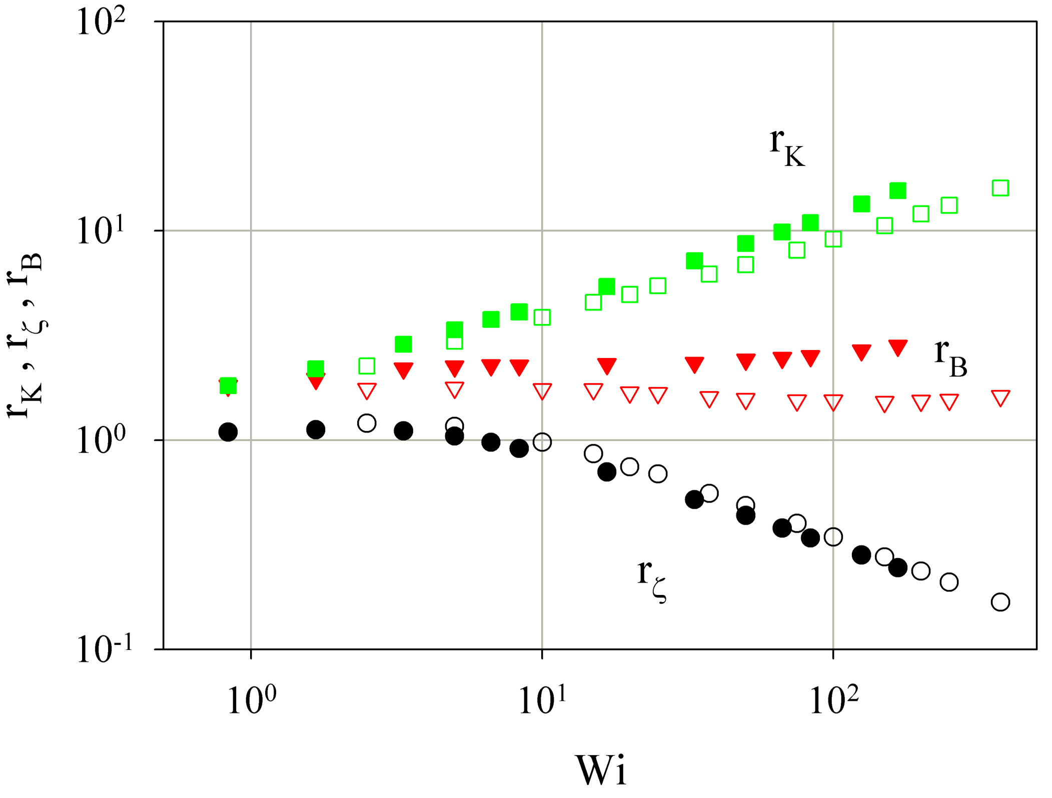

Figure 4.13: The spring strength r_κ, the friction r_ζ, and the Brownian intensity r_B as a function of Weissenberg number - Full symbols: $N = 30$, empty symbols: $N = 50$.

As shown in Figure 4.13, the spring strength r_κ increases with increasing W_i while the friction r_ζ decreases, as expected. In contrast, the Brownian intensity r_B stays almost constant, rather than decreasing together with the friction. Hence, the Brownian force under flow can be regarded as the same as it in the equilibrium state.

Results in Figure 4.13 confirm that in order to fit the data in fast steady shear flows the spring coefficient must increase with increasing shear rate, rather than staying constant as predicted by the Rouse model. In other words, finite-extensibility (FENE) effects become relevant in fast flows because of the flow-induced stretching of the molecules. However, data also indicate that FENE effects are not enough to explain the observed shear thinning behavior. Other nonlinear effects come into play. More specifically, results in Figure 4.13 also indicate that the friction coefficient must decrease with increasing the shear rate, consistently with the suggestion advanced long ago by Marrucci and Ianniruberto. Friction reduction is due to the flow-induced monomer co-alignment in the shear flow direction. Surprisingly, but consistent with Watanabes intuition, Figure 4.13 also indicates that the Brownian force intensity does not decrease together with the friction coefficient, as the fluctuation dissipation theorem would predict. Indeed, results in Figure 4.13 clearly show that the nondimensional Brownian intensity remains essentially constant with increasing shear rate. The violation of the fluctuation dissipation theorem in fast flows of polymer melts clearly emerging from Figure 4.13 confirms a similar violation shown by the molecular dynamics results of Brasiello et al [52] who independently measured both the diffusion and the mobility tensors in fast shear flows of oligostyrene melts (see their Figures 6 and 7).

In conclusion, the results reported in this chapter unequivocally confirm that successful models for fast flows of polymer melts, both unentangled and entangled, must necessarily account for flow-induced friction reduction effects, also triggering a violation of the fluctuation dissipation theorem. Unfortunately, both phenomena are expected to be chemistry dependent, and they can only be predicted by resorting to nonequilibrium molecular dynamics simulations. In the following chapter, we will attempt a fit of the unentangled melt data of Xu et al. [138] by performing suitable single-chain Brownian dynamics simulations.

4.4 Conclusions

The Physical phenomena of deformecd polymer melts subjected to flow were presented, in which two couples of comparisons were made, unentangled vs entangled melts in shear flow and unentangled vs entangled melts in elongational flow. In both flows, the steady-state viscosities approach a power-law relationship with the shear rate at sufficiently high shear rates, even though the exponent may be different. At low shear rates and under elongational flow, the unentangled melts exhibit more significant strain-hardening on an increase of the Weissenberg number W_i than the entangled melts due to the chain stretch. The strain-hardening and strain-softening are attributable to the stretch- and orientation-induced ζ reduction and the finite extensible nonlinear elasticity (FENE) effect.

Watanabe et al (2021)[134] attempted to describe the roles of the local elastic strength κ, segmental friction coefficient ζ, and the Brownian force intensity B of polymer chains in a melt by allowing κ, ζ, and B in the Rouse model to change under flow, in which a modified FENE-PMRouse model was applied. Xu et al.[138] reported rich data on the Kremer-Grest melts under fast flow, including η, ψ_1 and R^2, which is a full set of rheological and structural data required by Watanabe's model. We applied Xu et al's data into Watanabe's model with the conclusion that the Brownian force under flow almost remained the same as that at the equilibrium state.

In Watanabe's system, since they made an attempt to express effects of changes of B, ζ, and κ under flow on the nonlinear rheology of the Rouse chain in an analytical form, decoupling and pre averaging happened for all springs, which resulted in $N_2 = 0$. Nevertheless, Xu et al's (2014) [138] reported a group of non-zero N_2 data. A nonzero second normal stress difference can be a signature of the importance of topological effects, similarly to what happens in entangled melts.

In the next section, the isotropic friction reduction and anisotropic friction reduction in polymer melts will be further discussed by using Xu et al's (2014) data. The model adopted in the next section will not be pre averaging. Therefore, N_2 will not be zero.

5

Friction Reduction in Fast Flows of Unentangled Polymer Melts

5.1 Introduction

It has been thought for a long time that unentangled polymer melts are well described by the Rouse model, with the possible exception of their shear viscosity exhibiting shear thinning, and hence requiring some correction of the Rouse model[23]. A sensible modification of the Rouse model was required in fast extensional flows because the Rouse chain is indefinitely extensible, while actual polymer molecules are obviously not. Finite extensibility (FENE) corrections were therefore included where necessary[31, 46, 124].

In recent times, however, further corrections appeared indispensable in fast flows (for a review, see Matsumiya et al. (2021)[89]). Both experiments and molecular dynamics simulations of uniaxial extensional flows revealed that the extensional viscosity does not approach the expected plateau value predicted by the FENE models because of a new effect, namely the flow-induced co-alignment of the Kuhn segments (monomers) of the polymer molecules, and the consequent reduction of the monomeric friction coefficient[38, 90], an effect also observed in entangled polymers[47, 53, 86, 98, 140]. Finally, the link between the monomeric friction coefficient and the random forces due to thermal motion, known as fluctuation-dissipation theorem, (or, equivalently, the Einsteins relationship between diffusivity and friction coefficient) does not necessarily hold true away from equilibrium. This nonlinear effect was revealed by nonequilibrium molecular dynamics simulation of styrene oligomers in shear flows[52], and more recently emphasized by Watanabe and coworkers [90], who envisaged significant consequences on the rheology and flow-induced conformations of unentangled polymers in fast flows. As is well known, nonlinear data on unentangled polymers are scarce, and Watanabe and coworkers called for new data to be collected to confirm the anticipated nonlinear effects.

In this paper, we take advantage of the rich set of data obtained by Xu et al.[138] with nonequilibrium molecular dynamics simulations of several Kremer-Grest melts in fast steady shear flows to try and reproduce them by suitable Brownian dynamics simulations, with the aim of understanding the role of the nonlinear mechanisms mentioned above. Indeed, the data of Xu et al[138]. include not only the viscosity and the first normal stress difference (as is typically measured in experiments [120]), but also the second normal stress difference, the chain end-to-end distance, and all components of the gyration tensor. One should note that the second normal stress difference is predicted to be zero by the Rouse model, also in the modified version recently proposed by Watanabe and coworkers[134], while a nonzero second normal stress difference is typical of the entangled regime. Quite surprisingly, the results of Xu et al.[138] indicate that the second normal stress difference is present in unentangled melts, and that the ratio to the first normal stress difference is virtually the same as that of entangled melts. Even more surprisingly, and differently from entangled melts, the normal stress ratio in the unentangled case remains essentially constant with increasing shear rate. As suggested in this paper, the latter effect is probably due to flow-induced excluded volume interactions.

As mentioned above, single-chain Brownian simulations are used in this paper, with chains coarse grained at Kuhn segment level. To account for the inextensibility of the Kuhn segments (and consequently of the whole chain), the latter are simulated as stiff Fraenkel segments. Should the friction of the beads of the chain be isotropic, simulations give a zero second normal stress difference, because the Fraenkel chain is equivalent to the Rouse one in this respect. Hence, we endow the beads with anisotropic friction, on the plausible assumption that a bland topological hindrance is also present in unentangled polymers. The trick of an anisotropic friction was already suggested in previous works attempting to replace the tube confining entangled polymers (refs), as well as to mimic bland topological interactions in polymeric solutions at the overlap concentration $c*$ [81].

A mild topological interaction in unentangled polymers is also revealed by the fact that at equilibrium the center-of-mass friction coefficient $\zeta_c m$ is more than proportional to the chain molar mass (a parabolic relationship is reported by Svaneborg and Everaers (2020)[125]), rather than following the linear relationship predicted by the Rouse model.

5.2 Beads Endowed with Isotropic Friction

5.2.1 Fraenkel-chain Model

In unentangled polymer melts, each chain feels the surrounding chains through the excluded volume interaction (preserving the mass density and presumably not affecting chain dynamics) and through the monomeric friction coefficient ζ[84]. At equilibrium, the entropic response of unentangled polymer melts can be well-described by the Rouse model, which is well-known. Nevertheless, in fast flows, where chains become strongly extended, the Rouse model becomes inadequate, and a better model of the polymer chain is obtained by coarse-graining at the level of the inextensible Kuhn segment, described as a Fraenkel spring with a suitably large spring constant. Then unentangled polymers can be modeled as Fraenkel chains made up of beads endowed with the friction coefficient ζ and connectors of root-mean-square Kuhn length l_K having a suitably large spring constant H. In polymer melts, hydrodynamic and excluded volume interactions are screened. Hence, for unentangled melts, the equations of a Fraenkel chain (coarse graining being at Kuhn segment level) reads:

$$\mathbf{F} = H(l - l_K)\mathbf{u}, \tag{5.1}$$

where $\mathbf{F}$ is the force in the chain segment having orientation described by the unit vector $\mathbf{u}$ and H is so chosen that the current segment length l remains close to l_K.

Chain dynamics is described by the following Langevin equation

$$\zeta \left(\frac{\mathrm{d}\mathbf{R}_i}{\mathrm{d}t} - \mathbf{k} \cdot \mathbf{R}_i \right) = \mathbf{F}_{i+1} - \mathbf{F}_i + \mathbf{f}_i \quad i = 0, \cdots, N \tag{5.2}$$

$$\mathbf{F}_0 = \mathbf{F}_{N+1} = \mathbf{0}, \tag{5.3}$$

where $\mathbf{R}_i$ is the position of the ith bead, $\mathbf{k}$ is the velocity gradient, and $\mathbf{F}_i$ obeys eq (5.1) (for $1iN$) with l_i and $\mathbf{u}_i$ obeying the connectorvector relationship $\mathbf{Q}_i \equiv \mathbf{R}_i - \mathbf{R}_{i-1} = l_i\mathbf{u}_i$. The Brownian force f_i has a Gaussian distribution with $\langle \mathrm{f}_i \rangle = 0$, and $\langle \mathrm{f}_i(t)\mathrm{f}_i(t') \rangle = 2\zeta k_B T \delta(tt')I$, where $\langle \cdots \rangle$ indicates ensemble average, $k_B T$ is the thermal energy, $\delta(\cdot)$ is the Dirac delta function, and $\mathbf{I}$ is the unit tensor.

Observables are computed by averaging over a suitably large population of chains. The observables of interest are the stress tensor $\boldsymbol{\sigma}$ and the Kuhn segment order parameter tensor $\mathbf{S}$, respectively, given by

$$\boldsymbol{\sigma} = \nu \left\langle \sum_{i=1}^{N} \mathbf{F}_i \mathbf{Q}_i \right\rangle , \tag{5.4}$$

$$\mathbf{S} = \frac{1}{N} \sum_{i=1}^{N} \mathbf{S}_i, \quad \mathbf{S}_i = \frac{3}{2} \left(\langle \mathbf{u}_i \mathbf{u}_i \rangle - \frac{1}{3}\mathbf{I} \right) , \tag{5.5}$$

where ν is the number density of chains and $\mathbf{S}_i$ is the local order parameter tensor, i.e., that of the Kuhn segments located at the ith position along the chains. In the case of uniaxial elongational flows, the order parameter tensor is fully determined by the scalar order parameter S given by

$$S = \frac{1}{N} \sum_{i=1}^{N} S_i, \quad S_i = \langle u_{i,x}^2 - u_{i,y}^2 \rangle, \tag{5.6}$$

where $u_{i,x}$ and $u_{i,y}$ are components of $\mathbf{u}_i$ in a Cartesian coordinate system with the x-axis in the elongation direction. Obviously, the order parameter S is zero at equilibrium, while approaching unity when chains become increasingly oriented in the elongation direction.

Consistently with previous results[52, 53, 98, 140], it is here assumed that the monomeric friction coefficient ζ is the following decreasing function of the Kuhn segment order parameter $\mathbf{S}$

$$\frac{\zeta}{\zeta_{eq}} = \frac{1}{\left[1 + \left(\frac{S}{S_c}\right)^{\alpha}\right]^{n/\alpha}} \tag{5.7}$$

Since α will be set at a value around 2, eq (5.7) implies that, for S smaller than a critical value S_c (of order 0.1), ζ essentially remains at the equilibrium value ζ_{eq}, whereas for S larger than S_c, ζ/ζ_{eq} follows the power law $(S/S_c)^n$.

All relaxation times are assumed to be proportional to ζ through equations of the form

$$\frac{\tau}{\tau_{eq}} = \frac{\zeta}{\zeta_{eq}}, \tag{5.8}$$

where τ_{eq} is the value of τ at equilibrium.

Simulations were actually run in non dimensional units. we take the following scalings:

$$k_B T = \widetilde{k_B T} \cdot \mathrm{U}, \quad l_K = \widetilde{l_K} \cdot \mathrm{L}, \quad \tau_K = \widetilde{\tau_K} \cdot \mathrm{T}, \tag{5.9}$$

where U, L, and T are units of energy, length, and time, respectively. Hereinafter, the $^{\sim}$ symbol implies that the variables are non-dimensional. The unit of time also represents the relaxation time T of the Kuhn segment at equilibrium. Accordingly, the spring constant H and the contour length of the i-th subsegments l_i has the scalings $\widetilde{H} = \frac{H\mathrm{L}^2}{\mathrm{U}}$, $\widetilde{l_i} = \frac{l_i}{\mathrm{L}}$. The stress tensor $\boldsymbol{\sigma}$ in eq (5.4) can be written in the following form:

$$\boldsymbol{\sigma} = \nu \left\langle \sum_{i=1}^{N} \tilde{H}\mathrm{U} \left(1 - \frac{1}{\tilde{l}_i}\right) \tilde{l}_i \mathbf{u}_i \tilde{l}_i \mathbf{u}_i \right\rangle. \tag{5.10}$$

Then the stress tensor has the following scaling form:

$$\widetilde{\boldsymbol{\sigma}} = \frac{\rho}{N_{bead}} \left\langle \sum_{i=1}^{N} \tilde{H} \left(1 - \frac{1}{\tilde{l}_i}\right) \tilde{\mathbf{Q}}_i \tilde{\mathbf{Q}}_i \right\rangle, \tag{5.11}$$

where ν is the number density of chains, N_{bead} is the number of beads per chain, and ρ is the number of beads per unit volume. In comparing simulation results to data of Xu et al. [138], known values of l_K and $k_B T$ are used, while τ_K is determined by fitting linear viscoelastic data.

Before comparing predictions to the data of Xu et al. [138], however, it is worth recalling that, since unentangled melts have a relatively fast relaxation, the glassy dynamics provides a minor but non-negligible contribution to the rheological response[90]. Hence, the viscosity is defined as follows

$$\eta = \frac{\sigma}{\dot{\gamma}} + \eta_G, \tag{5.12}$$

where η_G is the glassy contribution to the zero-shear viscosity.

5.2.2 Comparison with the Molecular Dynamics Simulations on Kremer-Grest Unentangled Melts

5.2.2.1 Review the Simulation Data of Kremer-Grest Unentangled Melts

The aim is that of performing Brownian dynamics simulations of Fraenkel chains (coarse-grained at the Kuhn length scale), in order to compare them with the molecular dynamics results of Xu et al.[138] on Kremer-Grest (KG) unentangled melts, as we have already introduced in the last chapter. In particular, we focus on KG chains with $N = 30$ and $N = 50$ beads for which we have equilibrium and steady shear flow results. The approach is based on the assumption that the friction coefficient decreases with increasing flow-induced molecular co-alignment[54, 55].

Let's start from the equilibrium results reported in Table 5.1 of Xu et al.[138], here reproduced for convenience.

Table 5.1: Chain length N, longest relaxation time τ_0, zero shear viscosity η_0, scaling exponent n, critical shear rate $\dot{\gamma}_c$, mean-square radius of gyration $\langle R_{g0}^2 \rangle$ and mean-square end-to-end distance $\langle R_{ete0}^2 \rangle$ at equilibrium for the systems in this work. All quantities are given in standard reduced LJ units.

N	τ_0	η_0	n	$\dot{\gamma}_c$	$\langle R_{g0}^2 \rangle$	$\langle R_{ete0}^2 \rangle$
30	834	20.2	$\cdots$	$\cdots$	7.7	46.3
50	2500	37.9	0.45	0.022	13.4	80.2
100	13513	90.5	0.51	0.015	27.9	168.3
200	86956	417.4	0.60	0.010	56.2	341.8
400	714285	3589.9	0.70	0.003	115.5	686.5

In Table 5.1 we find the following equilibrium properties: the longest relaxation time τ_R (extracted from end-to-end vector autocorrelation), the zero-shear viscosity η_0 (extracted from the low shear rate asymptote of Figure 5.1), and the square average end-to-end chain size $\langle R^2 \rangle$, where all quantities are expressed in Lennard-Jones (LJ) units. We also know the curvilinear length L of the chain, $L = (N-1)l_b$, where $N-1$ is the number of bonds and $l_b = 0.965$ is the bond length. From $\langle R^2 \rangle$ and L we can compute the number N_K of Kuhn segments and the Kuhn segment length l_K by using the following equations: $\langle R^2 \rangle = N_K \cdot l_K^2$ and $L = N_K \cdot l_K$. Then, from τ_R we can extract the Kuhn segment friction ζ by using the well-known formula for the Rouse time. Once we have N_K, l_K and ζ we can perform equilibrium simulations and compare results with those reported in Table 5.1. Details are reported below for $N = 30$ and $N = 50$.

Let's start from the equilibrium dynamics of the $N = 30$ KG melts. From Table 5.1 we know that $\langle R^2 \rangle = 46.3$. On the other hand, the length L of the chain is $L = 29 \cdot 0.965 = 28$. Hence $l_K = \langle R^2 \rangle / L = 1.65$, a value slightly smaller than indicated by Figure 2 of Svaneborg and Everaers (2020)[125] (1.68 and 1.74 for $N = 20$ and $N = 40$, respectively). There follows that $N_K = \langle R^2 \rangle / (l_K^2) = 16.9 \approx 17$. Fraenkel chain simulations with $N_K = 17$ give $\langle R^2 \rangle = 46.6$.

Concerning dynamic properties, from Table 5.1 of Xu et al.[138] we know that the longest relaxation (Rouse) time is $\tau_R = 834$. The formula for τ_R is $\tau_R = (\zeta l_K^2)/(12 k_B T \sin^2[\pi/2(N_K + 1)])$, from which we get $\zeta = 27.9$. This value is consistent with that reported in Figure 6(a) of Svaneborg and Everaers (2020)[125], which is $\zeta = \zeta_{CM}/N_K = 441.6/17 = 26.0$. We have run Fraenkel chain simulations with such a value of ζ, giving a longest relaxation time of 848. Hence the true value of ζ is $\zeta = 27.9 \cdot 834/848 \approx 27$.

The same Fraenkel chain simulation gives $\eta_0 = 19$. By correcting for the slightly smaller value of the longest relaxation time, we obtain $\eta_0 = 18.5$, which is compatible with the value reported by Xu et al.[138], $\eta_0 = 21.2$. The difference $21.2 - 18.5 = 2.7$ gives an estimate of the glassy contribution to the zero-shear viscosity, which is not accounted for in our Fraenkel chain simulations.

Let's then move to the equilibrium dynamics of the $N = 50$ KG melts. From Table 5.1 of Xu et al.[138], we know that $\langle R^2 \rangle = 80.2$. On the other hand, the length L of the chain is $L = 49 \cdot 0.965 = 47.3$. Hence $l_K = \langle R^2 \rangle / L = 1.70$, a value slightly smaller than indicated by Figure 2 of Svaneborg and Everaers (2020)[125] (1.74 for $N = 40$). There follows that $N_K = \langle R^2 \rangle / (l_K^2) = 27.8 \approx 28$. Fraenkel chain simulations with $N_K = 28$ give $\langle R^2 \rangle = 81.1$.

Concerning dynamic properties, from Table 5.1 of Xu et al.[138] we know that the longest relaxation (Rouse) time is $\tau_R = 2500$. Now, since τ_R is $\tau_R = (\zeta l_K^2)/(12 k_B T \sin^2[\pi/2(N_K + 1)])$, we get $\zeta = 30.4$. This value is consistent with that reported in Figure 6(a) of Svaneborg and Everaers (2020)[125], which is $\zeta = \zeta_C M/N_K = 878/28 = 31.4$. We have then run Fraenkel chain simulations with such a value of ζ, giving a longest relaxation time of 2520. Hence the true value of ζ is $\zeta = 30.4 \cdot 2500/2520 \approx 30$.

The same Fraenkel chain simulation gives $\eta_0 = 33.7$. By correcting for the slightly smaller value of the longest relaxation time, we obtain $\eta_0 = 33.7 \cdot 0.99 = 33.4$, which is compatible with the value reported by Xu et al.[138], $\eta_0 = 37.9$. The difference $37.9 - 33.4 = 4.5$ gives an estimate of the glassy contribution to the zero-shear viscosity.

Hence, we take an average of the estimates, giving $\eta_G = 3.6$. This value is particularly important for the comparison with steady shear data to be discussed below.

Now the aim is fitting the viscosity data reported in Figure 5.1 of Xu et al.[138], reproduced here for convenience.

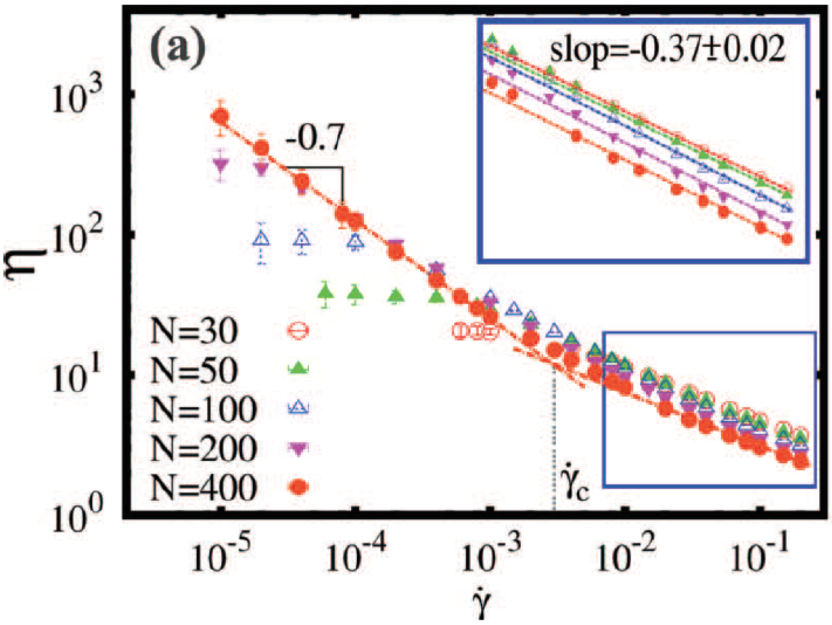

Figure 5.1: First normal stress difference N_1 - Scaled first normal stress difference N_1 as a function of shear rate. The dashed line indicates quadratic behavior for $\dot{\gamma} < \tau_0^{-1}$.

Figure 5.2 shows that Fraenkel chain simulations with the equilibrium friction generate a modest shear thinning, incompatible with data. The only way to improve predictions is by reducing the friction coefficient, more and more significantly with increasing values of the shear rate.

In order to fit the data in Figure 5.1 we developed a code that, with a trial-and-error procedure, determines the best fit value of the friction coefficient for each shear rate. In this section, the beads are endowed with isotropic friction. Figure 5.3 shows the bead friction under steady flow normalized with the equilibrium friction as a function

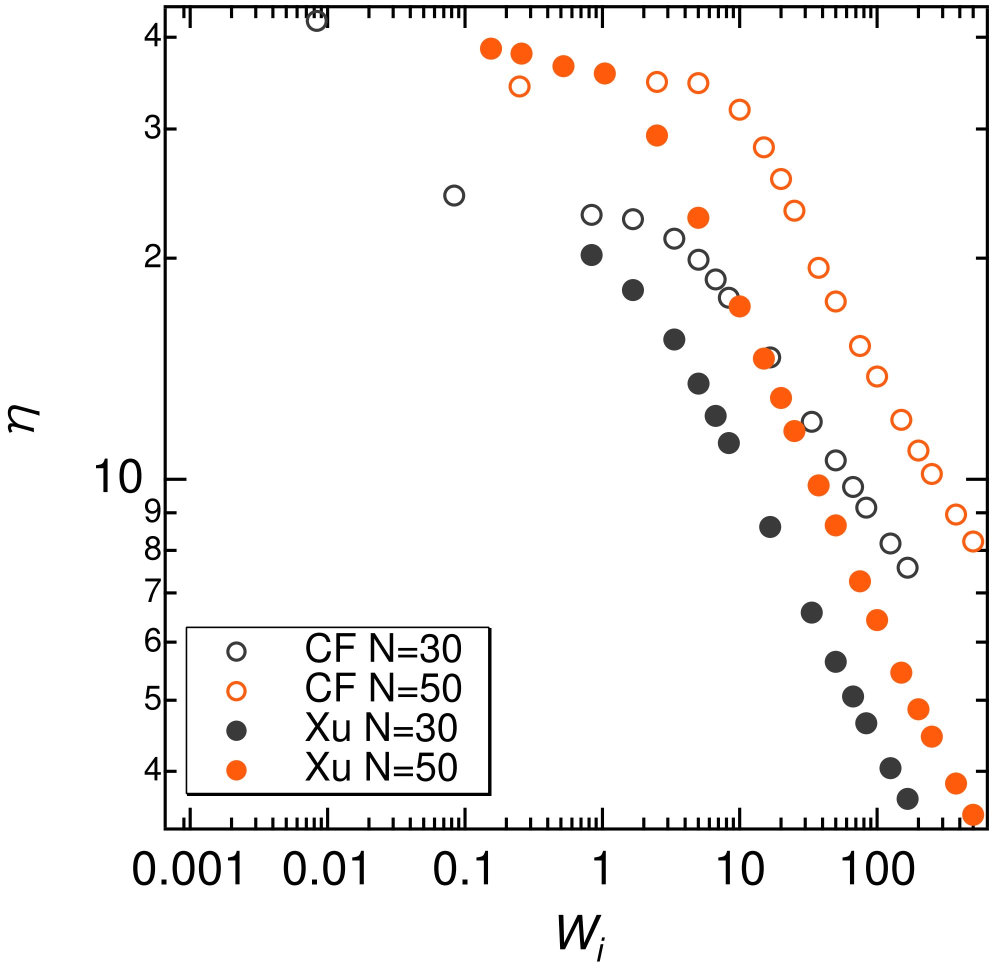

Figure 5.2: Steady-state shear viscosity as a function of Weissenberg number - Comaprisons between the data from Xu et al.[138] and the Fraenkel chain predictions with equilibrium friction. Hereinafter, "CF" indicates "constant friction" and "Xu" refers to the data from Xu et al.[138].

of Weissenberg number. We can easily find that at shear rates larger than $\dot{\gamma}_c$ data can be fitted with a shear-rate independent friction coefficient, about one third the equilibrium value.

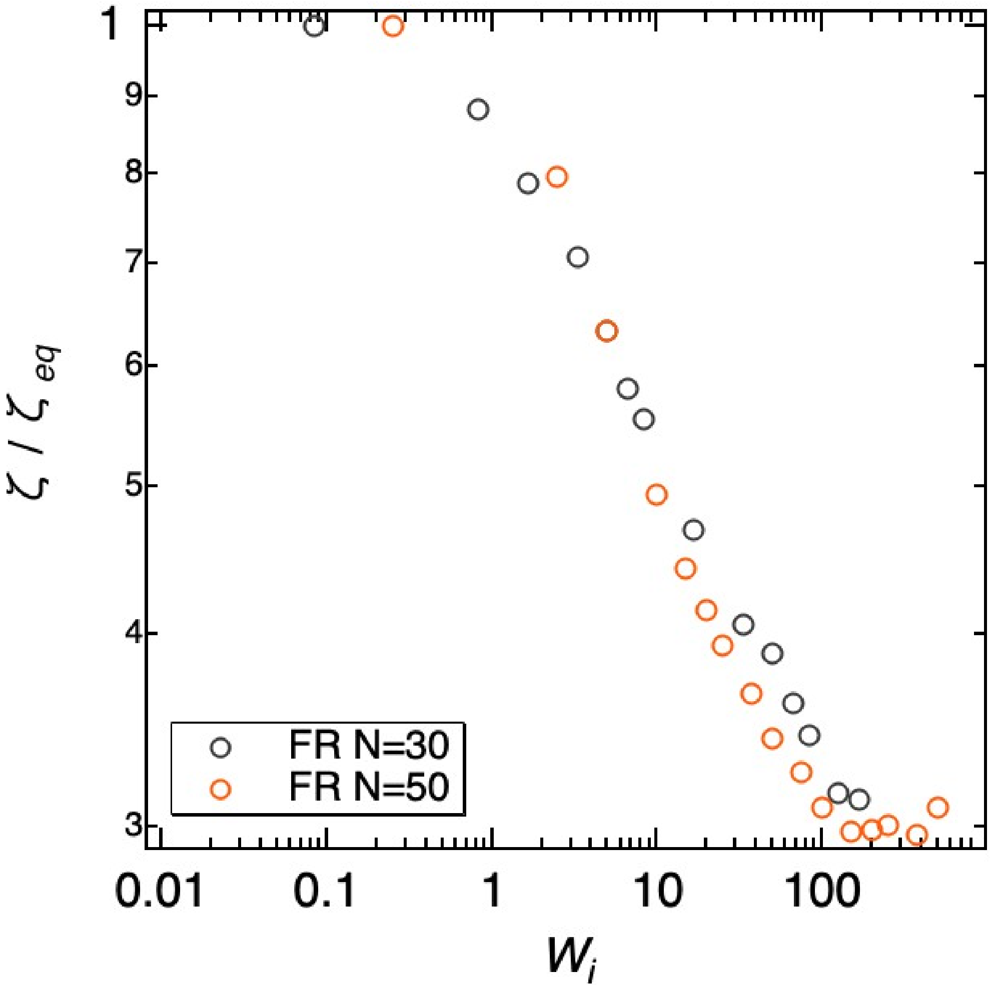

Figure 5.3: Normalized friction coefficient with equilibrium friction as a function of Weissenberg number - At $W_i > 100$, friction coefficient is about one third the equilibrium value.

Figure 5.3 also indicates that the steady-state normalized friction is not sensitive to chain length, at least for the length within an unentangled regime (the good agreement between $N = 30$ and $N = 50$). The agreement is explainable from a chemical point of view. As mentioned in the last Chapter, ζ-reduction is a local phenomenon. Hence, the friction magnitude relies on the chemical structure of the monomeric segments. In other words, the chain length would not affect the magnitude (within the unentangled regime. For the entangled polymer melts, the effect of ζ-reduction on the viscoelastic response is mixed with the effects of nonlinear mechanisms of entanglement relaxation; it is not so straightforward to extract just the former effect from those responses). In addition, at low enough shear rates ($\dot{\gamma} < 0.2$), the friction remains near a constant, which means that the energy-dissipating motion of monomeric segments, driven by molecular interaction, is so slow that the arrangement of chains almost remains unchanged. In contrast, at high shear rates, the friction plummets. It implies that monomeric segment motion becomes faster and that the relative orientation of surrounding segments is changed. Finally, all segments are oriented in the same direction and the motion arrives at the ultimate speed.

After fitting the data in Figure 5.1, the challenge is looking at all other observables reported by Xu et al.[138].

5.2.2.2 Structural Properties

The end-to-end tensor $\mathbb{R}$ and the gyration tensor $\mathbb{G}$ are the most common quantitative variables of the conformational properties of a polymer chain under flows, which are defined as follows

$$\mathbb{R} = (\mathbf{R}_N - \mathbf{R}_1)(\mathbf{R}_N - \mathbf{R}_1) \tag{5.13}$$

$$\mathbb{G} = \frac{1}{N}\sum_{i=1}^{N} \mathbf{R}_{cm}\mathbf{R}_{cm}, \tag{5.14}$$

where $\mathbf{R}_{cm}$ is the vector between i-th monomer and the center of mass of the polymer. On the basis of the definition of $\mathbb{R}$ and $\mathbb{G}$, we mark their trace as the mean-square end-to-end distance $\langle R_{ete}^2\rangle$ and the mean-square radius of gyration $\langle R_g^2\rangle$ respectively, i.e. $\langle R_{ete}^2\rangle = \mathrm{Tr}\langle\mathbb{R}\rangle$ and $\langle R_g^2\rangle = \mathrm{Tr}\langle\mathbb{G}\rangle$.

Figure 5.4, and Figure 5.5 display simulation results for the mean-square chain radius of gyration normalized with the quadratic curvilinear length $\langle R_g^2\rangle/L^2$ and the nomarlized root-mean-square chain end-to-end distance $\langle R_{ete}\rangle/L$ as a function of Weissenberg number in dimensionless units, respectively. The comparisons among the constant friction ("CF") case , the friction reduction ("FR") case, and the data of Xu et al. [138] are made in both Figures as well. At low enough shear rates ($\dot{\gamma} < 2$), the two quantities remain practically unaffected by the applied flow, indicating that in this range of shear rates the flow causes mainly orientation (and not distortion) of the chains along the flow direction. At higher shear rates, on the other hand, the values of $\langle R_g^2 \rangle / L^2$ and $\langle R_{ete} \rangle / L$ increase rapidly with the applied flow; this indicates that for these intermediate flows, polymermolecules are not only aligned along the flow direction but assume also a stretched conformation. This is accompanied by effects such as: (a) significant energetic and entropic contributions to the free energy of the system, (b) development of significant lateral enthalpic interactions between neighboring chains, and (c) development of an anisotropic chain diffusivity tensor, which are all features of the nonlinear viscoelastic response of the melt to the applied flow. At high shear rates, the increase in the chain dimensions gradually slows down, leading eventually to a plateau. Comparing with the data of Xu et al. [138], the simulation results of both "FR" and "CR" are able to qualitatively capture the features of the chain radius of gyration $\langle R_g^2 \rangle / L^2$ as well as the features of chain end-to-end distance. However, at high shear rates, even though both "CF" and "FR" deviate from the data, "FR" alleviates the derivation to a great extent. The discrepancies happened in the friction reduction model is probably caused by the fact that the beads are endowed with isotropic fraction.

In the next section, we proposed that the bead friction is anisotropic in view that the diffusivity tensor is anisotropic.

Figures 5.6, 5.7 show the friciton reduction results for the probability distribution function with respect to the magnitude $|R_{ete}|/L$ of the normalized chain end-to-end vector for a number of shear rates in the interval $0.001 \leq \dot{\gamma} \leq 0.2$ covering both linear and nonlinear flow fields. At equilibrium the distribution is Gaussian, in accordance with theoretical predictions for long enough chains. The distribution remains essentially Gaussian even when a flow is applied as long as the dimensionless shear rate is approximately less than 0.01 (although a small shift of the entire curve to larger $|R_{ete}|/L$ values is clearly discernible in the curves of Figures 5.6 and 5.7). For higher shear rates (e.g., for $W_i \approx 10$, $\dot{\gamma} = 0.01$ in Figure 5.6 ($W_i = 8.34$) and $\dot{\gamma} = 0.006$ in Figure 5.7 ($W_i = 15$)) the distribution deviates significantly from the Gaussian one, which is consistent with the simulation reports for shorter (i.e., unentangled) PE melts[8, 64]. For example, despite the fact that it is still dominated by a single peak, it is centered asymmetrically around its average value (more precisely, it is broadened on its left). At even higher shear rates (e.g., for $\dot{\gamma} = 0.1, 0.15$, and 0.2 in Figures 5.6 and 5.7), the distribution becomes very flat in its intermediate region (its width grows considerably);

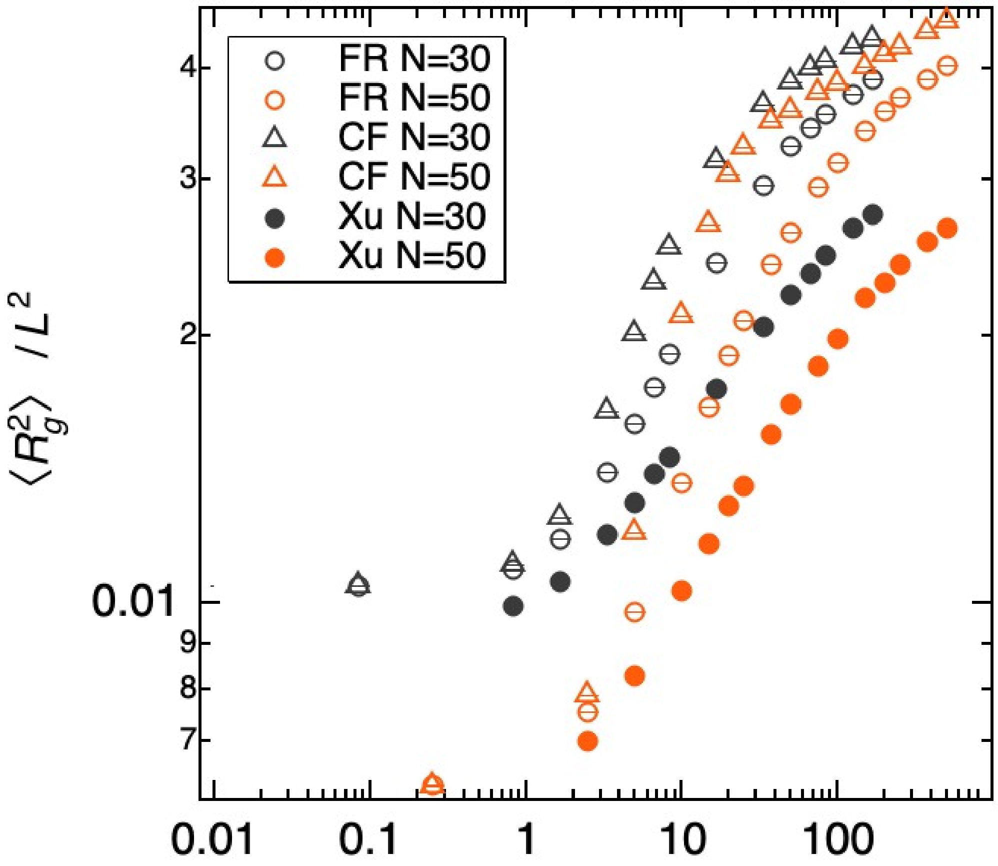

Figure 5.4: Normalized mean-square chain radius of gyration $\langle R_g^2 \rangle / L^2$ - When $W_i > 3$, the chain radius of gyration increases rapidly first and then approaches to a constant.

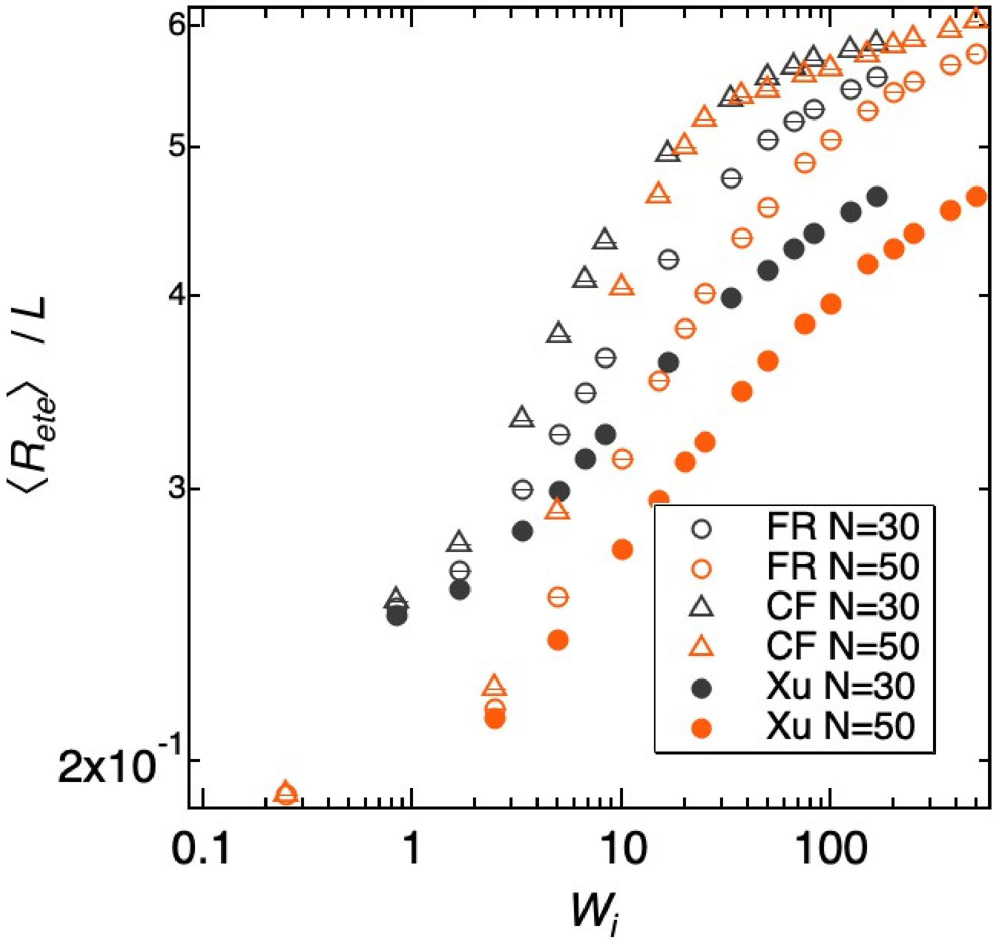

Figure 5.5: Normalized root-mean-square chain end-to-end distance $\langle R_{ete}\rangle/L$ - The values of the end-to-end distance show a similar trend as the value of the chain radius of gyration.

it also shows a tendency to develop two peaks, one at small and one at large $|R_{ete}|/L$ values. This phenomenon is due to chain rotation and tumbling under shear:[4, 8, 64] the increase in the shear rate enhances the rotational frequency of the molecule (its vorticity), thus also the number of lateral collisions with neighboring chains; consequently the polymer tumbles quickly, since it finds itself more and more often in an unstable orientation relative to the direction of the applied flow. The net result is a chain whose conformation alternates quickly between stretched and collapsed structures, and this explains the broadening of the distribution function for $|R_{ete}|$ as well as the appearance of the two peaks (instead of one at low shear rates)[4, 8, 29, 39, 64]. The comparisons of the distribution of $|R_{ete}|$ among FR, CR and Xu (data) for $N = 30$ at $\dot{\gamma} = 0.2$ is plotted in Figure 5.8. For low $|R_{ete}|$ ($|R_{ete}|/L < 0.2$), the distribution are almost the same for all cases, yet the predictions of both FR and CF models depart from the data when $|R_{ete}|$ becomes larger even though the former two results overlap with each other. The consistency of the results between FR and CR implies that the friction reduction is not caused by the stretching of chains but by the orientation of chains.

Figures 5.9, 5.10, and 5.11 reports results for the variation of the three nonzero components of the radius gyration tensor ($\langle G_{xx}\rangle$, $\langle G_{yy}\rangle$, and $\langle G_{zz}\rangle$) with W_i. Figures 5.12 and 5.13 shows the combined results for the variation of those components of the radius gyration tensor with W_i, in the cases of $N = 30$ and $N = 50$, respectively. The curves obtained are very similar to those already reported in the literature for a number of shorter PE melts from direct NEMD or hybrid GENERIC Monte Carlo/NEMD simulations with a similar atomistic model[8]. More specifically, $\langle G_{xx}\rangle$ remains practically constant (close to unity of the equilibrium condition) at low shear rates corresponding to rather weak flows ($W_i < 2$), for larger shear rates (corresponding to Weissenberg numbers in the interval $2 < Wi < 30$) it increases rapidly, while for even higher shear rates ($W_i > 30$) it reaches an asymptote. The overall behavior appears to be quite similar to $\langle R_g^2\rangle/L^2$ shown in Figure 5.4, as $\langle G_{xx}\rangle$ dominates over the other components at high shear rates (c.f. Figures 5.12 and 5.13), As closely related to Figure 5.4, the asymptotic behavior of $\langle G_{xx}\rangle$ is ascribed to (a) finite chain extensibility due to local bond-stretching and bond-bending interactions, and (b) chain rotation and tumbling under shear flow, which lower the average chain dimension significantly below its maximum value and prevent perfect alignment of chains to the flow (x-) direction;50 this can also be interpreted as an asymptotic behavior of the persistence length l_K at high

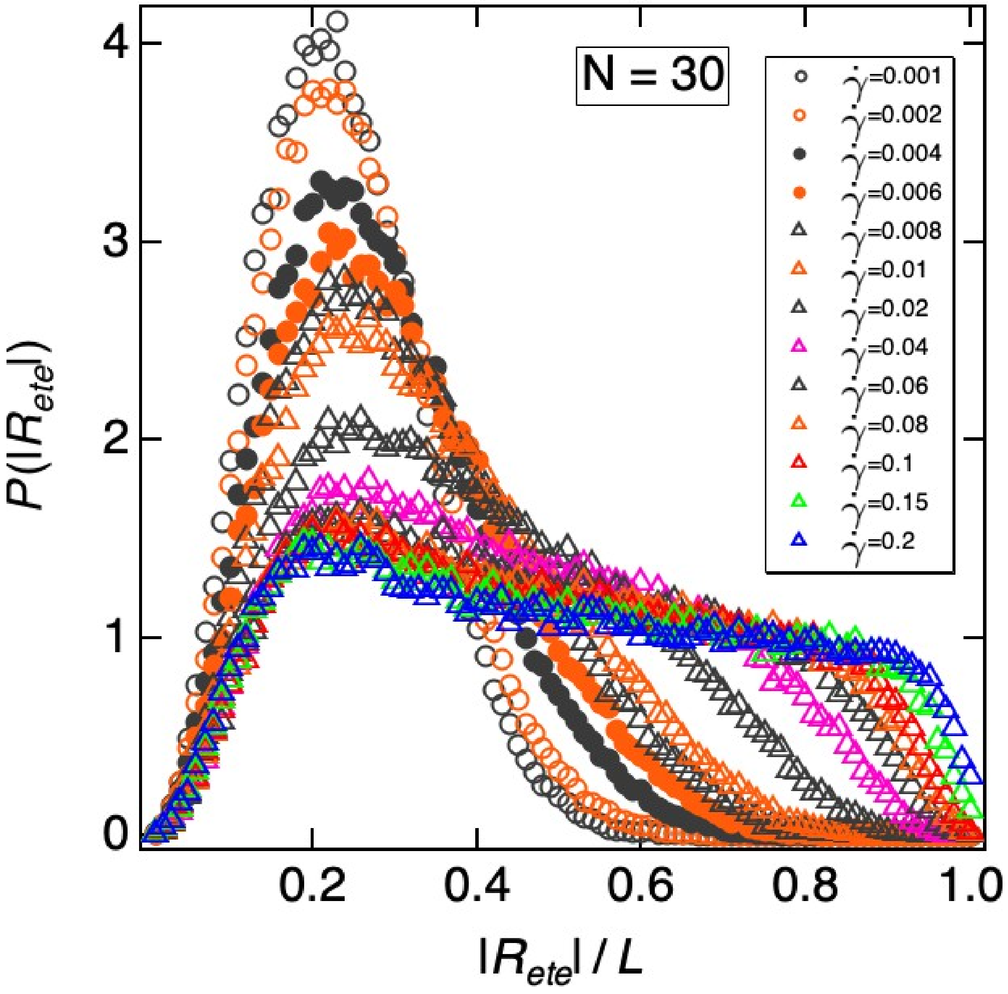

Figure 5.6: Variation of the probability distribution function $P(|R_{ete}|)$ regarding the normalized chain end-to-end distance $|R_{ete}|/L$ with shear rate - $N = 30$

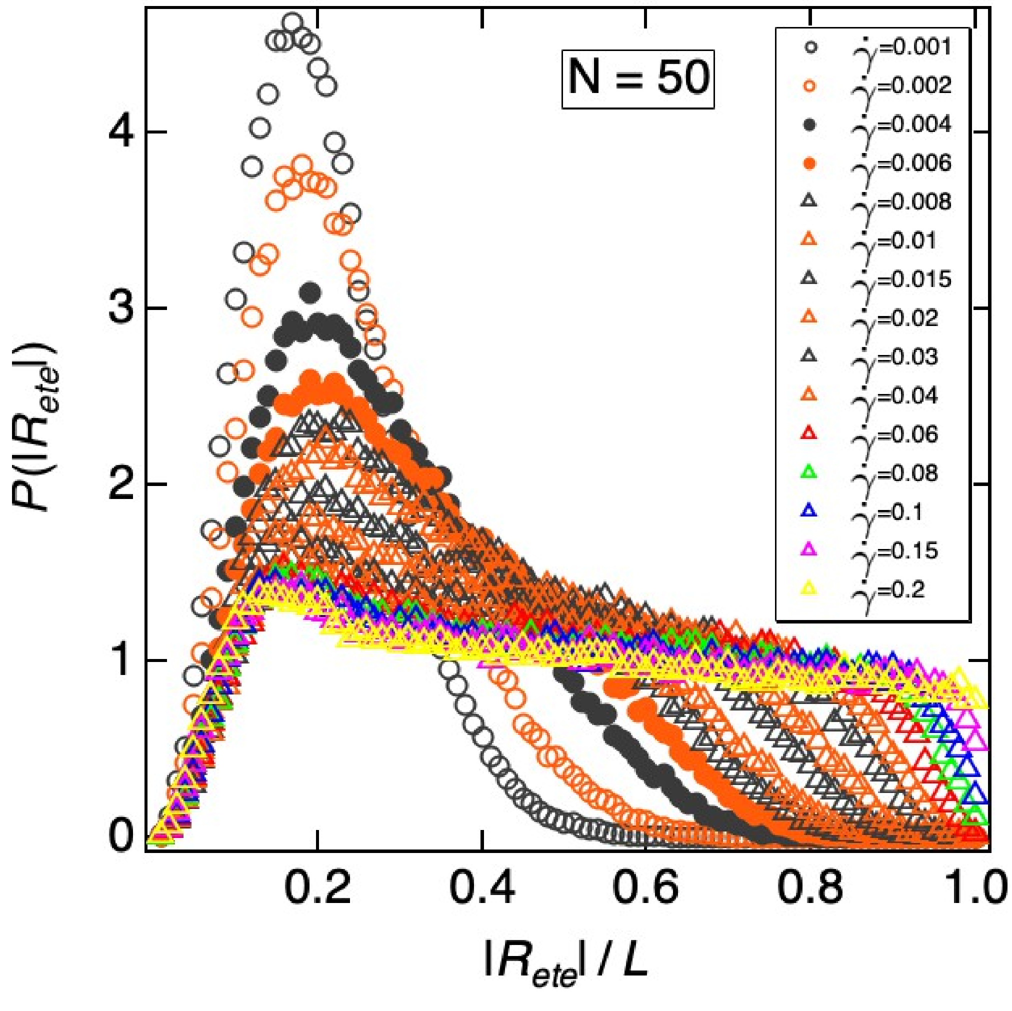

Figure 5.7: Variation of the probability distribution function $|R_{ete}|$ regarding the normalized chain end-to-end distance $|R_{ete}|/L$ with shear rate - $N = 50$

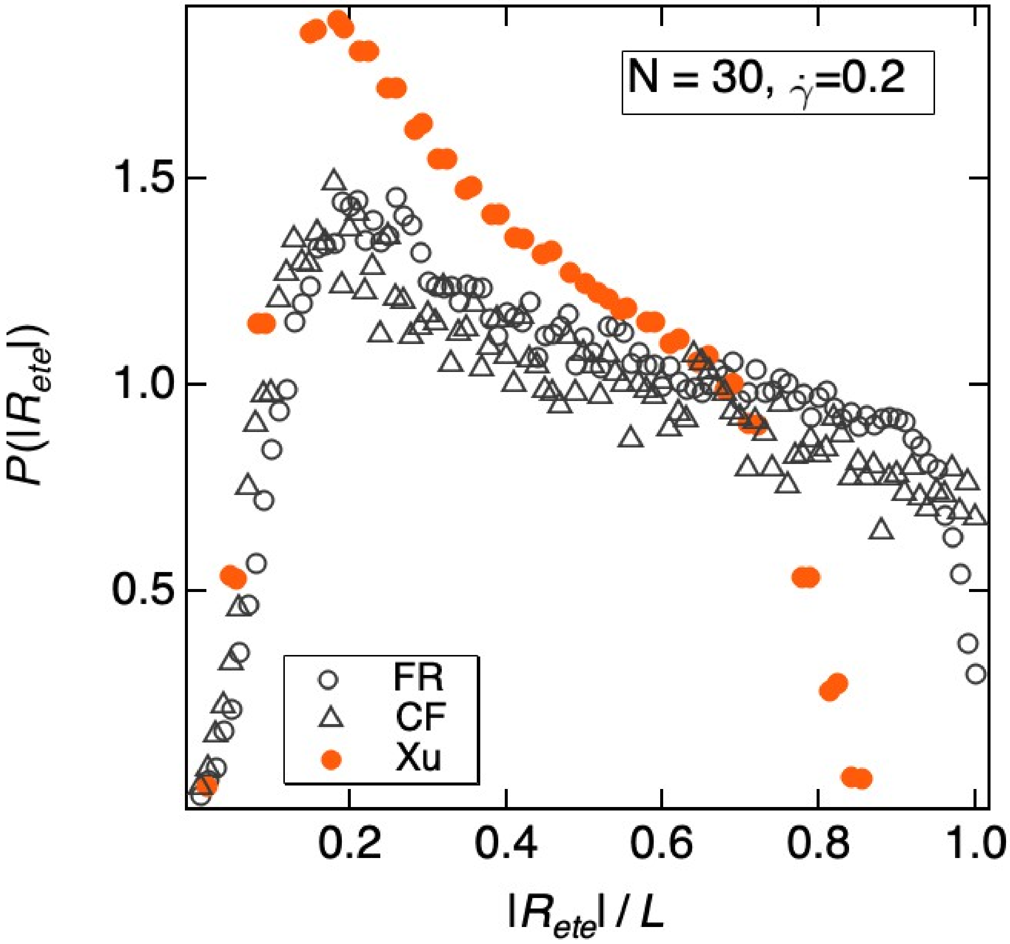

Figure 5.8: Comparisons of the probability distribution function $P(|R_{ete}|)$ regarding the normalized chain end-to-end distance $|R_{ete}|/L$ among FR, CF and Xu - $N = 30, \dot{\gamma} = 0.2$

shear rates, as described earlier. Qualitatively similar behavior has also been observed in unentangled polyethylene38 and polystyrene50 melts under shear. Likewise, FR results reduce the gap between CF results and the data. The asymptotic behavior shown by FR and CR at high shear rates is probably induced by the persistence length l_K.

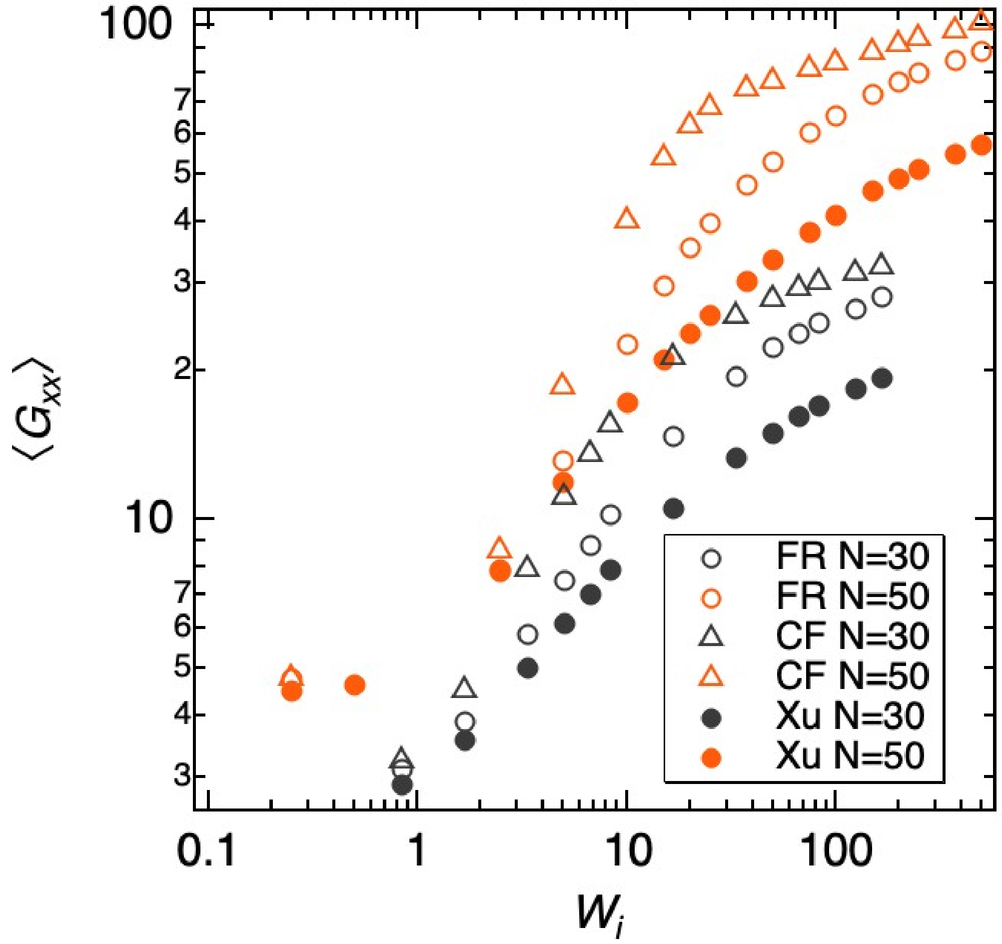

Figure 5.9: Variation of the radius gyration tensor component $\langle G_{xx} \rangle$ with W_i. - The FR results narrow the deviation from the data, comparing with CF results when $W_i > 3$.

In contrast to $\langle G_{xx} \rangle$, $\langle G_{yy} \rangle$, and $\langle G_{zz} \rangle$ are found to decrease monotonically with the applied flow, which is physically reasonable given that their behavior is governed solely by the degree of chain orientation and alignment with the flow. Furthermore, $\langle G_{zz} \rangle$ decreases more slowly than $\langle G_{yy} \rangle$, which should have been expected given that the y-axis is the velocity gradient and the z-axis is the neutral direction.

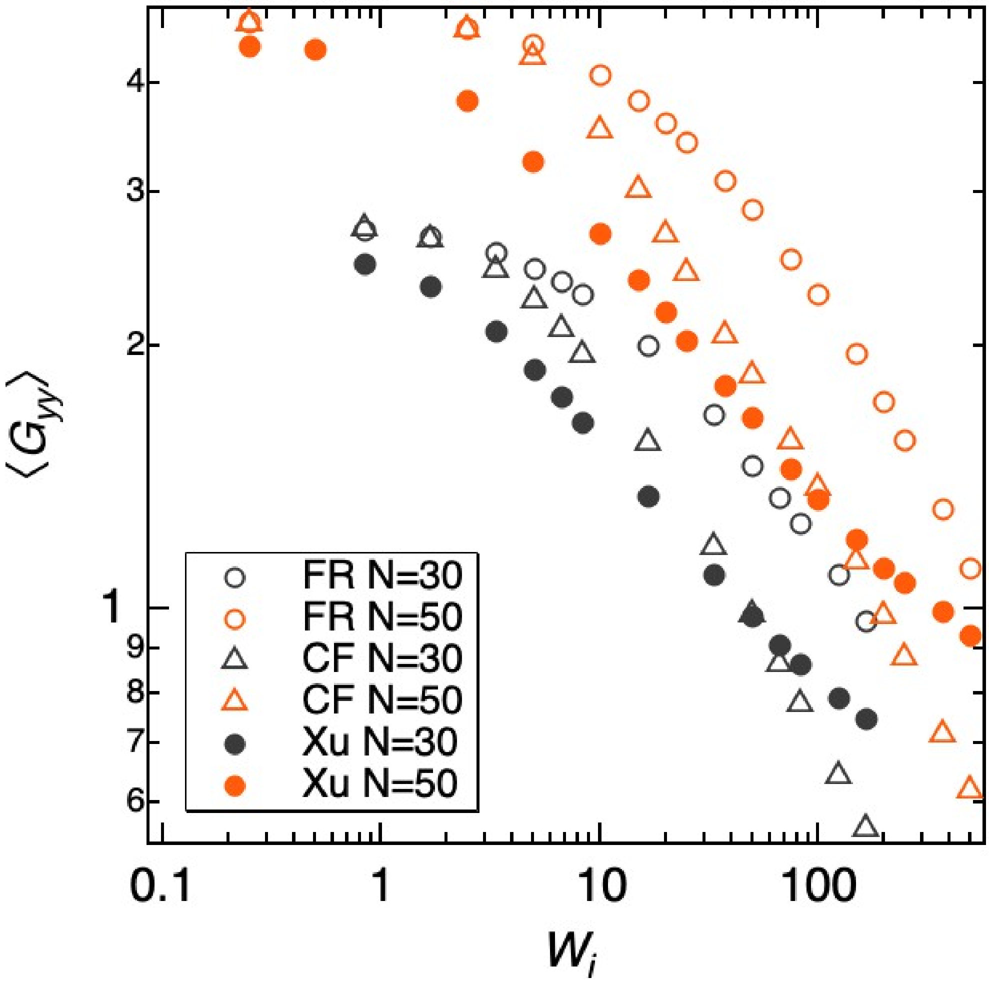

Figure 5.10: Variation of the radius gyration tensor component $\langle G_{yy} \rangle$ with W_i. - The fact that CF results show smaller values at high shear rates ($W_i > 10$) implies that the chain conformation is more flat when the equilibrium friction is adopted in the steady shear flow.

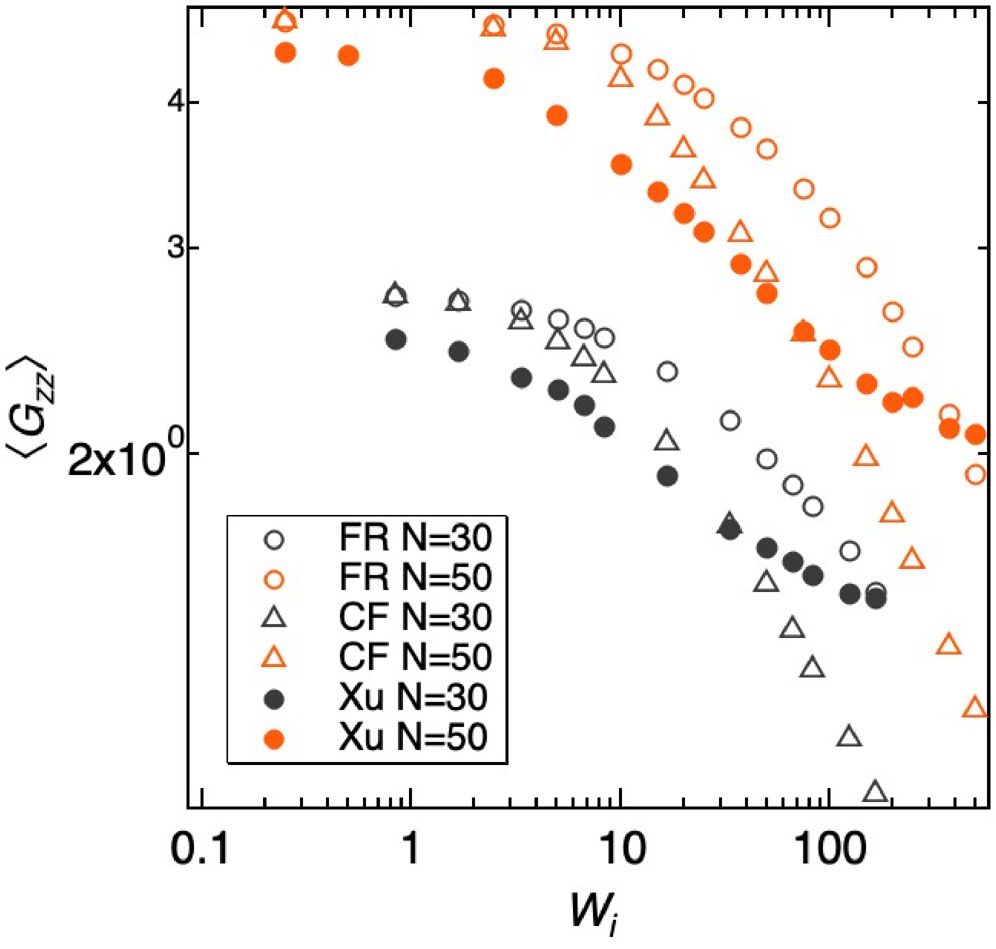

Figure 5.11: Variation of the radius gyration tensor component $\langle G_{zz} \rangle$ with W_i. - Even though the FR results deviate from the data at the intermediate shear rates, they are approaching to the data along with shear rates increasing($W_i > 10$.)

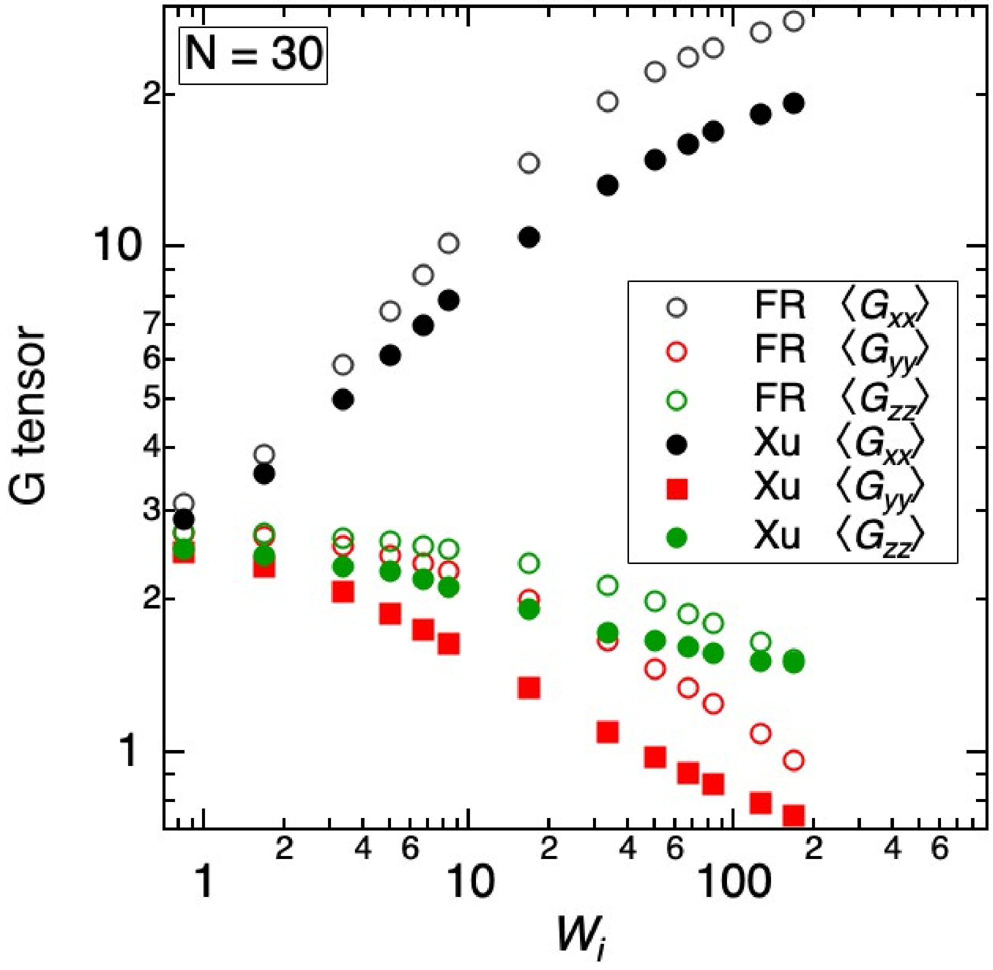

Figure 5.12: The combined results for the three components of the tensor $\mathbb{G}$ as a function of W_i - $N = 30$

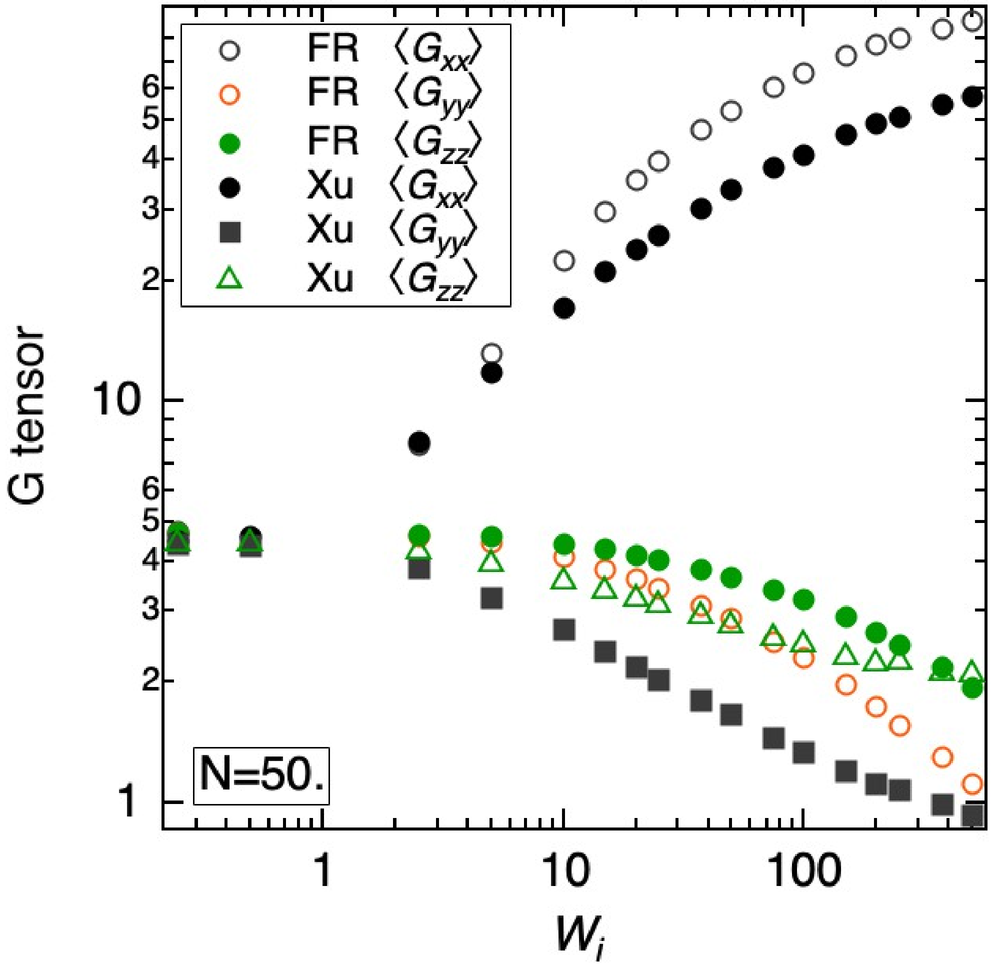

Figure 5.13: The combined results for the three components of the tensor $\mathbb{G}$ as a function of W_i - $N = 50$

In both Figures 5.10 and 5.11, CF results show smaller values at high shear rates ($W_i > 10$), which indicates that the chain conformation is more flat along y-axis and z-axis. These predictions are acceptable since at high shear rates, chains with larger friction (compared with the friction reduction model) are less movable, driven by shear flow, along y-axis and z-axis.

Given that the conformation tensor is one of the most favorite primary state variables for the formulation of differential constitutive models[12, 105], the results presented here for its variation with the applied flow can be important not only in getting a deeper understanding of the interplay between flow and molecular-level characteristics of polymer melts but also in developing more accurate rheological models 79-81,36,82,83 and, more importantly, in designing more versatile multiscale simulation methodologies[7, 8, 57, 96, 110].

The degree of chain alignment/orientation can be characterized by the angle ϕ, which is the angle between the projection of the eigenvector of the gyration tensor with the largest eigenvalue onto the flow-gradient plane and the flow direction. It can be extracted straightforwardly from the simulation data through

$$\tan(2\phi) = 2\langle G_{xy}\rangle/(\langle G_{xx}\rangle - \langle G_{yy}\rangle) = m_G/\dot{\gamma}, \tag{5.15}$$

where the right-hand side of the equation defines the orientation resistance parameter m_G.

Figure 5.14 displays the comparisons of the scaled orientation resistance parameter among FR, CF, and the data as a function of W_i. In the Newtonian regime ($W_i < 2$), m_G is found independent of shear rate, consistent with the results for polymers in dilute solution under shear[6, 9, 66]. With the increase of shear rates, the orientational resistance deviates from a plateau value and can be described by a universal power law for various chain lengths. The exponent is about 0.75.

The FR results have a good agreement with the data regarding the orientation resistance parameter. However, the magnitude of the CF predictions is less than that of the data when $W_i > 2$. These facts provide solid evidence for the assumption that the physical phenomenon of friction reduction is related to the orientation of polymer chains.

Further insight into the orientational behavior of polymer chains is gained by the orientation parameter S, which is defined in eq (5.5). Figure 5.15 shows the comparisons of the order parameter between FR and CF with two different chain lengths as a function of W_i. Clearly, the degree to which chains get ordered along the flow direction increases with increasing shear rate, approaching a plateau (0.6) at high enough fields where approximately $\sim$ 60% of the chains (on the average) is supposed to be aligned along the flow direction. On the other hand, at low shear rates ($W_i < 0.1$), chains should be neither stretched nor elongated in any preferred direction although a nonzero xy-component should be present.

The difference between FR and CF results shows the effects of the friction reduction on the chain alignment. The smaller magnitude of the FR results imply that the chains are less aligned along the flow direction in the FR model than that in the CF model, which is consistent with the results of the orientation gyration tensor as well as with the results of the resistance parameter (c.f. Figures 5.10, 5.11 and 5.14).

5.2.2.3 Viscometric Functions

In Figures 5.16, 5.17, and 5.18 we present the predictions of our FENE simulations for the material functions of the simulated Kremer & Grest (KG) melt, namely the first normal stress coefficient Ψ_1, the second normal stress N_2, and the ratio $-\Psi_2/\Psi_1$. The results have been obtained by using the given expression in eqs (4.1), (4.2), and (4.3) for the stress tensor $\boldsymbol{\sigma}$ based on the well-known Irving-Kirkwood statistical-mechanical formula.

In an incompressible material, normal stresses are themselves of no rheological significance, because if they are equal in all directions they cause no deformation. However, differences between normal stress components are significant, because they cause deformation. Figures 5.16 and 5.17 show our simulation results for the first normal stress coefficient and the second normal stress difference Ψ_1 and N_2 as a function of dimensionless shear rate. Consistent with experimental observations,2 both exhibit a large shear thinning behavior which is captured quite well by power-law expressions. Figure 5.18 reports the ratio $-\Psi_2/\Psi_1$, we see that the value of the ratio lies within the range [0.0001,0.01].

In Figure 5.16, the FR results show a better agreement with the data than the CF predictions.

The second normal stress difference N_2 is the most difficult to measure of the three viscometric functions, not only by experiments but also by the simulations. Olson et

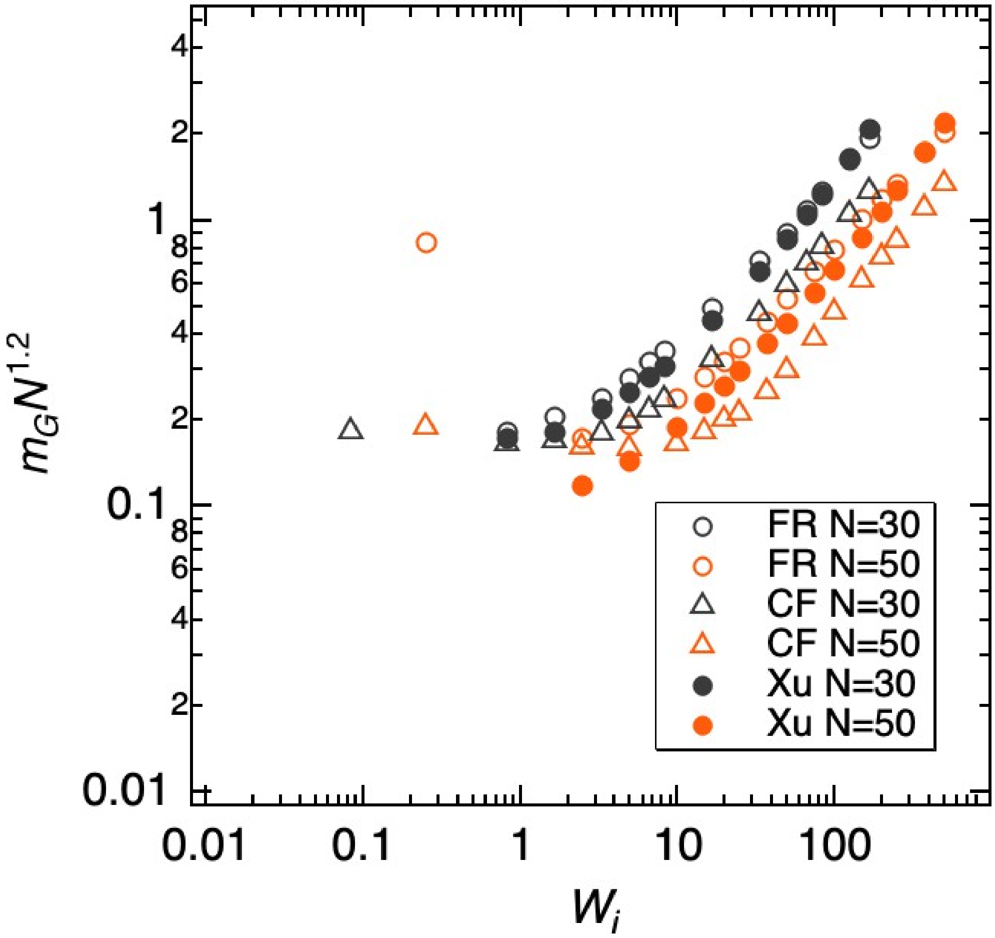

Figure 5.14: Scaled orientation resistance parameter m_G as a function of W_i. - The resistance parameter exhibits a power-law dependence on shear rate with an exponent of about 0.75.

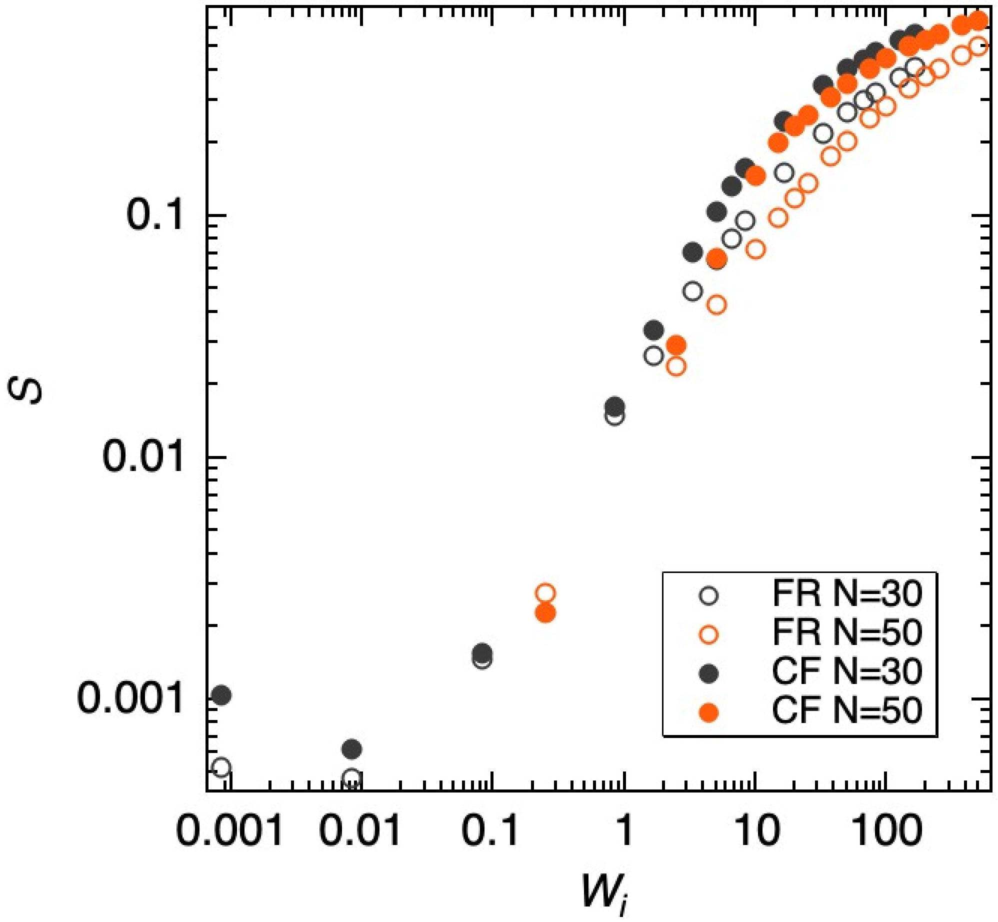

Figure 5.15: Order parameter S as a function of W_i - The mismatch of the results between FR and CR indicates that the friction reduction is related to the conformation of chains.

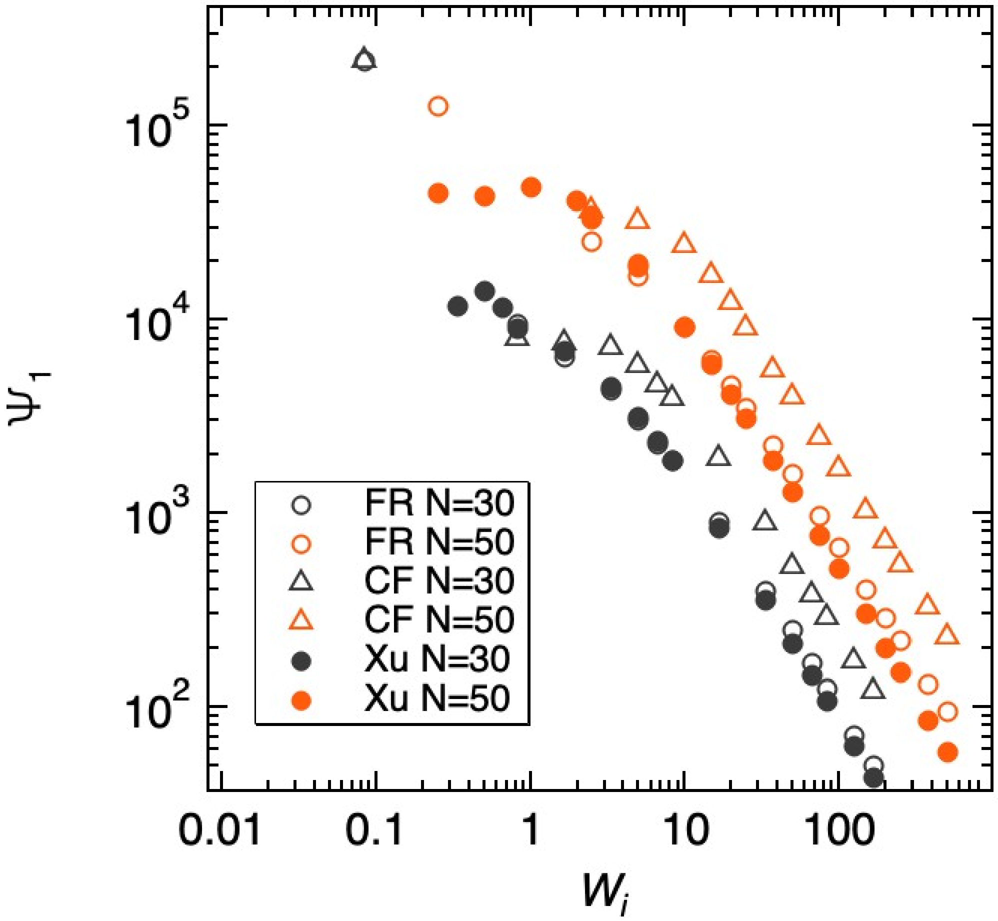

Figure 5.16: FENE simulation predictions for the steady-state viscoelastic material functions of the simulated KG melt - The first normal stress coefficient

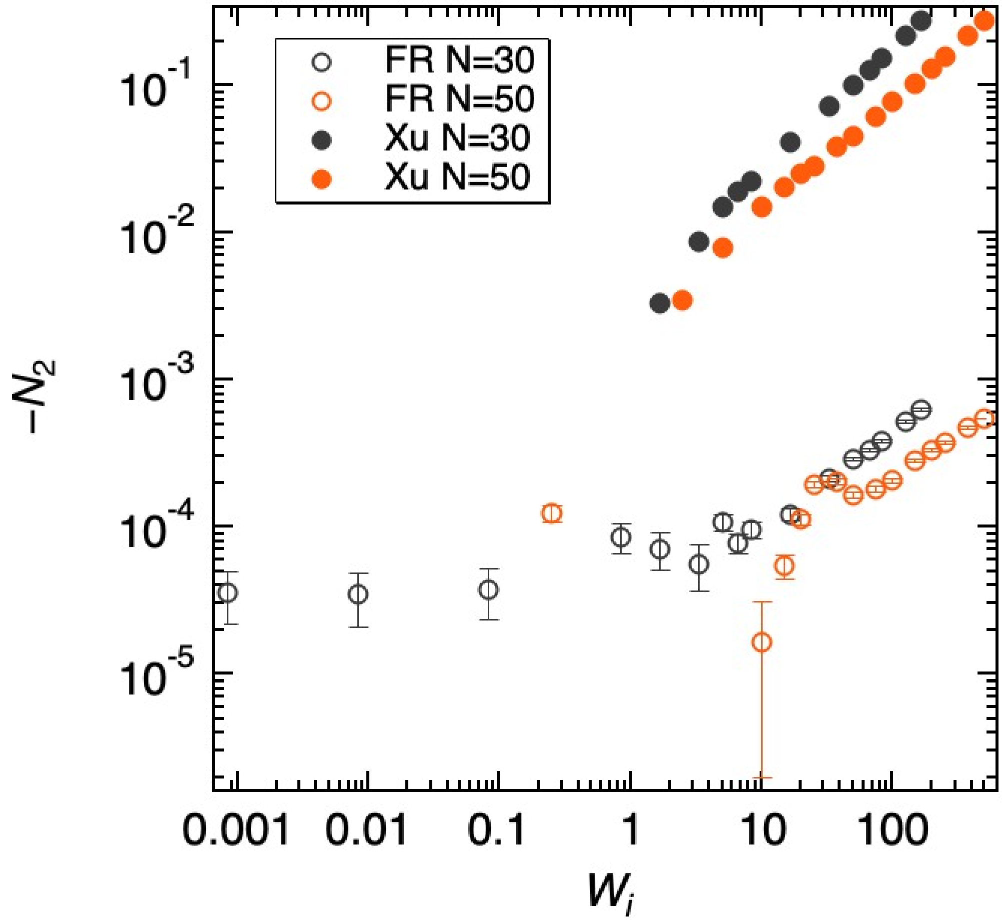

Figure 5.17: FENE simulation predictions for the steady-state viscoelastic material functions of the simulated KG melt - The second normal stress difference

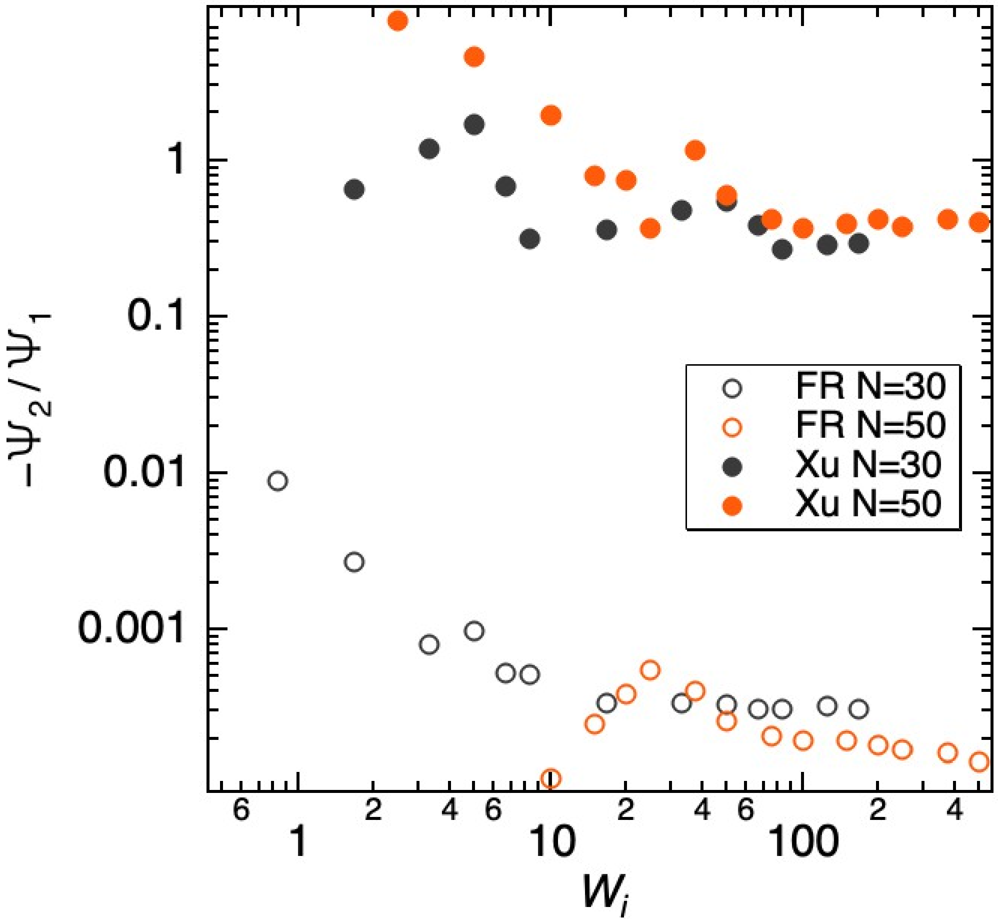

Figure 5.18: FENE simulation predictions for the steady-state viscoelastic material functions of the simulated KG melt - the ratio $-\Psi_2/\Psi_1$ of the second to the first normal stress coefficient

al. [95] measured the second normal stress difference using beams inclined at several angles to find the components of the refractive index tensor. To determine transient normal stress difference, the phase-modulated polarization technique was developed by Frattini and Fuller [37]. Kalogrianitis and van Egmond [63] used this technique to determine the shear stress and both normal stress differences as functions of time in the start-up of steady simple shear. Optical techniques are particularly attractive for measurements of normal stress differences, since such methods do not require the use of a mechanical transducer that is subject to compliance error.

A non-zero N_2 is obtained in our simulation, even though the values are smaller than the data. It should be noticed that in the last Chapter, the value of N_2 reported by Watanabe's recipe is zero due to the pre averaging assumption used in their model. Here, we take the topological effects into account so that we obtain the non-zero N_2. We are supposed to use the beads endowed with anisotropic friction model in the next section to improve the results.

Schweizer[111] reported a technique that a cone angle of 0.148 rad minimized instrument compliance while generating a nearly homogeneous strain. Schweizer[111] used this technique to study a polystyrene melt and found that the normal stress ratio $-\Psi_2/\Psi_1$ was 0.24 at a shear rate of $0.1s^1$ and decreased to 0.05 at $30s1$. Schweizer et al. [113] used the cone/partitioned plate method to obtain transient normal stress data for a polystyrene melt and reported that axial compliance and the normal force range caused problems. Schwiezer and Schmidheiny [112] added a third plate partition (CPP3) to suppress edge effects, and this improved the accuracy of the steady state value of N_2, but it was not suitable for use with melts because of rheometer frame compliance. The FR results shown in the Figure 5.18 qualitatively capture the experimental characterization described above, even though there are discrepancies between the FE results and the data.

5.3 Beads Endowed with Anisotropic Friction

5.3.1 Theory

As mentioned in the Introduction, we want to account for a bland topological interaction with the surrounding chains. Since at each time t the chain is seen as an ellipsoid, we will assume that the chain diffuses preferentially along the major axis of such ellipsoid, i.e., diffusion in the orthogonal direction is somewhat restricted. The chain model considered here is therefore endowed with a time-dependent anisotropic diffusion coefficient $\boldsymbol{D}$ and mobility $\boldsymbol{\mu}$ of the beads given by:

$$\boldsymbol{D}(t) = D[(1-\alpha)\boldsymbol{I} + \alpha\boldsymbol{u}(t)\boldsymbol{u}(t)], \qquad \boldsymbol{\mu}(t) = \frac{1}{\zeta}[(1-\alpha)\boldsymbol{I} + \alpha\boldsymbol{u}(t)\boldsymbol{u}(t)] \tag{5.16}$$

These tensors are defined by the scalar coefficients D and ζ, respectively, and by the nondimensional tensor $(1-\alpha)\boldsymbol{I} + \alpha\boldsymbol{u}(t)\boldsymbol{u}(t)$, where $0 \geq \alpha < 1$ is the anisotropy parameter, $\boldsymbol{I}$ is the unit tensor, and $\boldsymbol{u}$ is the eigenvector (of unit length) of the gyration tensor of the chain, specifically the one corresponding to the largest of the three eigenvalues.

If the chain is divided into N subchains, and $\boldsymbol{R}_n$ $(n = 0, 1, ..., N)$ are the locations of the $N+1$ beads, the Smoluchowski equation for the distribution function $\Psi(\boldsymbol{R}_0, \boldsymbol{R}_1, ..., \boldsymbol{R}_N; t)$ is written as[84]:

$$\frac{\partial \Psi}{\partial t} = \sum_{n=0}^{N} \frac{\partial}{\partial \boldsymbol{R}_n} \cdot \left[\boldsymbol{D} \cdot \frac{\partial \Psi}{\partial \boldsymbol{R}_n} + (\boldsymbol{k} \cdot \boldsymbol{R}_n - \mu \cdot \boldsymbol{F}_n)\Psi\right] \tag{5.17}$$

Here $\boldsymbol{k}$ is the velocity gradient of the flow, and $\boldsymbol{F}_n$ is the force on the n-th bead exerted by the subchain springs. Hence, the bracket multiplying Ψ in eq (5.17) is the net convective velocity of the n-th bead. In the Ito interpretation,(refs) the set of Langevin equations corresponding to eq (5.17) is then written as

$$\mathrm{d}\boldsymbol{R}_n = \left(\frac{\partial}{\partial \boldsymbol{R}_n} \cdot \boldsymbol{D} + \boldsymbol{k} \cdot \boldsymbol{R}_n - \mu \cdot \boldsymbol{F}_n\right)\mathrm{d}t + \boldsymbol{B} \cdot \boldsymbol{\eta}_n \sqrt{2\mathrm{d}t}, \qquad n = 0, 1, ..., N \tag{5.18}$$

where $\boldsymbol{B}$ is the tensor obeying $\boldsymbol{B} \cdot \boldsymbol{B}^{\mathrm{T}} = \boldsymbol{D}$, and $\boldsymbol{\eta}_n$ are normal Gaussian vectors.

Needless to say, numerical integration of eq (5.18) requires calculation of the unit eigenvector u of the gyration tensor at each time step, thus allowing determination of $\boldsymbol{D}$ and $\boldsymbol{\mu}$, of the Cholesky square root $\boldsymbol{B}$, and of the set of the $N+1$ divergences $\frac{\partial}{\partial \boldsymbol{R}_n} \cdot \boldsymbol{D}$. As regards these divergences, in view of eq (5.16) we need to calculate $\frac{\partial}{\partial \boldsymbol{R}_n} \cdot \boldsymbol{u}\boldsymbol{u}$. The latter divergence is best rewritten by using the eigenvector $\boldsymbol{V}$ before normalization (see Appendix 6):

$$\frac{\partial}{\partial \boldsymbol{R}_n} \cdot \boldsymbol{u}\boldsymbol{u} = \frac{1}{\boldsymbol{V}}\left[\left(\frac{\partial}{\partial \boldsymbol{R}_n} \cdot \boldsymbol{V} - 2\boldsymbol{u} \cdot \frac{\partial \boldsymbol{V}}{\partial \boldsymbol{R}_n} \cdot \boldsymbol{u}\right)\boldsymbol{u} + \frac{\partial \boldsymbol{V}}{\partial \boldsymbol{R}_n} \cdot \boldsymbol{u}\right] \tag{5.19}$$

Finally, the set of gradient tensors $\frac{\partial \boldsymbol{V}}{\partial \boldsymbol{R}_n}$ needs to be calculated from the gyration tensor $\boldsymbol{G}$, which is a straightforward, if cumbersome, operation (see Appendix 6).

Up to now, we have not specified the expression for the subchain spring force $\boldsymbol{f}_n$, which is needed to calculate the force $\boldsymbol{f}_n$ on the beads. Indeed, at equilibrium, long-time relaxation properties of the system can be calculated by using the classical Gaussian expression $\boldsymbol{f}_n = \frac{3k_BT}{l_K^2}(\boldsymbol{R}_n - \boldsymbol{R}_{n-1})$, where l_K is the Kuhn length, and k_BT is thermal energy. Conversely, under flow, especially under fast flows, inextensibility of the subchains (Kuhn segments) must be accounted for, and the Fraenkel force is used instead

$$\boldsymbol{f}_n = H\left(1 - \frac{l_K}{l}\right)(\boldsymbol{R}_n - \boldsymbol{R}_{n-1}) \tag{5.20}$$

where $l = |\boldsymbol{R}_n - \boldsymbol{R}_{n-1}|$ is the current subchain length, and H is a suitably large spring constant that maintains l close to l_K at all times.

It should be noted that in eq (5.16) two scalar quantities appear, D and ζ, which at equilibrium are linked by the well-known Einstein relationship $D_{eq} = k_BT/\zeta_{eq}$, also known as fluctuation-dissipation theorem. As mentioned in the Introduction, it appears that such relationships break down in fast flows. Hence, in fast flows, not only we expect that the Kuhn-segment friction coefficient ζ becomes smaller than ζ_{eq} because of the flow-induced co-alignment of the Kuhn segments, but also that D will increase with respect to its equilibrium value D_{eq} in a way that does not fulfill the relationship $D = k_BT/\zeta$[52].

From the simulations we extract several observables, as averages over a sufficiently large number of chains. Conformational quantities are the chain end-to-end distance R_{ete}, and all the components of the gyration tensor $\boldsymbol{G}$. The rheological quantity is the stress tensor $\boldsymbol{T}$ given by:

$$\boldsymbol{T} = \nu\left[\sum_{n=1}^{N}\langle \boldsymbol{f}_n(\boldsymbol{R}_n - \boldsymbol{R}_{n-1})\rangle - e_p\boldsymbol{w}\boldsymbol{w}\right], \tag{5.21}$$

where ν is the chain number density, $\boldsymbol{w}$ is the unit eigenvector associated to the smallest eigenvalue of the gyration tensor $\boldsymbol{G}$, and e_p is an unknown factor with dimension of energy. The first term in eq (5.21) is the classical Kramer expression for phantom chains that accounts for intrachain forces only. As discussed later in this Chapter, the second term arises in fast flows from interchain excluded volume interactions. As is known, the latter are irrelevant in polymer melts at equilibrium [], i.e., at equilibrium it is $e_p = 0$.

5.3.2 Results and Discussion

5.3.2.1 Linear Viscoelasticity

We here compare predictions of the model with the molecular dynamics results of Xu et al.[138] on Kremer-Grest (KG) unentangled melts. In particular, we focus on KG chains with 30 and 50 beads because their results on longer chains already show entanglement effects.

In Table I of the Xu et al.[138] paper the following equilibrium properties are reported: i) the longest relaxation time τ_{long} (extracted from the end-to-end vector autocorrelation), ii) the zero-shear viscosity η_0 (extracted from the low shear rate asymptote in Figure 1 of Xu et al[138].), and iii) the average square end-to-end distance R^2_{ete}. Table I below reports all such quantities in Lennard-Jones (LJ) units. We will use LJ units throughout this Section.

Table 5.2: Properties of the two unentangled KG melts of Xu et al.[138]

Number of beads	τ_{long}	η_0	R^2_{ete}	N	τ_R	α	ν
30	834	20.2	46.3	17	700	0.35	0.028
50	2500	37.9	80.2	28	1800	0.4	0.017

The curvilinear length L of the two chains is also known from $L = N_b l_b$, where N_b is the number of bonds (29 and 49, respectively), and $l_b = 0.965$ is the bond length of the KG chain [125]. From R^2_{ete} and L the number N of Kuhn segments and the Kuhn segment length l_K are determined by solving the equations: $R^2_{ete} = N l_K^2$ and $L = N l_K$. Values of N (rounded to integer numbers) are reported in Table 5.2, and the value of $l_K \approx 1.7$ agrees with literature results [125].

It is now worth calculating the Rouse time τ_R of the two chains from the formula $\tau_R = \zeta_{eq} l_K^2 / (12 k_B T \sin^2[\pi/(2N+2)])$ [76]. Here, the equilibrium friction coefficient ζ_{eq} of the Kuhn segment is obtained from the literature value of the KG bead friction coefficient $\zeta_b = 12.4 \pm 1$ [125] as $\zeta_{eq} = \zeta_b l_K / l_b \approx 22$. The values of τ_R so obtained (see Table 5.2) confirm that the Rouse model is inadequate, while a bland topological interaction explains why τ_{long} is found somewhat larger than τ_R, the more so the larger is N.

In our simulations, topological effects are introduced through the anisotropy parameter α, and we find that $\alpha = 0.35$ and $\alpha = 0.4$, for $N = 17$ and $N = 28$, respectively, generate $\tau_{long} = 845$ and $\tau_{long} = 2540$, respectively, in agreement with the data in Table 5.2. Figure 1 shows the end-to-end autocorrelation function for both KG melts as generated by our coarse-grained simulation. In this linear-log plot, the ultimate slope gives $1/\tau_{long}$. The values of α so obtained will be maintained throughout the rest of the paper.

To calculate the zero-shear viscosity, we first compute the linear relaxation modulus $G(t)$ from the Green-Kubo stress autocorrelation function [76], and then use the relationship $\eta_0 = \int_0^\infty G(t)\mathrm{d}t$. Calculation of the stress requires the chain number density ν (see eq (5.21)), given by $\nu = \rho/[m_b(N_b + 1)]$. Since $\rho = 0.85$ and $m_b = 1$, we find the values reported in Table 5.2. Figure 2 reports the $G(t)$ curves for both KG melts, calculated from Fraenkel chain simulations with the same parameters as in Figure 5.19.

Integration of the $G(t)$ curves gives $\eta_0 = 19$ and $eta_0 = 37$, for the two KG melts, respectively. Comparison with the η_0 values of Xu et al.[138] reported in Table 5.2 indicates that the glassy dynamics (not accounted for in our simulations) gives a small contribution to the zero-shear viscosity, of the order of a few percent for both KG melts. In particular, we estimate a glassy viscosity $\eta_G \approx 1$. This is in agreement with the fact that the molecular dynamics simulations of Xu et al.[138] are run at $T = 1$, far above the glass transition temperature (Kremer and Grest, 1990[65]).

Before moving on to the nonlinear range, it is fair to also perform a comparison with the KG melt data of Likhtman and co-workers[77], which also include results of chains with 50 beads. Figure 5.21 reports that comparison in terms of $G(t)t^{0.5} vs.t$, where symbols are KG data, and the green line are the corresponding Fraenkel chain predictions reported in Figure 5.20.

Both figures confirm that the glassy contribution is not relevant. Deviations at short times are probably not significant for our purpose. It is finally fair to mention that there is a non-negligible discrepancy between Xu[138] and Likhtman[77] result, insofar the zero-shear viscosity of Xu is 38 while Likhtman indicates the value 45, which is closer to our prediction.

Values of Kuhn segment length, $l_K = 1.7$, and equilibrium friction coefficient, $\zeta_{eq} = 22$, as well as $\alpha = 0.35$ and 0.4 here determined for $N = 17$ and 28, respectively, are all parameters needed to solve the Langevin equation (eq (5.17)) for any value of the velocity gradient $\boldsymbol{k}$. In particular, shear flows are considered in the next section.

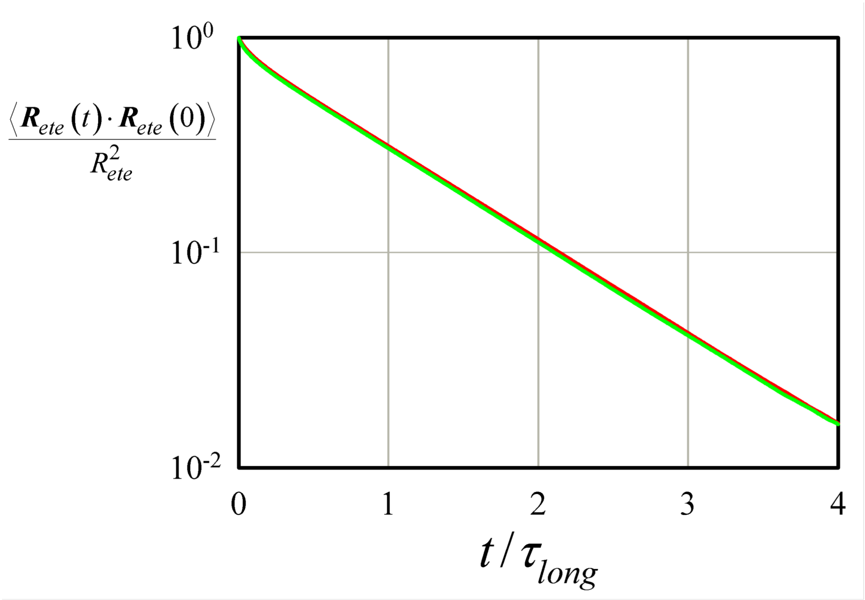

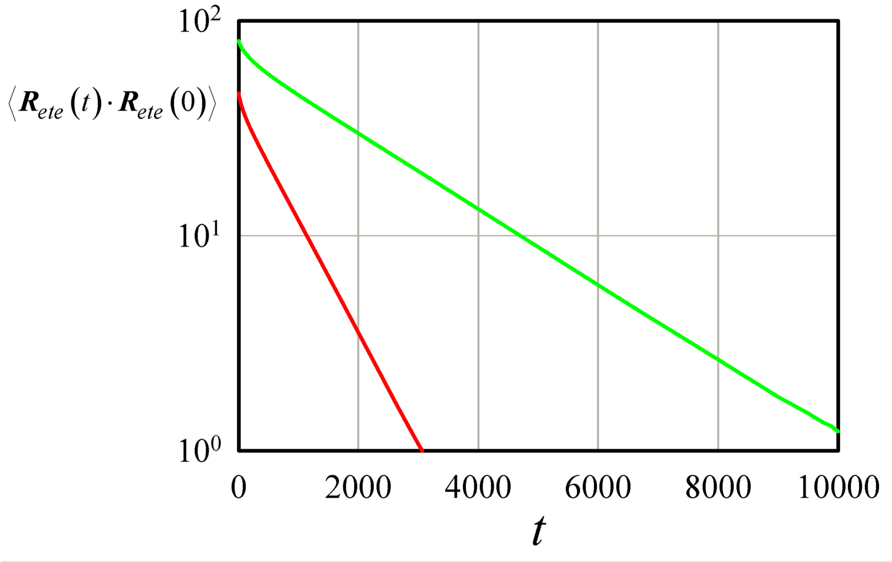

Figure 5.19: End-to-end autocorrelation function for KG melts of 30 and 50 beads, obtained from Kuhn-segment-level coarse-grained Brownian simulations with anisotropic mobility. - Parameters are $N = 17$, $\alpha = 0.35$ (red line), and $N = 28$, $\alpha = 0.4$ (green line).

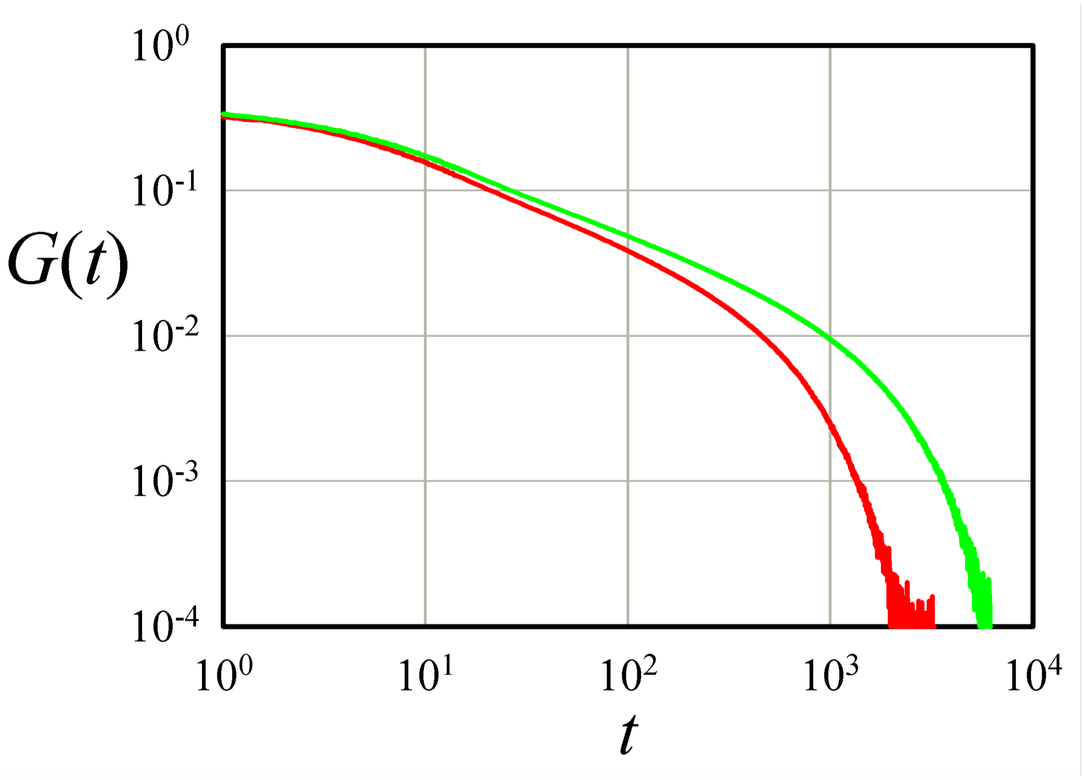

Figure 5.20: Linear relaxation modulus of the KG melts with 30 and 50 beads, red and and green lines, respectively. - Parameters as in Figure 5.19

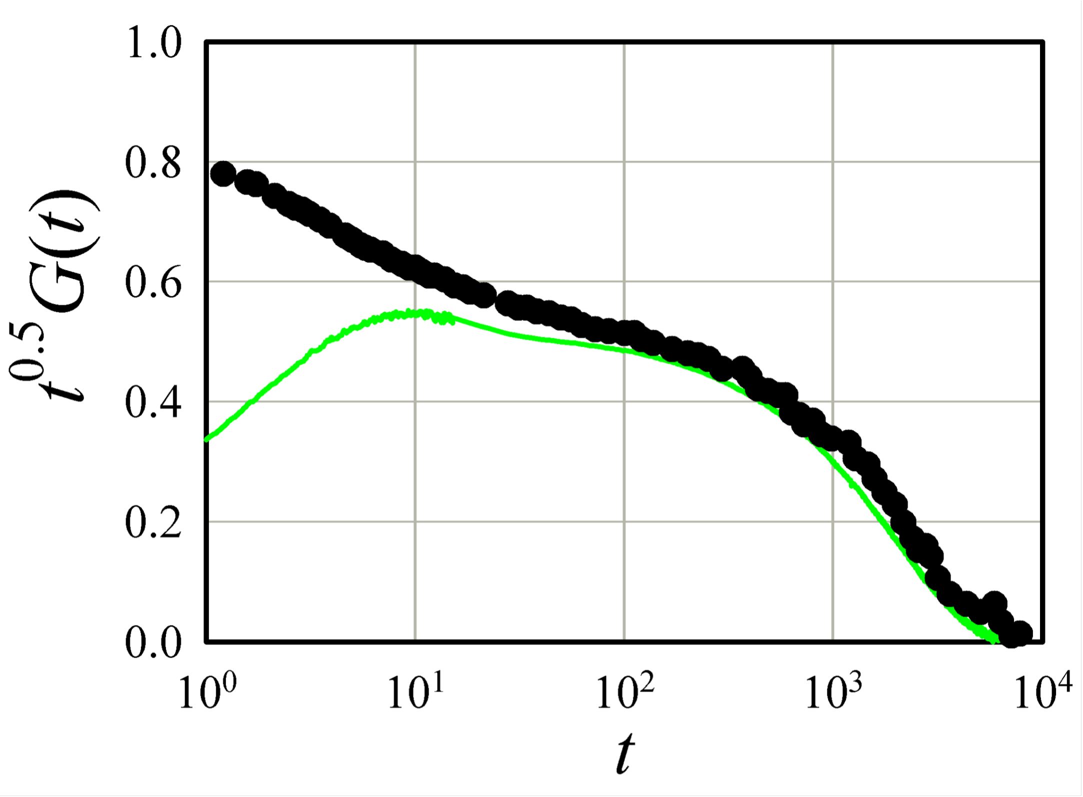

Figure 5.21: Comparison of model predictions with $G(t)$ data of KG melts with 50 beads reported by Likhtman et al.[77] - Parameters as in Figure 5.19

5.3.2.2 Shear Flow

We first run our simulations by letting the parameters ζ at the equilibrium value ζ_{eq}, and D at the Einstein value $D_{eq} = k_B T/\zeta_{eq}$. For the time being, we will calculate the stress tensor by setting $e_p = 0$. Starting from equilibrium conformations of the chains, we switch on a shear rate $\dot{\gamma}$, and advance in time sufficiently long so as to reach a steady state, and compare our predictions with the steady shear data of Xu et al[138].

Figures 5.22-5.25 report their data of shear viscosity η, first normal stress difference N_1, second normal stress difference N_2, and end-to-end distance R_{ete}, versus $\dot{\gamma}$, for 30 bead KG melts. In the same figures, green squares are simulation results with parameter values determined in the previous section and orange circles are simulation results obtained in the previous Chapter. In slow flows, $\dot{\gamma}\tau_{long} < 1$, agreement between simulations and data is satisfactory. Particularly relevant is the good agreement with the value of N_2, which represents a confirmation of the α values determined in the previous section. It is worth recalling again that, without anisotropy ($\alpha = 0$), N_2 would be zero. In fast flows agreement between predictions and data is totally lost, with the possible exception of the viscosity. Indeed, both R_{ete} and N_1 are predicted larger than observed, and N_2 approaches a plateau, while data keep increasing with increasing $\dot{\gamma}$.

Figures 5.26-5.29 show the results of radius gyration tensor components $\langle G_{xx} \rangle$, $\langle G_{yy} \rangle$, $\langle G_{zz} \rangle$, and $\langle G_{xy} \rangle$ for 30 bead KG melts. Compared with the data (solid circles), both anisotropic results and isotropic results have good agreement with data at low shear rates, even though they depart from the data at high shear rates ($\langle G_{xx} \rangle$, $\langle G_{yy} \rangle$, and $\langle G_{zz} \rangle$) or at the intermediate shear rates ($\langle G_{xy} \rangle$). In addition, the anisotropic results slightly shrink the discrepancies between the isotropic results and the data. The anisotropic friction reduction model hopefully improves the results, which will be left for the future work.

5.4 Conclusions

The steady-shear-flow molecular dynamics results on two unentangled Kremer-Grest melts, reported by Xu et al.[138], already analyzed in the previous chapter by using the Rouse-like constitutive equation very recently suggested by Watanabe and coworkers (2021)[134], have here been carefully re-analyzed through single-chain Brownian

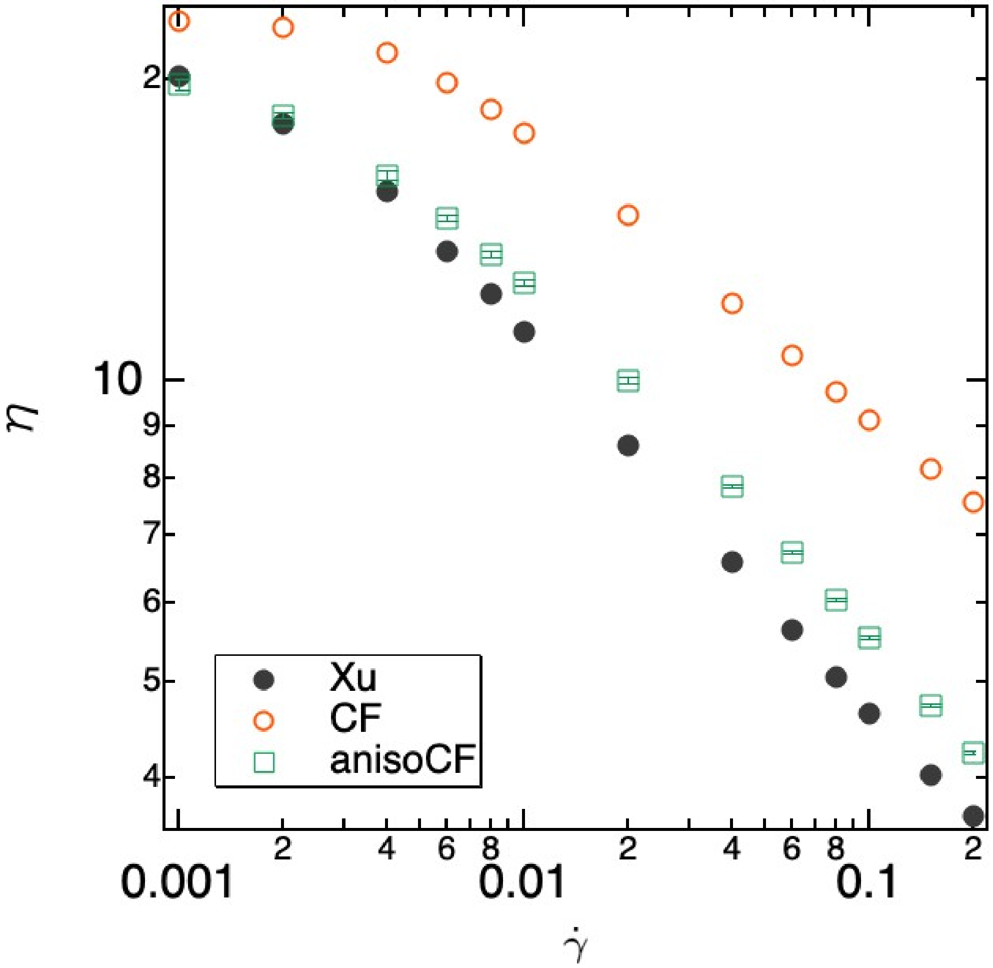

Figure 5.22: Steady-state shear viscosity as a function of shear rate - Hereinafter, "anisoCF" indicates "anisotropy constant friction".

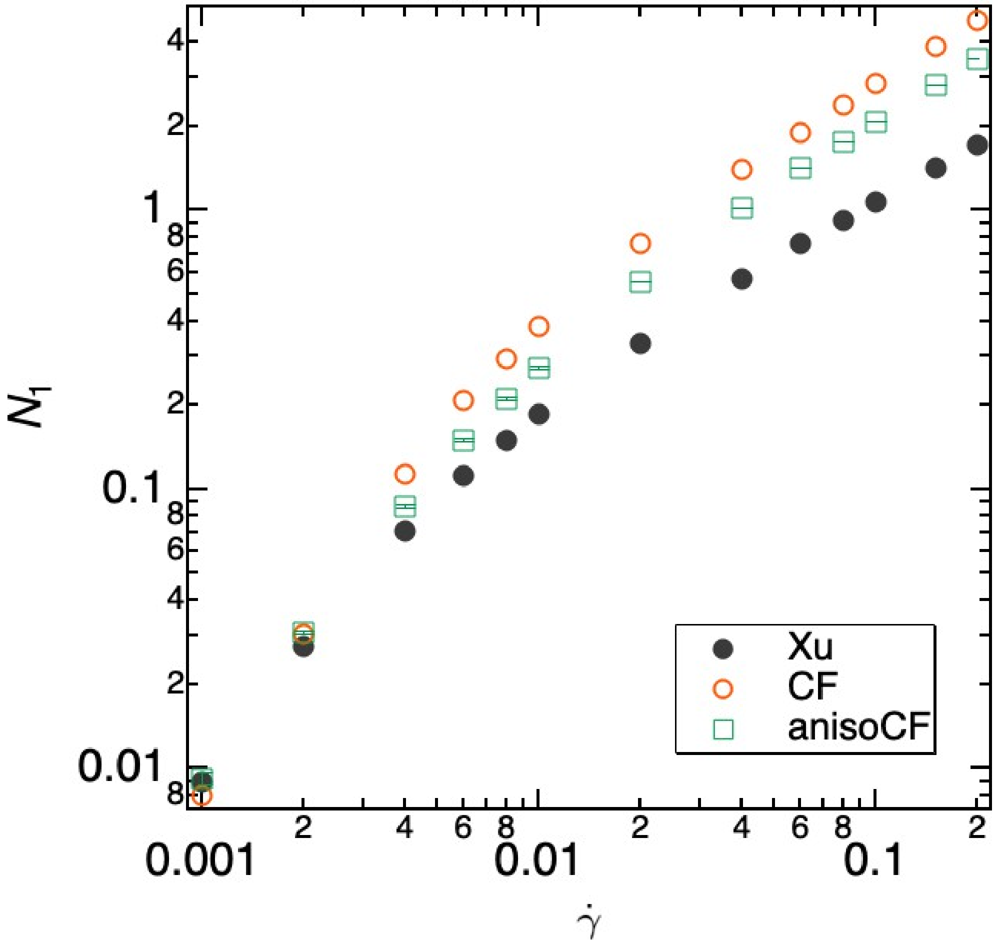

Figure 5.23: Comparisons of viscometric functions among the isotropic constant friction results, anisotropy constant friction results, and the data. - The first normal stress difference.

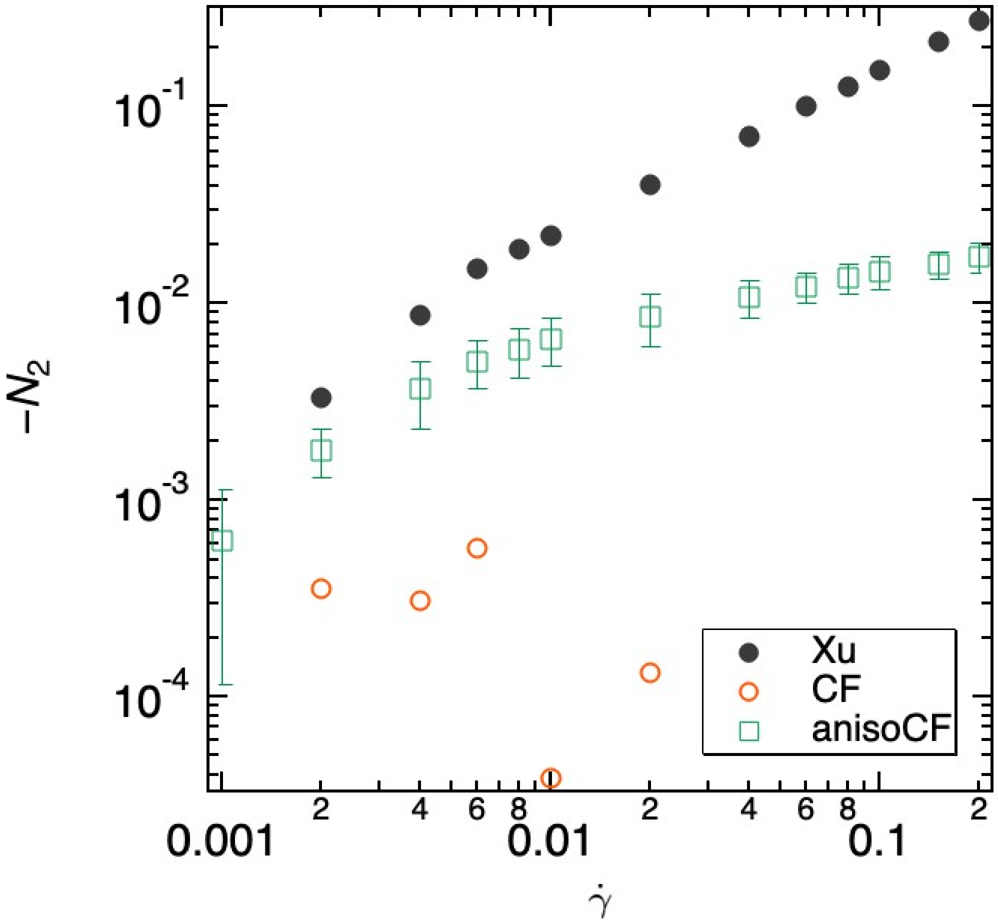

Figure 5.24: Comparisons of viscometric functions among the isotropic constant friction results, anisotropy constant friction results, and the data. - The second normal stress difference.

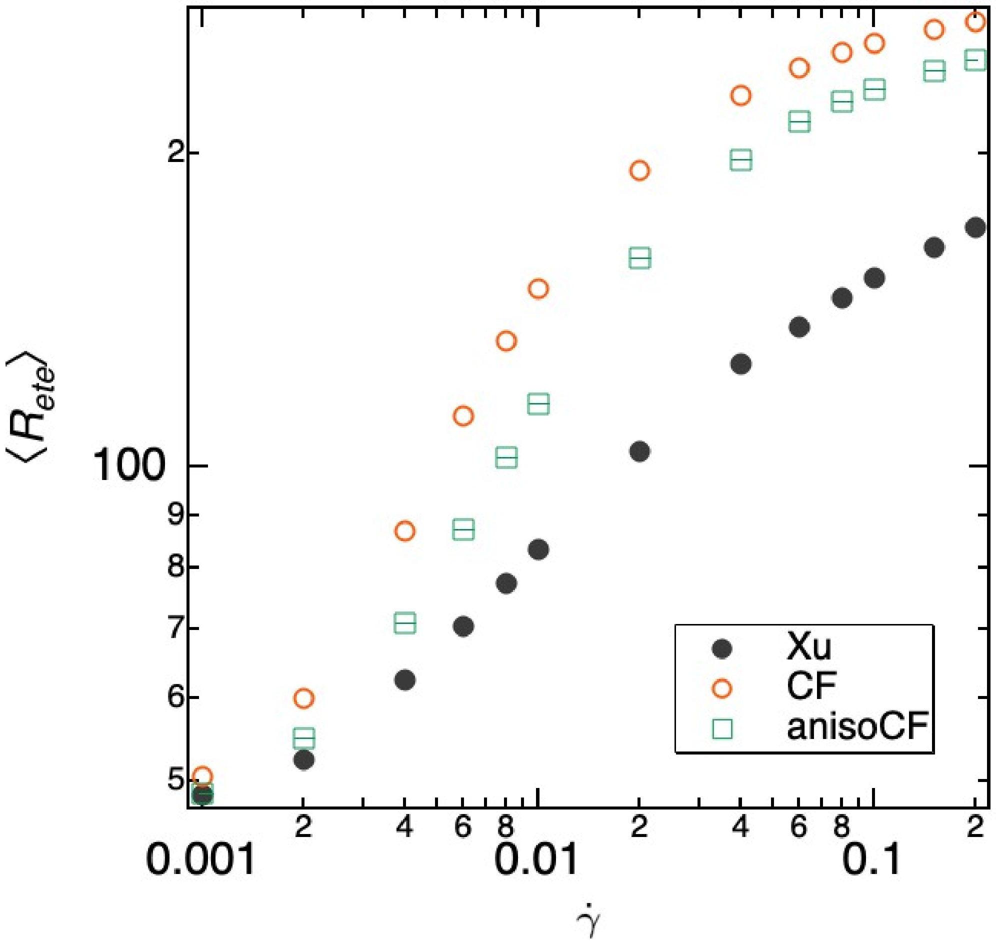

Figure 5.25: Comparisons of viscometric functions among the isotropic constant friction results, anisotropy constant friction results, and the data. - Root-mean-square chain end-to-end distance.

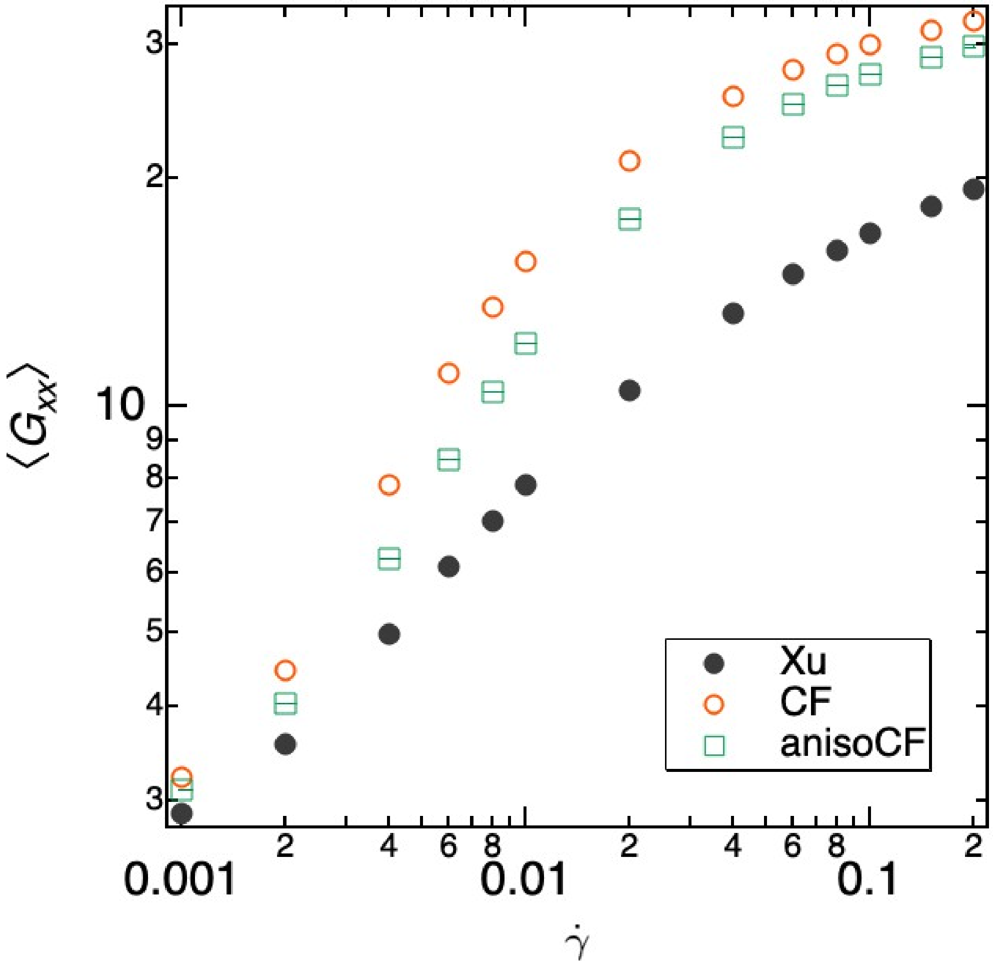

Figure 5.26: Comparisons of radius gyration tensor component among the isotropic constant friction results, anisotropy constant friction results, and the data. - $\langle G_{xx} \rangle$

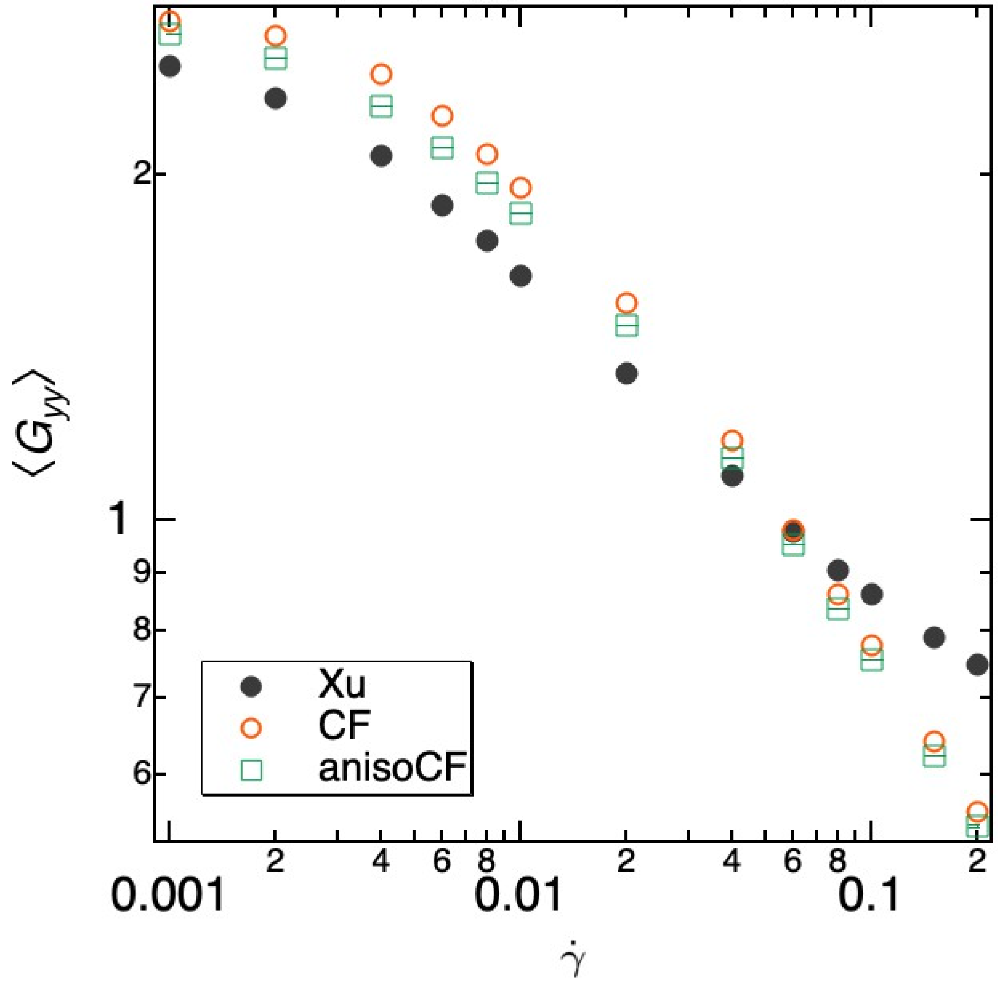

Figure 5.27: Comparisons of radius gyration tensor component among the isotropic constant friction results, anisotropy constant friction results, and the data. - $\langle G_{yy} \rangle$

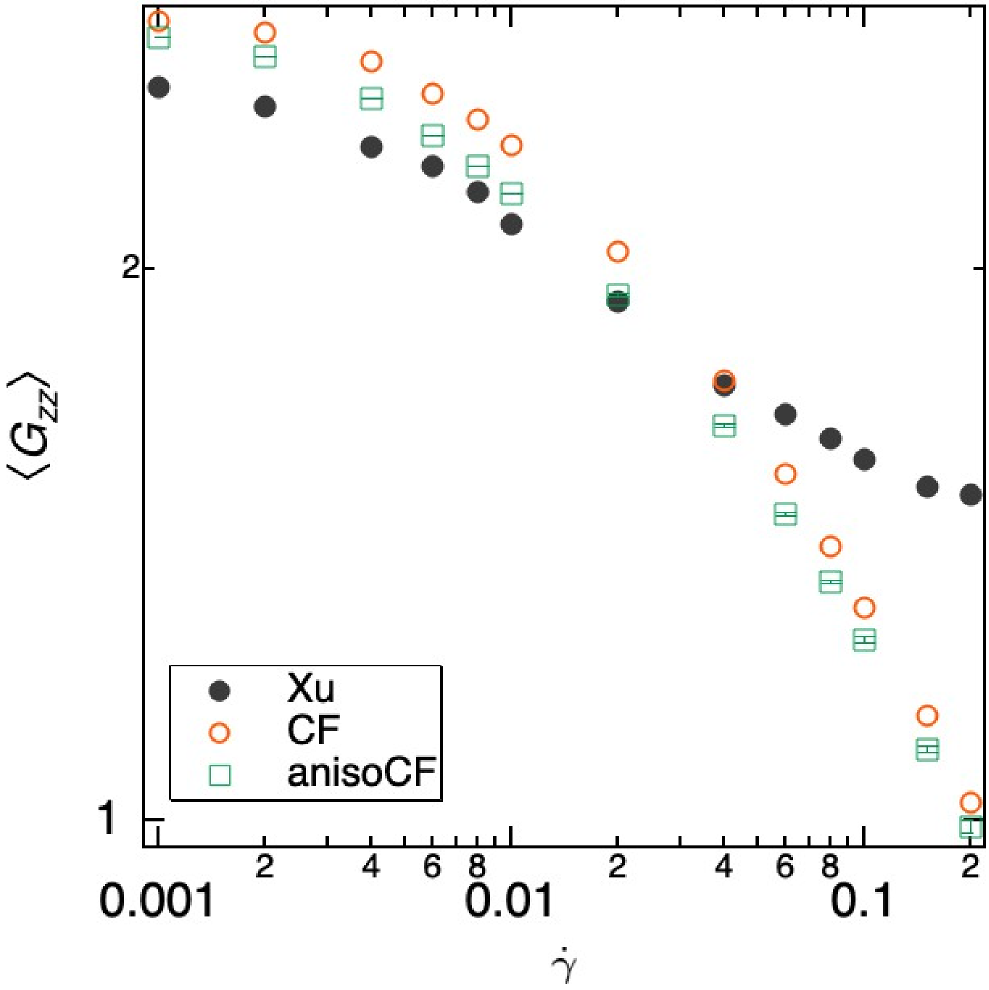

Figure 5.28: **Comparisons of radius gyration tensor component among the isotropic constant friction results, anisotropic constant friction results, and the data. -** $\langle G_{zz} \rangle$

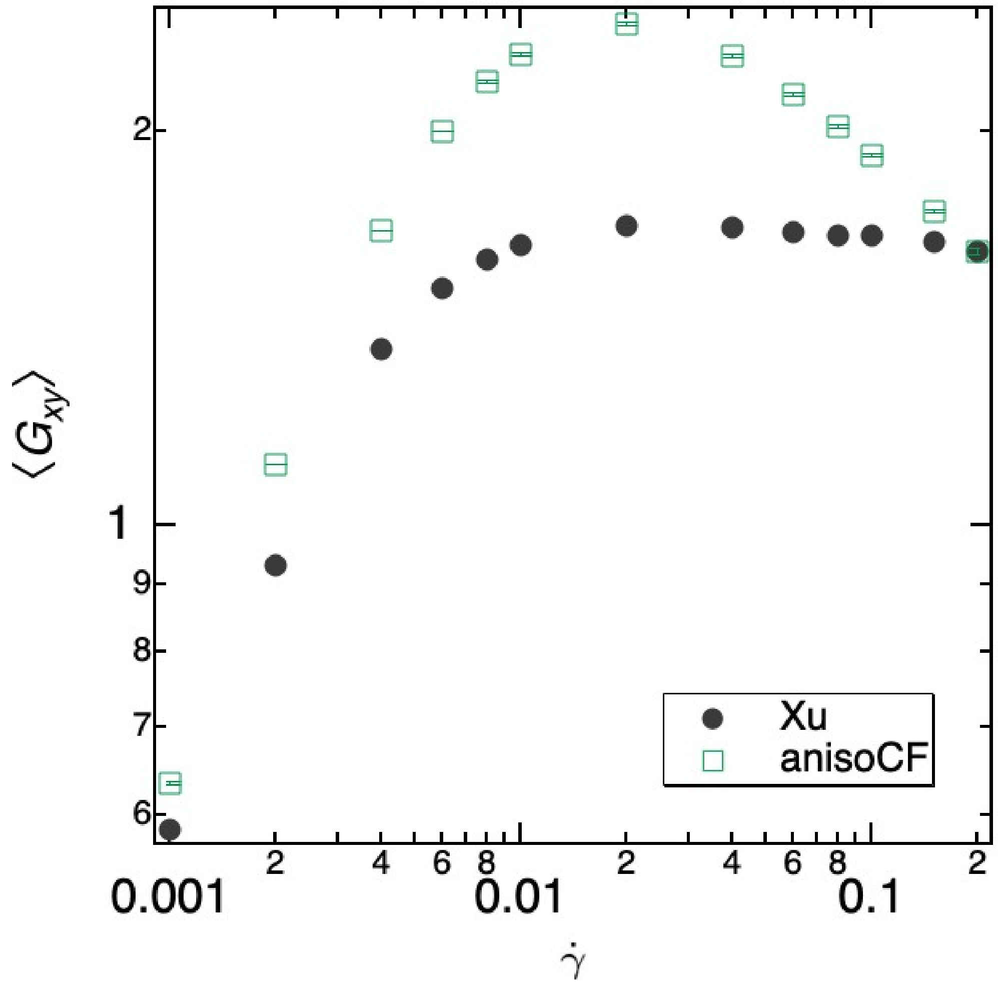

Figure 5.29: Comparisons of radius gyration tensor component among the isotropic constant friction results, anisotropic constant friction results, and the data. - $\langle G_{xy} \rangle$

dynamics simulations. Those simulations first accounted for FENE effects by coarse graining chains at the Kuhn segment scale, and by mimicking the rod-like behavior of the Kuhn segments through suitably stiff Fraenkel springs. Results confirm that FENE effects alone are not sufficient to describe the complex nonlinear behavior of unentangled KG melts. As already shown for the case of unentangled polystyrene melts, though a better agreement with KG melt data can be attained by accounting for flow-induced friction reduction effects, simulations still predict a virtually zero second normal stress difference, similarly to the Rouse-like model of Watanabe and coworkers, but inconsistently with the data of Xu et al[138].

We have here shown that to improve predictions for the second normal stress difference some topological effects must be accounted for. In particular, we accounted for those topological effects by endowing the beads of the Kuhn chain with an anisotropic mobility. Similarly to the case of entangled melts, beads are here assumed to move preferentially along some direction: chains are here seen as ellipsoids, diffusing preferentially along the major axis of such ellipsoid, the diffusion in the orthogonal direction being somewhat restricted by the steric hindrance of the surrounding chains. Such anisotropy affects dynamic properties already at equilibrium, and for that reason we have extracted the anisotropy parameter α of eq (5.16) by fitting the equilibrium autocorrelation of the chain end-to-end vectors.

Preliminary results of this anisotropic model are very encouraging, being also consistent with the second normal stress data in slow flows (compare Figure 5.17 with Figure 5.24). To improve predictions in fast flows, the simulations must obviously account for friction reduction effects, and probably also for the possible violation of the fluctuation-dissipation theorem, as suggested by Watanabe and coworkers. A further possible complication is due to the fact that interchain excluded volume interactions, which are known to be screened at equilibrium in melts, become important in fast flows. Those flow-induced pressure-like interactions could indeed explain the large values of the second normal stress difference in fast flows (see Figure 5.24). Understanding all these aspects is left as future work.

6

Summarizing Chapter

In this thesis, we have studied the linear and nonlinear rheological behavior of ordinary and associating unentangled polymer melts through molecular modeling approaches. Results not only enhanced our understanding of the rich dynamic behavior of associating polymers, resulting from the the complicated topological structures and the breaking/re-forming kinetics of the physical bonds, but also promoted our understanding of the mechanism of the friction reduction of unentangled polymer melts in fast flows.

In Chapter 2, we developed a multi-chain model to study the topological properties as well as the dynamics of reversible polymer networks, where a periodic simulation box was introduced to overcome the surface effects at a molecular scale. This box was designed to also be used under flow. To save on computing time, a multi-tau correlator algorithm was used. Effects of the lifetime, density and distribution of stickers on the viscoelastic response of associating polymers were studied. Our results confirmed that the distribution of stickers has an effect on the viscoelastic response of reversible polymer networks, whereas this is ignored in the sticky Rouse model proposed by Chen et al. [22]. In addition, our results showed that the lifetime of stickers has almost no effects on the local dynamics of chains but significant effects on the viscoelastic response at low and intermediate frequencies with a significant time delay. Furthermore, our results indicated that the sticker density determines the level of the $G'(\omega)$ plateau at the intermediate frequencies as well as that the chains with more stickers had a longer terminal relaxation time.

In Chapter 3, a simple single-chain model, based on the classic sticky-Rouse model, was proposed. Our results showed good agreement with the data of Lewis et al. [74], especially at the intermediate frequencies, where the predictions of the model proposed both by Cui et al. [27] and by Chen et al.[22] failed to fit the data. Then we compared with the data reported by Cui et al. [27]. The good agreement of the results predicted by our sticky-Rouse model with the data of the chain having two stickers implied that the association generated longer chains but no network structure, where a larger number of Kuhn segments was used. The true lifetime of the sticky junction was estimated by the the longest relaxation time of the associated chain with two stickers. Indeed, when in this case sticky junctions detach, the opportunity that the same two stickers recombine is expected not to be significantly different from that of combining with a different partner. Our results had good agreement with the data with more than two stickers per chain as well.

In Chapter 4, we compared the nonlinear rheological behavoir of unentangled and entangled melts in shear and elongational flows to emphasize that unentangled melts are not rheologically simpler than entangled ones. The nonlinear behavior (i.e. strain-hardening and strain-softening) are attributable to the stretch-and orientation-induced ζ reduction and the finite extensible nonlinear elasticity (FENE) effect. The very recent model proposed by Watanabe et al (2021)[134] was used for the first time to fit the rich data set of Kremer-Grest melts under fast flow reported by Xu et al.[138]. Results confirmed that FENE and friction reduction effects are important in fast flows of unentangled melts. More importantly, the results in Chapter 4 strongly confirm Watanabe's suggestion that the fluctuation dissipation theorem is not fulfilled in fast flows. Indeed, we have shown that the Brownian force almost remains the same as that at the equilibrium state, rather than decreasing together with the friction.

In Chapter 5, Brownian dynamics simulations of ordinary unentangled polymer melts were performed to improve agreement with Xu et al data, revealing, among other things, a nonzero second normal stress difference, differently from the predictions of Watanabe's model. We first considered beads endowed with isotropic friction. Even though the results are capable of capturing the main features of the data, discrepancies indicated that FENE effects alone are not sufficient to describe the complex nonlinear behavior of unentangled KG melts. Then we proposed another model, where beads were endowed with anisotropic friction. Preliminary results of this anisotropic model are very encouraging. The results showed improved predictions for the second normal stress difference. To further improve the results, friction reduction effects have to be taken into account, which is left as future work.

Appendix A

Calculation of the gradient $\partial\boldsymbol{\nu}/\partial\boldsymbol{R}$ of the eigenvector $\boldsymbol{\nu}$

As is well known, the eigenvalues λ of the moment of inertia $\boldsymbol{M}$ are found from the cubic equation

$$\det(\boldsymbol{M}-\lambda\boldsymbol{I}) = \det\begin{pmatrix} M_{11}-\lambda & M_{12} & M_{13} \\ M_{12} & M_{22}-\lambda & M_{23} \\ M_{13} & M_{23} & M_{33}-\lambda \end{pmatrix} = 0, \tag{A.1}$$

where the M_{ij}'s are the 6 Cartesian components of the symmetric tensor $\boldsymbol{M}$.

The Cartesian components of the eigenvector $\boldsymbol{\nu}$ mentioned in the paper are obtained from the minors of the matrix $(\boldsymbol{M}-\lambda\boldsymbol{I})$. If we choose the minors of the elements of the first row, we write:

$$\begin{aligned} \nu_1 &= (M_{22}-\lambda)(M_{33}-\lambda) - M_{23}^2, \\ \nu_2 &= M_{13}M_{23} - M_{12}(M_{33}-\lambda), \\ \nu_3 &= M_{12}M_{23} - M_{13}(M_{22}-\lambda) \end{aligned} \tag{A.2}$$

where it is understood that in this and in the following formulas λ is the largest of the three eigenvalues.

Lets now assume that the moment of inertia $\boldsymbol{M}$ is differentially modified by $\mathrm{d}\boldsymbol{M}$. There follows that also the Cartesian components of $\boldsymbol{\nu}$ are modified (to first order) by the differential quantities:

$$\begin{aligned}
\mathrm{d}\nu_1 &= (M_{22}-\lambda)\mathrm{d}M_{33} + (M_{33}-\lambda)\mathrm{d}M_{22} - 2M_{23}\mathrm{d}M_{23} - (M_{22}+M_{33}-2\lambda)\mathrm{d}\lambda,\\
\mathrm{d}\nu_2 &= M_{13}\mathrm{d}M_{23} + M_{23}\mathrm{d}M_{13} - M_{12}\mathrm{d}M_{33} - (M_{33}-\lambda)\mathrm{d}M_{12} + M_{12}\mathrm{d}\lambda, \qquad \text{(A.3)}\\
\mathrm{d}\nu_3 &= M_{12}\mathrm{d}M_{23} + M_{23}\mathrm{d}M_{12} - M_{13}\mathrm{d}M_{22} - (M_{22}-\lambda)\mathrm{d}M_{13} + M_{13}\mathrm{d}\lambda.
\end{aligned}$$

On the other hand, $\mathrm{d}\lambda$ is itself related to $\mathrm{d}\boldsymbol{M}$. Indeed, by differentiating eq (A.1), one obtains:

$$\mathrm{d}\lambda = m_{11}\mathrm{d}M_{11} + m_{22}\mathrm{d}M_{22} + m_{33}\mathrm{d}M_{33} + 2m_{12}\mathrm{d}M_{12} + 2m_{13}\mathrm{d}M_{13} + 2m_{23}\mathrm{d}M_{23}, \quad \text{(A.4)}$$

where the m_{ij}'s are the minors of the corresponding elements of the matrix $(\boldsymbol{M}-\lambda\boldsymbol{I})$, changed in sign if $i+j$ is odd, and divided by the quantity:

$$(M_{11}-\lambda)(M_{22}-\lambda)+(M_{22}-\lambda)(M_{33}-\lambda)+(M_{11}-\lambda)(M_{33}-\lambda)-M_{12}^2-M_{13}^2-M_{23}^2. \quad \text{(A.5)}$$

For future reference, it should be noted that the m_{ij}'s are the 6 Cartesian components of a symmetric tensor $\boldsymbol{m}$.

We now recall that we are interested in the differential modification of $\boldsymbol{M}$ due to changing by $\mathrm{d}\boldsymbol{R}$ the location $\boldsymbol{R}$ of one of the beads of the chain. (Here and in the following we omit the bead index n from $\boldsymbol{R}_n$to avoid confusion with the coordinate indices.) If $\boldsymbol{R}$ is measured from the center of mass of the molecule, $\mathrm{d}\boldsymbol{M}$ is given by

$$\mathrm{d}\boldsymbol{M} = \boldsymbol{R}\mathrm{d}\boldsymbol{R} + \mathrm{d}\boldsymbol{R}\boldsymbol{R}, \qquad \text{(A.6)}$$

or, in Cartesian component form:

$$\begin{pmatrix} \mathrm{d}M_{11} & \mathrm{d}M_{12} & \mathrm{d}M_{13}\\ \mathrm{d}M_{12} & \mathrm{d}M_{22} & \mathrm{d}M_{23}\\ \mathrm{d}M_{13} & \mathrm{d}M_{23} & \mathrm{d}M_{33} \end{pmatrix} = \begin{pmatrix} R_1\mathrm{d}R_1 + R_1\mathrm{d}R_1 & R_1\mathrm{d}R_2 + R_2\mathrm{d}R_1 & R_1\mathrm{d}R_3 + R_3\mathrm{d}R_1\\ R_1\mathrm{d}R_2 + R_2\mathrm{d}R_1 & R_2\mathrm{d}R_2 + R_2\mathrm{d}R_2 & R_2\mathrm{d}R_3 + R_3\mathrm{d}R_2\\ R_1\mathrm{d}R_3 + R_3\mathrm{d}R_1 & R_2\mathrm{d}R_3 + R_3\mathrm{d}R_2 & R_3\mathrm{d}R_3 + R_3\mathrm{d}R_3 \end{pmatrix}. \qquad \text{(A.7)}$$

It is then found that substituting eq (A.7) into eq (A.4) gives

$$\mathrm{d}\lambda = \boldsymbol{w}\cdot\mathrm{d}\boldsymbol{R}, \qquad \text{(A.8)}$$

where vector $\boldsymbol{w}$ is itself obtained from tensor $\boldsymbol{m}$ as:

$$\boldsymbol{w} = 2\boldsymbol{m}\cdot\boldsymbol{R}. \qquad \text{(A.9)}$$

Finally, replacing eqs (A.7)-(A.8) into eq (A.3) for d$\boldsymbol{\nu}$ gives the 9 Cartesian components of the tensor $\frac{\partial \boldsymbol{\nu}}{\partial \boldsymbol{R}}$:

$$
\begin{aligned}
\frac{\partial \nu_1}{\partial R_1} &= -(M_{22} + M_{33} - 2\lambda)w_1, \\
\frac{\partial \nu_1}{\partial R_2} &= 2R_2(M_{33} - \lambda) - 2R_3M_{23} - (M_{22} + M_{33} - 2\lambda)w_2, \\
\frac{\partial \nu_1}{\partial R_3} &= 2R_3(M_{22} - \lambda) - 2R_2M_{23} - (M_{22} + M_{33} - 2\lambda)w_3, \\
\frac{\partial \nu_2}{\partial R_1} &= R_3M_{23} - R_2(M_{33} - \lambda) + M_{12}w_1, \\
\frac{\partial \nu_2}{\partial R_2} &= R_3M_{13} - R_1(M_{33} - \lambda) + M_{12}w_2, \\
\frac{\partial \nu_2}{\partial R_3} &= R_2M_{13} + R_1M_{23} - 2R_3M_{12} + M_{12}w_3, \\
\frac{\partial \nu_3}{\partial R_1} &= R_2M_{23} - R_3(M_{22} - \lambda) + M_{13}w_1, \\
\frac{\partial \nu_3}{\partial R_2} &= R_3M_{12} + R_1M_{23} - 2R_2M_{13} + M_{13}w_2, \\
\frac{\partial \nu_3}{\partial R_3} &= R_2M_{12} - R_1(M_{22} - \lambda) + M_{13}w_3.
\end{aligned}
\tag{A.10}
$$

We recall that in eq (A.10), $\boldsymbol{R}$ is measured from the center of mass, and λ is the largest of the three eigenvalues of the moment of inertia $\boldsymbol{M}$. We also note that vector $\boldsymbol{w}$, just like vector $\boldsymbol{R}$, is bead-dependent, i.e., for both vectors, as well as for the tensor $\frac{\partial \boldsymbol{\nu}}{\partial \boldsymbol{R}}$, the bead index n is understood.

Appendix B

Accuracy of Simulation Approaches

B.1 Simulation on Fraenkel Chain

In Chapter 4 and 5, we studied the viscoelastic response and the structural properties of polymer melts in steady fast flow. Figure. B.1 illustrates the effect of the time step dt. In the simulation, the time step was chosen as 5×10^{-5}. We can also decide the starting time of the steady state from Figure. B.1. Spring constant is another constant crucial to the simulation results. Figure. B.2 shows the simulation results of a variable that is proportional to the viscosity with different spring constant for $N = 30$ and $N = 50$. The value $H_k = 500$ was chosen in our simulation.

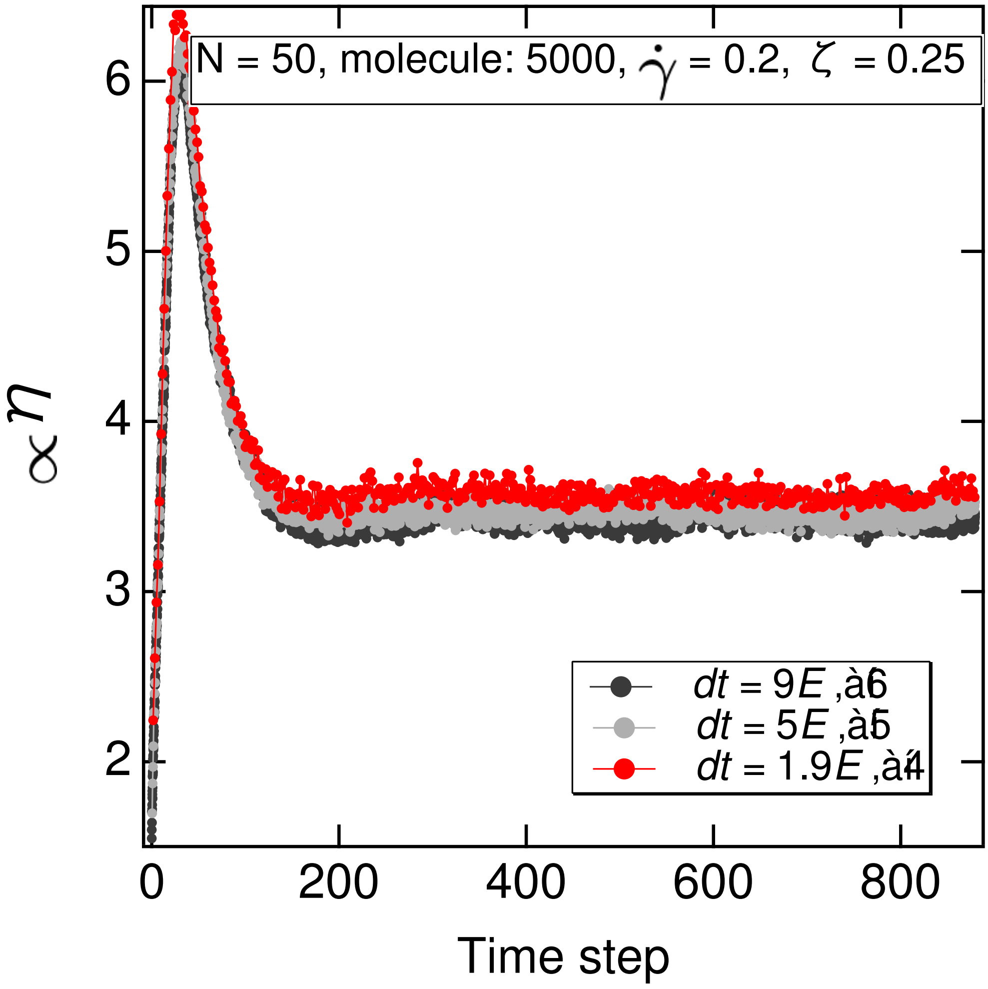

Figure B.1: A variable proportional to viscosity as a function of time. - Effect of time step

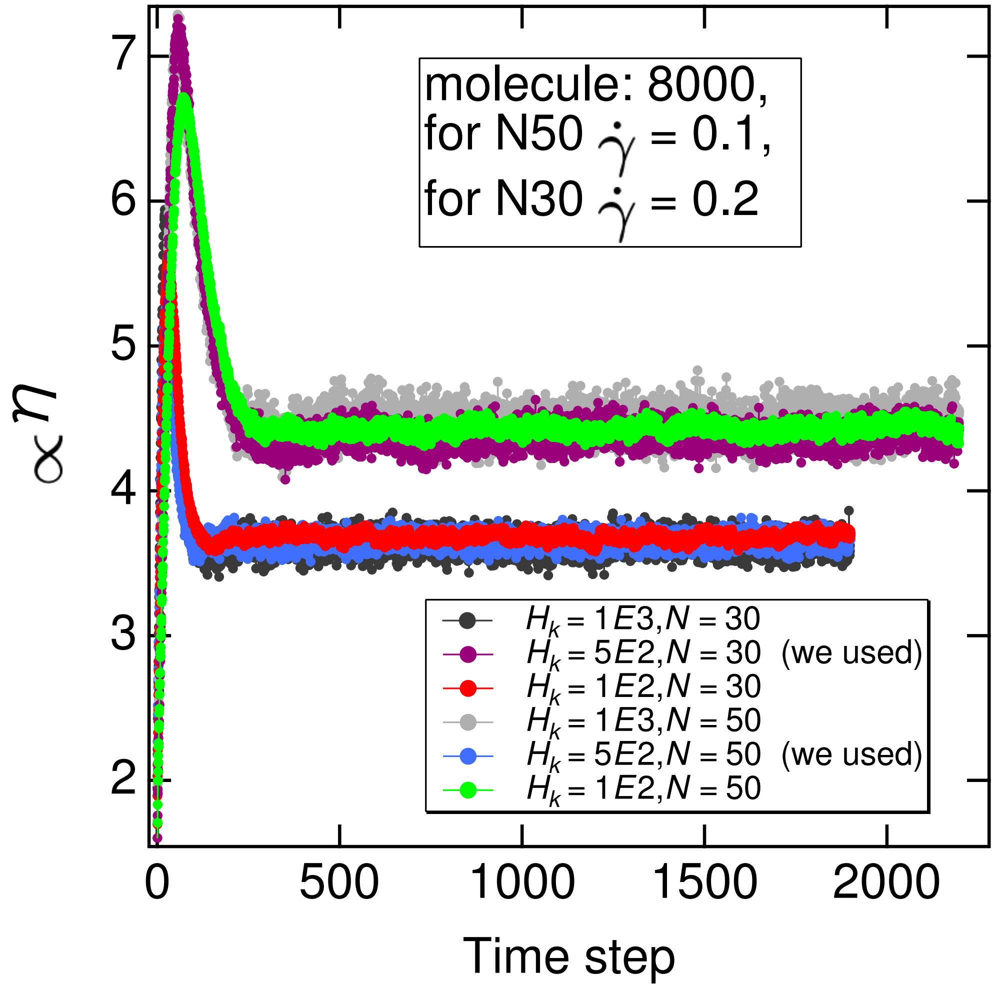

Figure B.2: A variable proportional to viscosity as a function of time. - Effect of spring constant in both N30 and N50 cases.

References

[1] Mostafa Ahmadi, Laurence G. D. Hawke, Hadi Goldansaz, and Evelyne van Ruymbeke. **Dynamics of Entangled Linear Supramolecular Chains with Sticky Side Groups: Influence of Hindered Fluctuations**. *Macromolecules*, **48**(19):7300–7310, sep 2015.

[2] Nicolas J. Alvarez, José Manuel Román Marín, Qian Huang, Michael Locht Michelsen, and Ole Hassager. **Creep Measurements Confirm Steady Flow after Stress Maximum in Extension of Branched Polymer Melts**. *Physical Review Letters*, **110**(16):168301, apr 2013.

[3] Marat Andreev, Renat N. Khaliullin, Rudi J. A. Steenbakkers, and Jay D. Schieber. **Approximations of the discrete slip-link model and their effect on nonlinear rheology predictions**. *Journal of Rheology*, **57**(2):535–557, mar 2013.

[4] Carsten Aust, Siegfried Hess, and Martin Krger. **Rotation and Deformation of a Finitely Extendable Flexible Polymer Molecule in a Steady Shear Flow**. *Macromolecules*, **35**(22):8621–8630, sep 2002.

[5] Anders Bach, Kristoffer Almdal, Henrik Koblitz Rasmussen, and Ole Hassager. **Elongational Viscosity of Narrow Molar Mass Distribution Polystyrene**. *Macromolecules*, **36**(14):5174–5179, jun 2003.

[6] C. Baig, B. J. Edwards, D. J. Keffer, and H. D. Cochran. **A proper approach for nonequilibrium molecular dynamics simulations of planar elongational flow**. *The Journal of Chemical Physics*, **122**(11):114103, mar 2005.

[7] C. Baig and V. G. Mavrantzas. **Thermodynamically Guided Nonequilibrium Monte Carlo Method for Generating Realistic Shear Flows in Polymeric Systems**. *Physical Review Letters*, **99**(25):257801, dec 2007.

[8] Chunggi Baig and Vlasis G. Mavrantzas. **Multiscale simulation of polymer melt viscoelasticity: Expanded-ensemble Monte Carlo coupled with atomistic nonequilibrium molecular dynamics**. *Physical Review B*, **79**(14):144302, apr 2009.

[9] Chunggi Baig, Vlasis G. Mavrantzas, and Martin Krger. **Flow Effects on Melt Structure and Entanglement Network of Linear Polymers: Results from a Nonequilibrium Molecular Dynamics Simulation Study of a Polyethylene Melt in Steady Shear**. *Macromolecules*, **43**(16):6886–6902, jul 2010.

[10] Howard A. Barnes, J. F. Hutton, and Kenneth Walters. *An Introduction to Rheology, Volume 3 (Rheology Series)*. Elsevier Science, 1989. Available from: `https://www.amazon.com/Introduction-Rheology-3/dp/0444871403?SubscriptionId=AKIAIOBINVZYXZQZ2U3A&tag=chimbori05-20&linkCode=xm2&camp=2025&creative=165953&creativeASIN=0444871403`.

[11] L. G. Baxandall. **Dynamics of reversibly crosslinked chains**. *Macromolecules*, **22**(4):1982–1988, jul 1989.

[12] Antony N. Beris and Brian J. Edwards. *Thermodynamics of Flowing Systems: with Internal Microstructure*. Oxford University Press, aug 1994.

[13] P. K. Bhattacharjee, D. A. Nguyen, G. H. McKinley, and T. Sridhar. **Extensional stress growth and stress relaxation in entangled polymer solutions**. *Journal of Rheology*, **47**(1):269–290, jan 2003.

[14] P. K. Bhattacharjee, J. P. Oberhauser, G. H. McKinley, L. G. Leal, and T. Sridhar. **Extensional Rheometry of Entangled Solutions**. *Macromolecules*, **35**(27):10131–10148, nov 2002.

[15] Simon Biggs. **Giant Molecules: Here, There, & Everywhere. By Alexander Yu Grosberg**. *Molecules*, **3**(8):142–142, apr 1998.

[16] Hassager Bird, Armstrong. *Dynamics of Polymeric Liquids, Volume 1: Fluid Mechanicshttps://doi.org/10.1016/C2013-0-04284-3*. John Wiley and Sons, May 1987. Available from: `https://www.ebook.de/de/product/3635666/bird_armstrong_hassager_liquids_2e_v1.html`.

[17] R. B. Bird and H. R. Warner. **Hydrodynamic Interaction Effects in Rigid Dumbbell Suspensions. I. Kinetic Theory**. **15**(4):741–750, dec 1971.

[18] M Bom and T Von Karman. **Uber schwingungen in Raumgittern**. *Physik. Z*, **13**:297–309, 1912.

[19] Anton W Bosman, Rint P Sijbesma, and E.W Meijer. **Supramolecular polymers at work**. *Materials Today*, **7**(4):34–39, apr 2004.

[20] X. Callies, C. Fonteneau, C. Véchambre, S. Pensec, J.-M. Chenal, L. Chazeau, L. Bouteiller, G. Ducouret, and C. Creton. **Linear rheology of bis-urea functionalized supramolecular poly(butylacrylate)s: Part I – weak stickers**. *Polymer*, **69**:233–240, jul 2015.

[21] Quan Chen, Hanqing Masser, Huai-Suen Shiau, Siwei Liang, James Runt, Paul C. Painter, and Ralph H. Colby. **Linear Viscoelasticity and Fourier Transform Infrared Spectroscopy of Polyether–Ester–Sulfonate Copolymer Ionomers**. *Macromolecules*, **47**(11):3635–3644, may 2014.

[22] Quan Chen, Gregory J. Tudryn, and Ralph H. Colby. **Ionomer dynamics and the sticky Rouse model**. *Journal of Rheology*, **57**(5):1441–1462, sep 2013.

[23] R. H. Colby, D. C. Boris, W. E. Krause, and S. Dou. **Shear thinning of unentangled flexible polymer liquids**. *Rheologica Acta*, **46**(5):569–575, nov 2006.

[24] Philippe Cordier, François Tournilhac, Corinne Soulié-Ziakovic, and Ludwik Leibler. **Self-healing and thermoreversible rubber from supramolecular assembly**. *Nature*, **451**(7181):977–980, 2008.

[25] Salvatore Costanzo, Qian Huang, Giovanni Ianniruberto, Giuseppe Marrucci, Ole Hassager, and Dimitris Vlassopoulos. **Shear and Extensional Rheology of Polystyrene Melts and Solutions with the Same Number of Entanglements**. *Macromolecules*, **49**(10):3925–3935, may 2016.

[26] W. P. Cox and E. H. Merz. **Correlation of dynamic and steady flow viscosities**. *Journal of Polymer Science*, **28**(118):619–622, apr 1958.

[27] Guanghui Cui, Victor A. H. Boudara, Qian Huang, Guilhem P. Baeza, Andrew J. Wilson, Ole Hassager, Daniel J. Read, and Johan Mattsson. **Linear shear and nonlinear extensional rheology of unentangled supramolecular side-chain polymers**. *Journal of Rheology*, **62**(5):1155–1174, sep 2018.

[28] John G. Curro, Dale S. Pearson, and Eugene Helfand. **Viscoelasticity of randomly crosslinked polymer networks. Relaxation of dangling chains**. *Macromolecules*, **18**(6):1157–1162, jun 1985.

[29] P. G. de Gennes. **Molecular Individualism**. *Science*, **276**(5321):1999–2000, jun 1997.

[30] Tom FA de Greef and EW Meijer. **Supramolecular polymers**. *Nature*, **453**(7192):171–173, 2008.

[31] John M. Dealy, Daniel J. Read, and Ronald G. Larson. *Structure and Rheology of Molten Polymers*. Hanser Fachbuchverlag, 2018. Available from: `https://www.ebook.de/de/product/31595189/john_m_dealy_daniel_j_read_ronald_g_larson_structure_and_rheology_of_molten_polymers.html`.

[32] PATRICK S. DOYLE, ERIC S. G. SHAQFEH, and ALICE P. GAST. **Dynamic simulation of freely draining flexible polymers in steady linear flows**. **334**:251–291, mar 1997.

[33] A. Eisenberg, B. Hird, and R. B. Moore. **A new multiplet-cluster model for the morphology of random ionomers**. *Macromolecules*, **23**(18):4098–4107, sep 1990.

[34] Kathleen E. Feldman, Matthew J. Kade, E. W. Meijer, Craig J. Hawker, and Edward J. Kramer. **Model Transient Networks from Strongly Hydrogen-Bonded Polymers**. *Macromolecules*, **42**(22):9072–9081, sep 2009.

[35] John D. Ferry. *Viscoelastic Properties of Polymers*. Wiley-Blackwell, 1980. Available from: `https://www.ebook.de/de/product/3597161/john_d_ferry_viscoelastic_properties_of_polymers.html`.

[36] Paul. J. Flory and M. Volkenstein. **Statistical mechanics of chain molecules**. **8**(5):699–700, nov 1969.

[37] Paul L. Frattini and Gerald G. Fuller. **Note: A Note on Phase-Modulated Flow Birefringence: A Promising Rheo-Optical Method**. *Journal of Rheology*, **28**(1):61–70, feb 1984.

[38] Yuichi Masubuchi Giovanni Ianniruberto, Giuseppe Marrucci. **Melts of Linear Polymers in Fast Flows**. 2020.

[39] Alexander N. Gorban and Iliya V. Karlin. **Uniqueness of thermodynamic projector and kinetic basis of molecular individualism**. *Physica A: Statistical Mechanics and its Applications*, **336**(3-4):391–432, may 2004.

[40] M. S. Green and A. V. Tobolsky. **A New Approach to the Theory of Relaxing Polymeric Media**. *The Journal of Chemical Physics*, **14**(2):80–92, feb 1946.

[41] Eugene Guth and Herman Mark. **Internal molecular statitics, especially in chain molecules**. *Mh Chem*, **65**:93–121, 1934.

[42] Ole Hassager. **Polymers in Fast Flow: Linking Rheology with Structure**. 2019.

[43] L. G. D. Hawke, M. Ahmadi, H. Goldansaz, and E. van Ruymbeke. **Viscoelastic properties of linear associating poly(n-butyl acrylate) chains**. *Journal of Rheology*, **60**(2):297–310, mar 2016.

[44] Harald Hofmeier and Ulrich S. Schubert. **Recent developments in the supramolecular chemistry of terpyridine–metal complexes**. *Chem. Soc. Rev.*, **33**(6):373–399, 2004.

[45] D. M. Hoyle, Q. Huang, D. Auhl, D. Hassell, H. K. Rasmussen, A. L. Skov, O. G. Harlen, O. Hassager, and T. C. B. McLeish. **Transient overshoot extensional rheology of long-chain branched polyethylenes: Experimental and numerical comparisons between filament stretching and cross-slot flow**. *Journal of Rheology*, **57**(1):293–313, jan 2013.

[46] Chih-Chen Hsieh, Semant Jain, and Ronald G. Larson. **Brownian dynamics simulations with stiff finitely extensible nonlinear elastic-Fraenkel springs as approximations to rods in bead-rod models**. **124**(4):044911, jan 2006.

[47] Q. Huang, J. Ahn, D. Parisi, T. Chang, O. Hassager, S. Panyukov, M. Rubinstein, and D. Vlassopoulos. **Unexpected Stretching of Entangled Ring Macromolecules**. *Physical Review Letters*, **122**(20):208001, may 2019.

[48] Qian Huang, Serena Agostini, Ludovica Hengeller, Maksim Shivokhin, Nicolas J. Alvarez, Lian R. Hutchings, and Ole Hassager. **Dynamics of Star Polymers in Fast Extensional Flow and Stress Relaxation**. *Macromolecules*, **49**(17):6694–6699, aug 2016.

[49] Wook Ryol Hwang, Martien A. Hulsen, and Han E.H. Meijer. **Direct simulation of particle suspensions in sliding bi-periodic frames**. *Journal of Computational Physics*, **194**(2):742–772, mar 2004.

[50] G. Ianniruberto. **Introduction on Polymer Rheology**. In *Reference Module in Chemistry, Molecular Sciences and Chemical Engineering*. Elsevier, 2015.

[51] G Ianniruberto, A Brasiello, and G Marrucci. **Friction coefficient does not stay constant in nonlinear viscoelasticity**. In *Proc. 7th Annu. Eur. Rheol. Conf*, **1**, page 61, 2011.

[52] G. Ianniruberto, A. Brasiello, and G. Marrucci. **Simulations of Fast Shear Flows of PS Oligomers Confirm Monomeric Friction Reduction in Fast Elongational Flows of Monodisperse PS Melts As Indicated by Rheooptical Data**. *Macromolecules*, **45**(19):8058–8066, sep 2012.

[53] Giovanni Ianniruberto. **Extensional Flows of Solutions of Entangled Polymers Confirm Reduction of Friction Coefficient**. *Macromolecules*, **48**(17):6306–6312, aug 2015.

[54] Giovanni Ianniruberto, Antonio Brasiello, and Giuseppe Marrucci. **Modeling Unentangled Polystyrene Melts in Fast Elongational Flows**. *Macromolecules*, **52**(12):4610–4616, jun 2019.

[55] Giovanni Ianniruberto and Giuseppe Marrucci. **Molecular Dynamics Reveals a Dramatic Drop of the Friction Coefficient in Fast Flows of Polymer Melts**. *Macromolecules*, **53**(7):2627–2633, mar 2020.

[56] Giovanni Ianniruberto and Giuseppe Marrucci. **Origin of Shear Thinning in Unentangled Polystyrene Melts**. *Macromolecules*, **53**(4):1338–1345, feb 2020.

[57] Patrick Ilg, Hans Christian ttinger, and Martin Krger. **Systematic time-scale-bridging molecular dynamics applied to flowing polymer melts**. *Physical Review E*, **79**(1):011802, jan 2009.

[58] Tsutomu Indei and Jun ichi Takimoto. **Linear viscoelastic properties of transient networks formed by associating polymers with multiple stickers**. *The Journal of Chemical Physics*, **133**(19):194902, nov 2010.

[59] Jacob N. Israelachvili. *Intermolecular and Surface Forces*. Elsevier, 2011.

[60] Meyer B. Jackson. *Molecular and Cellular Biophysics*. Cambridge University Press, 2006.

[61] Nuofei Jiang, Hongdong Zhang, Ping Tang, and Yuliang Yang. **Linear Viscoelasticity of Associative Polymers: Sticky Rouse Model and the Role of Bridges**. *Macromolecules*, **53**(9):3438–3451, apr 2020.

[62] Nuofei Jiang, Hongdong Zhang, Yuliang Yang, and Ping Tang. **Molecular dynamics simulation of associative polymers: Understanding linear viscoelasticity from the sticky Rouse model**. *Journal of Rheology*, **65**(4):527–547, jul 2021.

[63] Socratis G. Kalogrianitis and Jan W. van Egmond. **Full tensor optical rheometry of polymer fluids**. *Journal of Rheology*, **41**(2):343–364, mar 1997.

[64] J.M. Kim, B.J. Edwards, D.J. Keffer, and B. Khomami. **Single-chain dynamics of linear polyethylene liquids under shear flow**. *Physics Letters A*, **373**(7):769–772, feb 2009.

[65] Kurt Kremer and Gary S. Grest. **Dynamics of entangled linear polymer melts: A molecular-dynamics simulation**. *The Journal of Chemical Physics*, **92**(8):5057–5086, apr 1990.

[66] Martin Krger and Siegfried Hess. **Rheological Evidence for a Dynamical Crossover in Polymer Melts via Nonequilibrium Molecular Dynamics**. *Physical Review Letters*, **85**(5):1128–1131, jul 2000.

[67] W Kuhn. **The shape of fibrous molecules in solution**. *Kolloid-Zeitschrift*, **68**(2), 1934.

[68] W Kuhn and F Grun. **Relationships between elastic constants and stretching double refraction of highly elastic substances**. *Kolloid Z.*, **101**:248, 1942.

[69] R.G. Larson and Priyanka S. Desai. **Modeling the Rheology of Polymer Melts and Solutions**. *Annual Review of Fluid Mechanics*, **47**(1):47–65, jan 2015.

[70] Ronald G. Larson1988a1988ahttps://doi.org/10.1002/bip.1969.360080514. *Constitutive Equations for Polymer Melts and Solutions.* Elsevier, 1988.

[71] MELVIN LAX. **Classical Noise IV: Langevin Methods**. *Reviews of Modern Physics*, **38**(3):541–566, jul 1966.

[72] A W Lees and S F Edwards. **The computer study of transport processes under extreme conditions**. *Journal of Physics C: Solid State Physics*, **5**(15):1921–1928, aug 1972.

[73] Ludwik Leibler, Michael Rubinstein, and Ralph H. Colby. **Dynamics of reversible networks**. *Macromolecules*, **24**(16):4701–4707, aug 1991.

[74] Christopher L. Lewis, Kathleen Stewart, and Mitchell Anthamatten. **The Influence of Hydrogen Bonding Side-Groups on Viscoelastic Behavior of Linear and Network Polymers**. *Macromolecules*, **47**(2):729–740, jan 2014.

[75] J. Li, J. A. Viveros, M. H. Wrue, and M. Anthamatten. **Shape-Memory Effects in Polymer Networks Containing Reversibly Associating Side-Groups**. *Advanced Materials*, **19**(19):2851–2855, oct 2007.

[76] A.E. Likhtman. **Viscoelasticity and Molecular Rheology**. In *Polymer Science: A Comprehensive Reference*, pages 133–179. Elsevier, 2012.

[77] Alexei E. Likhtman, Sathish K. Sukumaran, and Jorge Ramirez. **Linear Viscoelasticity from Molecular Dynamics Simulation of Entangled Polymers**. *Macromolecules*, **40**(18):6748–6757, sep 2007.

[78] David M. Loveless, Sung Lan Jeon, and Stephen L. Craig. **Rational Control of Viscoelastic Properties in Multicomponent Associative Polymer Networks**. *Macromolecules*, **38**(24):10171–10177, oct 2005.

[79] Davide Magatti and Fabio Ferri. **Fast multi-tau real-time software correlator for dynamic light scattering**. *Applied Optics*, **40**(24):4011, aug 2001.

[80] G. Marrucci, S. Bhargava, and S. L. Cooper. **Models of shear-thickening behavior in physically crosslinked networks**. *Macromolecules*, **26**(24):6483–6488, nov 1993.

[81] G. Marrucci and G. Ianniruberto. **Constitutive equations for polymeric solutions close to the overlap concentration**. *Chemical Engineering Science*, **56**(19):5539–5544, oct 2001.

[82] Giuseppe Marrucci and Giovanni Ianniruberto. **Interchain Pressure Effect in Extensional Flows of Entangled Polymer Melts**. *Macromolecules*, **37**(10):3934–3942, apr 2004.

[83] G. Martin, C. Barrès, P. Cassagnau, P. Sonntag, and N. Garois. **Viscoelasticity of randomly crosslinked EPDM networks**. *Polymer*, **49**(7):1892–1901, apr 2008.

[84] S. F. Edwards Masao Doi. *The Theory of Polymer Dynamics*. Oxford University Press, 1988. Available from: `https://www.ebook.de/de/product/3237758/masao_doi_s_f_edwards_the_theory_of_polymer_dynamics.html`.

[85] Yuichi Masubuchi. **Simulating the Flow of Entangled Polymers**. *Annual Review of Chemical and Biomolecular Engineering*, **5**(1):11–33, jun 2014.

[86] Yuichi Masubuchi, Yumi Matsumiya, and Hiroshi Watanabe. **Test of Orientation/Stretch-Induced Reduction of Friction via Primitive Chain Network Simulations for Polystyrene, Polyisoprene, and Poly(n-butyl acrylate)**. *Macromolecules*, **47**(19):6768–6775, sep 2014.

[87] Yuichi Masubuchi, Jun-Ichi Takimoto, Kiyohito Koyama, Giovanni Ianniruberto, Giuseppe Marrucci, and Francesco Greco. **Brownian simulations of a network of reptating primitive chains**. *The Journal of Chemical Physics*, **115**(9):4387–4394, sep 2001.

[88] Yuichi Masubuchi, Takatoshi Yaoita, Yumi Matsumiya, Hiroshi Watanabe, Giovanni Ianniruberto, and Giuseppe Marrucci. **Stretch/orientation Induced Acceleration in Stress Relaxation in Coarse-grained Molecular Dynamics Simulations**. *Nihon Reoroji Gakkaishi*, **41**(1):35–37, 2013.

[89] Yumi Matsumiya and Hiroshi Watanabe. **Non-Universal Features in Uniaxially Extensional Rheology of Linear Polymer Melts and Concentrated Solutions: A Review**. *Progress in Polymer Science*, **112**:101325, jan 2021.

[90] Yumi Matsumiya, Hiroshi Watanabe, Yuichi Masubuchi, Qian Huang, and Ole Hassager. **Nonlinear Elongational Rheology of Unentangled Polystyrene and Poly(p-tert-butylstyrene) Melts**. **51**(23):9710–9729, nov 2018.

[91] L. Robert Middleton and Karen I. Winey. **Nanoscale Aggregation in Acid- and Ion-Containing Polymers**. *Annual Review of Chemical and Biomolecular Engineering*, **8**(1):499–523, jun 2017.

[92] Samantha L. Morelly, Luisa Palmese, Hiroshi Watanabe, and Nicolas J. Alvarez. **Effect of Finite Extensibility on Nonlinear Extensional Rheology of Polymer Melts**. *Macromolecules*, **52**(3):915–922, jan 2019.

[93] Maria Rosella Nobile and Franco Cocchini. **Predictions of linear viscoelastic properties for polydisperse entangled polymers**. *Rheologica Acta*, **39**(2):152–162, mar 2000.

[94] Thomas C. O'Connor, Austin Hopkins, and Mark O. Robbins. **Stress Relaxation in Highly Oriented Melts of Entangled Polymers**. *Macromolecules*, **52**(22):8540–8550, oct 2019.

[95] David J. Olson, Eric F. Brown, and Wesley R. Burghardt. **Second normal stress difference relaxation in a linear polymer melt following step-strain**. *Journal of Polymer Science Part B: Polymer Physics*, **36**(14):2671–2675, oct 1998.

[96] J. T. Padding and W. J. Briels. **Time and length scales of polymer melts studied by coarse-grained molecular dynamics simulations**. *The Journal of Chemical Physics*, **117**(2):925–943, jul 2002.

[97] Johan T Padding. **Advanced courses in Macroscopic Physical Chemistry (Han-sur-Lesse winterschool 2005) THEORY OF POLYMER DYNAMICS**. 2005.

[98] Gun Woo Park and Giovanni Ianniruberto. **Flow-Induced Nematic Interaction and Friction Reduction Successfully Describe PS Melt and Solution Data in Extension Startup and Relaxation**. *Macromolecules*, **50**(12):4787–4796, jun 2017.

[99] Lawrence R. Pratt and Steven W. Haan. **Effects of periodic boundary conditions on equilibrium properties of computer simulated fluids. II. Application to simple liquids**. *The Journal of Chemical Physics*, **74**(3):1873–1876, feb 1981.

[100] Babak Radi, R. Mark Wellard, and Graeme A. George. **Effect of dangling chains on the structure and physical properties of a tightly crosslinked poly(ethylene glycol) network**. *Soft Matter*, **9**(12):3262, 2013.

[101] Jorge Ramírez, Sathish K. Sukumaran, and Alexei E. Likhtman. **Significance of cross correlations in the stress relaxation of polymer melts**. *The Journal of Chemical Physics*, **126**(24):244904, jun 2007.

[102] Jorge Ramírez, Sathish K. Sukumaran, Bart Vorselaars, and Alexei E. Likhtman. **Efficient on the fly calculation of time correlation functions in computer simulations**. *The Journal of Chemical Physics*, **133**(15):154103, oct 2010.

[103] Henrik Koblitz Rasmussen. **A constitutive analysis of the extensional flows of nearly monodisperse polyisoprene melts**. *Polymer*, **104**:251–257, nov 2016.

[104] Henrik Koblitz Rasmussen, Sara Lindeblad Wingstrand, and Ole Hassager. **On the universality in the extensional rheology of monodisperse polymer melts and oligomer dilutions thereof**. *Rheologica Acta*, **58**(6-7):333–340, jun 2019.

[105] Robert C. Armstrong Ole Hassager Robert Byron Bird, Charles F. Curtiss. *Dynamics of Polymeric Liquids, Volume 2: Kinetic Theory, 2nd Edition*. John Wiley and Sons, April 1987. Available from: `https://www.ebook.de/de/product/3597574/bird_armstrong_curtiss_liquids_2e_v2.html`.

[106] Stuart J. Rowan and J. Benjamin Beck. **Metal–ligand induced supramolecular polymerization: A route to responsive materials**. *Faraday Discuss.*, **128**:43–53, 2005.

[107] Michael Rubinstein and Alexander N. Semenov. **Thermoreversible Gelation in Solutions of Associating Polymers. 2. Linear Dynamics**. *Macromolecules*, **31**(4):1386–1397, feb 1998.

[108] Michael Rubinstein and Alexander N. Semenov. **Dynamics of Entangled Solutions of Associating Polymers**. *Macromolecules*, **34**(4):1058–1068, feb 2001.

[109] P. G. Santangelo and C. M. Roland. **Interrupted shear flow of unentangled polystyrene melts**. *Journal of Rheology*, **45**(2):583–594, mar 2001.

[110] Jay D. Schieber, Jesper Neergaard, and Sachin Gupta. **A full-chain, temporary network model with sliplinks, chain-length fluctuations, chain connectivity and chain stretching**. *Journal of Rheology*, **47**(1):213–233, jan 2003.

[111] Th. Schweizer. **Comparing cone-partitioned plate and cone-standard plate shear rheometry of a polystyrene melt**. *Journal of Rheology*, **47**(4):1071–1085, jul 2003.

[112] Thomas Schweizer and Werner Schmidheiny. **A cone-partitioned plate rheometer cell with three partitions (CPP3) to determine shear stress and both normal stress differences for small quantities of polymeric fluids**. *Journal of Rheology*, **57**(3):841–856, may 2013.

[113] Thomas Schweizer, Jan van Meerveld, and Hans Christian ttinger. **Nonlinear shear rheology of polystyrene melt with narrow molecular weight distribution—Experiment and theory**. *Journal of Rheology*, **48**(6):1345–1363, nov 2004.

[114] Sebastian Seiffert and Joris Sprakel. **Physical chemistry of supramolecular polymer networks**. *Chem. Soc. Rev.*, **41**(2):909–930, 2012.

[115] Alexander N. Semenov and Michael Rubinstein. **Thermoreversible Gelation in Solutions of Associative Polymers. 1. Statics**. *Macromolecules*, **31**(4):1373–1385, feb 1998.

[116] Michael J. Serpe and Stephen L. Craig. **Physical Organic Chemistry of Supramolecular Polymers**. *Langmuir*, **23**(4):1626–1634, nov 2006.

[117] Aamir Shabbir, Irakli Javakhishvili, Silvina Cerveny, Søren Hvilsted, Anne L. Skov, Ole Hassager, and Nicolas J. Alvarez. **Linear Viscoelastic and Dielectric Relaxation Response of Unentangled UPy-Based Supramolecular Networks**. *Macromolecules*, **49**(10):3899–3910, may 2016.

[118] Taisir Shahid, Christian Clasen, Filip Oosterlinck, and Evelyne van Ruymbeke. **Diluting Entangled Polymers Affects Transient Hardening but Not Their Steady Elongational Viscosity**. *Macromolecules*, **52**(6):2521–2530, mar 2019.

[119] Rint P. Sijbesma, Felix H. Beijer, Luc Brunsveld, Brigitte J. B. Folmer, J. H. K. Ky Hirschberg, Ronald F. M. Lange, Jimmy K. L. Lowe, and E. W. Meijer. **Reversible Polymers Formed from Self-Complementary Monomers Using Quadruple Hydrogen Bonding**. *Science*, **278**(5343):1601–1604, nov 1997.

[120] F Snijkers, R Pasquino, P D Olmsted, and D Vlassopoulos. **Perspectives on the viscoelasticity and flow behavior of entangled linear and branched polymers**. *Journal of Physics: Condensed Matter*, **27**(47):473002, nov 2015.

[121] T. Sridhar, Mohini Acharya, D. A. Nguyen, and P. K. Bhattacharjee. **On the Extensional Rheology of Polymer Melts and Concentrated Solutions**. *Macromolecules*, **47**(1):379–386, dec 2013.

[122] Robert A. Stratton. **Non-Newtonian Flow in Polymer Systems with No Entanglement Coupling**. *Macromolecules*, **5**(3):304–310, may 1972.

[123] Evgeny B. Stukalin, Li-Heng Cai, N. Arun Kumar, Ludwik Leibler, and Michael Rubinstein. **Self-Healing of Unentangled Polymer Networks with Reversible Bonds**. *Macromolecules*, **46**(18):7525–7541, sep 2013.

[124] A. Subbotin, A. Semenov, E. Manias, G. Hadziioannou, and G. ten Brinke. **Nonlinear Rheology of Polymer Melts under Shear Flow**. *Macromolecules*, **28**(11):3898–3900, may 1995.

[125] Carsten Svaneborg and Ralf Everaers. **Characteristic Time and Length Scales in Melts of Kremer–Grest Bead–Spring Polymers with Wormlike Bending Stiffness**. *Macromolecules*, **53**(6):1917–1941, mar 2020.

[126] Jay A. Syrett, C. Remzi Becer, and David M. Haddleton. **Self-healing and self-mendable polymers**. *Polymer Chemistry*, **1**(7):978, 2010.

[127] L. R. G. Treloar. *The Physics of Rubber Elasticity.* OXFORD UNIV PR, December 2005. Available from: `https://www.ebook.de/de/product/4443563/l_r_g_treloar_the_physics_of_rubber_elasticity.html`.

[128] Evelyne van Ruymbeke, Roland Keunings, and Christian Bailly. **Determination of the molecular weight distribution of entangled linear polymers from linear viscoelasticity data**. *Journal of Non-Newtonian Fluid Mechanics*, **105**(2-3):153–175, aug 2002.

[129] Russell J. Varley and Sybrand van der Zwaag. **Towards an understanding of thermally activated self-healing of an ionomer system during ballistic penetration**. *Acta Materialia*, **56**(19):5737–5750, nov 2008.

[130] Manfred H. Wagner, Saeid Kheirandish, and Ole Hassager. **Quantitative prediction of transient and steady-state elongational viscosity of nearly monodisperse polystyrene melts**. *Journal of Rheology*, **49**(6):1317–1327, nov 2005.

[131] Jennifer H. Ward, Kimberly Furman, and Nicholas A. Peppas. **Effect of monomer type and dangling end size on polymer network synthesis**. *Journal of Applied Polymer Science*, **89**(13):3506–3519, jul 2003.

[132] Harold R. Warner. **Kinetic Theory and Rheology of Dilute Suspensions of Finitely Extendible Dumbbells**. **11**(3):379–387, aug 1972.

[133] H. Watanabe. **Viscoelasticity and dynamics of entangled polymers**. *Progress in Polymer Science*, **24**(9):1253–1403, nov 1999.

[134] Hiroshi Watanabe, Yumi Matsumiya, and Takeshi Sato. **Revisiting Nonlinear Flow Behavior of Rouse Chain: Roles of FENE, Friction-Reduction, and Brownian Force Intensity Variation**. *Macromolecules*, **54**(8):3700–3715, apr 2021.

[135] Lewis E. Wedgewood, Daniel N. Ostrov, and R.Byron Bird. **A finitely extensible bead-spring chain model for dilute polymer solutions**. **40**(1):119–139, jul 1991.

[136] Jean-Luc Wietor, D. J. M. van Beek, Gerrit W. Peters, Eduardo Mendes, and Rint P. Sijbesma. **Effects of Branching and Crystallization on Rheology of Polycaprolactone Supramolecular Polymers with Ureidopyrimidinone End Groups**. *Macromolecules*, **44**(5):1211–1219, feb 2011.

[137] Sara L. Wingstrand, Nicolas J. Alvarez, Qian Huang, and Ole Hassager. **Linear and Nonlinear Universality in the Rheology of Polymer Melts and Solutions**. *Physical Review Letters*, **115**(7):078302, aug 2015.

[138] Xiaolei Xu, Jizhong Chen, and Lijia An. **Shear thinning behavior of linear polymer melts under shear flow via nonequilibrium molecular dynamics**. *The Journal of Chemical Physics*, **140**(17):174902, may 2014.

[139] Takatoshi Yaoita, Takeharu Isaki, Yuichi Masubuchi, Hiroshi Watanabe, Giovanni Ianniruberto, and Giuseppe Marrucci. **Primitive Chain Network Simulation of Elongational Flows of Entangled Linear Chains: Role of Finite Chain Extensibility**. *Macromolecules*, **44**(24):9675–9682, dec 2011.

[140] Takatoshi Yaoita, Takeharu Isaki, Yuichi Masubuchi, Hiroshi Watanabe, Giovanni Ianniruberto, and Giuseppe Marrucci. **Primitive Chain Network Simulation of Elongational Flows of Entangled Linear Chains: Stretch/Orientation-induced Reduction of Monomeric Friction**. *Macromolecules*, **45**(6):2773–2782, mar 2012.

[141] X. Ye, R. G. Larson, C. Pattamaprom, and T. Sridhar. **Extensional properties of monodisperse and bidisperse polystyrene solutions**. *Journal of Rheology*, **47**(2):443–468, mar 2003.

[142] Wayne C. Yount, David M. Loveless, and Stephen L. Craig. **Small-Molecule Dynamics and Mechanisms Underlying the Macroscopic Mechanical Properties of Coordinatively Cross-Linked Polymer Networks**. *Journal of the American Chemical Society*, **127**(41):14488–14496, sep 2005.

[143] Wayne C. Yount, David M. Loveless, and Stephen L. Craig. **Strong Means Slow: Dynamic Contributions to the Bulk Mechanical Properties of Supramolecular Networks**. *Angewandte Chemie International Edition*, **44**(18):2746–2748, apr 2005.

[144] Longhe Zhang, Nicole R. Brostowitz, Kevin A. Cavicchi, and R. A. Weiss. **Perspective: Ionomer Research and Applications**. *Macromolecular Reaction Engineering*, **8**(2):81–99, dec 2013.